First-Principles Calculations on the Electronic and Optical Properties of Polar Functional Materials

by

Nocona Sanders

A dissertation submitted in partial fulfillment
of the requirements for the degree of
Doctor of Philosophy
(Materials Science and Engineering)
in the University of Michigan
2021

Doctoral Committee:

Associate Professor Emmanouil Kioupakis, Chair
Assistant Professor Elaheh Ahmadi
Professor Zetian Mi
Assistant Professor Liang Qi

Nocona Sanders
nocona@umich.edu
ORCID iD: 0000-0003-2471-2128

© Nocona Sanders 2021
All Rights Reserved

ACKNOWLEDGEMENTS

Personal acknowledgements

Manos: Joining your group was by far the best decision I've ever made. You are a phenomenal advisor in every sense of the word. I have been especially thankful for your patience, even in some of the hardest times of my professional and personal life. There were plenty of times when I didn't think I was deserving or capable of earning this degree, so I can never thank you enough for your support along every step of the way. Working with you the past five years has been an absolute joy, and I could not be any happier at how my graduate experience turned out.

Kioupakis Group: You are a second family to me. I am incredibly happy to have spent the past five years surrounded by brilliant minds and supportive friends. Going into the office was always a joy (except for when the bees attacked us!), and I have learned a lot from everyone. My graduate experience was a positive one largely because of the culture we have in our group, so I am extremely grateful for all of you.

Dylan and Christina: A special thanks in the group goes out to you. I would not have survived my first year without your patience in showing me the ropes. You both helped me get through imposter syndrome and proved to me I had all the tools I needed to succeed. You guys rock.

Kelsey M: You are without a doubt my twin in every possible way. You convinced me to join the Kioupakis group, helped me move into my first apartment in Michigan, and have been there for me ever since. I truly cannot express how lucky I am that I can count on you for anything and everything. So many of my good times in Michigan were because of you, and hands down our float trip days are some of the best memories. I know we will be friends for life, and 2008 will be here before you know it.

Juan: It is hard to believe we have known each other for nine whole years, but it has been such an unbelievable journey. From long nights studying at S&T to driving on a cross-country road trip to navigating grad school and life at large, I am very

thankful you have been there with me every step of the way. You are a true friend, and I am deeply touched by your constant support. Just remember that you will always be the responsible adult.

Mark: You have helped me grow in ways I never thought possible. I am constantly impressed with your determination and drive, and it has definitely helped me sustain those qualities in myself. We have been through a lot together, and I am even more excited about what the future will bring. I am forever appreciative of everything you do.

Kelsey C: A friendship forged over taco soup wars. Thank you for helping me navigate my first half of grad school. I whined to you way more than you probably wanted, but I am thankful you helped me find my way. Looking forward to being your neighbor in California!

Vazrik and Kam: You guys have been through this journey with me from day one. From working together through 550 to navigating candidacy and beyond, I am thankful I have been able to count on your encouragement.

Dr. Medvedeva: Your work is what inspired me to go into this line of research. You were my first role model for what a professional scientist looks like, and you spent many, many hours helping me learn what it means to be a researcher. Thanks for taking a chance on me in my very first semester at S&T. I am endlessly grateful.

STPP: I owe my career aspirations to the Science, Technology, and Public Policy program. Before STPP I only had a vague idea of what I wanted to do with my degree, but they opened the door to so many possibilities. They broke my notions of what science is, but gave me a completely new perspective on what it can be. Dr. Rohde, thank you for giving me the tools to survive in the science policy world and for helping me plan my consensus conference. Dr. Mills, thank you for helping me learn the energy policy landscape and giving me lots of career advice.

Family: I could not have done this without your support. All of you have been monumental in giving me the courage to pursue a path this rigorous and shaping me as a person. I hope to make you proud in all that I do.

Funding acknowledgements

The projects in this work were supported through a variety of sources. I gratefully acknowledge the NSF ECCS-CDS&E program (1607796), the computational resources provided by the DOE NERSC facility under Contract No. DE-AC02-05CH11231, the Materials Science and Engineering Program, the University of Michi-

gan's Rackham Merit Fellowship, and Rackham Conference Travel Grants.

Copyright acknowledgements

Chapter 3 is reprinted (adapted) with permission from Nano Letters. Copyright (2017) American Chemical Society.

Chapter 4 is reprinted (adapted) with permission from The Journal of Physical Chemistry C. Copyright (2021) American Chemical Society.

Chapter 7 is reprinted (adapted) with permission from Applied Physics Letters. Copyright (2021) American Physical Society.

TABLE OF CONTENTS

ACKNOWLEDGEMENTS ii

LIST OF FIGURES viii

LIST OF TABLES xii

ABSTRACT xiii

CHAPTER

I. Introduction 1

1.1 Solid state lighting and the Group-III nitrides 2
1.2 Two-dimensional materials 3
1.3 High-power electronics 4
1.4 Organization of thesis 6

II. Computational Methods 8

2.1 Density Functional Theory 8
2.1.1 Theoretical foundations 9
2.2 Density Functional Perturbation Theory (DFPT) 9
2.3 Many-body perturbation theory 10
2.3.1 The GW method 10
2.3.2 Bethe-Salpeter equation (BSE) 11
2.4 Maximally-localized Wannier functions 11
2.5 Iterative Boltzmann Transport Equation and Electron-Phonon-Wannier (EPW) 12

III. Electronic and Optical Properties of Two-Dimensional GaN from First-Principles 15

3.1 Background and motivation 15
3.2 Project objectives 16

3.3 Methods . . . 16
3.4 Energetics of formation and hydrogen-passivation . . . 19
3.5 Electronic properties . . . 19
3.6 Optical and excitonic properties . . . 21
3.7 Strain effects . . . 23
3.8 Conclusions . . . 26

IV. Effect of Stacking Orientation on the Electronic and Optical Properties of Polar 2D III-nitride Bilayers . . . 27

4.1 Background and motivation . . . 27
4.2 Project objectives and overview . . . 29
4.3 Methods . . . 29
4.4 Thermodynamics and surface passivation . . . 30
4.5 Electronic properties . . . 33
4.6 Optical and excitonic properties . . . 38
4.7 Conclusions . . . 39

V. Carrier Mobility of Copper (I) Oxide . . . 41

5.1 Background and motivation . . . 41
5.2 Project objectives and overview . . . 41
5.3 Methods . . . 42
5.4 Carrier mobility and scattering . . . 43
5.5 Conclusions . . . 45

VI. Carrier Mobility of Ultra-Wide-Band-Gap (UWBG) Semiconductors . . . 46

6.1 Background and motivation . . . 46
6.2 Project objectives and overview . . . 47
6.3 Methods . . . 48
6.4 Phonons and band structures . . . 48
6.5 Carrier mobility . . . 50
6.6 Conclusions . . . 51

VII. Phonon- and Defect-limited Electron and Hole Mobility of Diamond and Cubic Boron Nitride: A Critical Comparison . . . 52

7.1 Background and motivation . . . 52
7.2 Project objectives and overview . . . 53
7.3 Methods . . . 55
7.4 Band structures and effective masses . . . 56
7.5 Phonon dispersions . . . 57
7.6 Scattering mechanisms and carrier mobility . . . 59

7.7 Impurity scattering 65
7.8 Conclusions 66

VIII. Summary and Future Work 68

8.1 Summary 68
8.2 Future work 70

APPENDICES 72
A.1 Mechanical stability 73
A.2 Details of band gap and exciton binding energy calculations . 75
A.3 GW corrections to LDA band structures 75
A.4 Wave functions as a function of strain 76
A.5 Electric field determination from polarization 77
A.6 Optical absorption spectra 79

BIBLIOGRAPHY 80

LIST OF FIGURES

FIGURE

3.1 Electron and hole wave functions squared for (a) monolayer and (b) bilayer 2D GaN, and plane-averaged electrostatic potentials for (c)monolayer and (d) bilayer 2D GaN. The polarization fields within each structure spatially separate electrons and holes. The artificial dipole correction in the vacuum region is necessary to cancel out artifacts of the periodic boundary conditions. The distance and slope between peaks of like atoms, indicated by the dashed line in (c), allow for the calculation of the internal electric field magnitude. 18

3.2 Quasiparticle band structures of (a) monolayer and (b) bilayer 2D GaN. Both materials exhibit a direct gap at Γ. The polarization fields counteract the effects of confinement in the bilayer structure. . 20

3.3 Optical gap of monolayer and bilayer 2D GaN as a function of biaxial strain. Compressive strain is a viable method for controlling the band gap of both structures. These results were determined from the DFT gap as a function of strain adjusted to account for the GW and BSE corrections at zero strain. 25

3.4 Energy splitting between the heavy and light holes of monolayer and bilayer GaN as a function of uniaxial strain. Uniaxial strain lifts the band degeneracy, resulting in polarized light emission along the axis of compressive strain. 25

4.1 Preferred passivation state of (a) BN, (b) AlN, (c) GaN, and (d) InN monolayer as a function of hydrogen partial pressure (Pa) and temperature (K). Under standard room-temperature conditions, BN adopts a planar hexagonal, unpassivated structure, and AlN, GaN, and InN adopt buckled tetrahedral, passivated structures. 32

4.2 The three possible orientations of III-nitride heterostructures, where the polarization is treated as the degree of freedom. The blue arrows denote the polarization direction of each monolayer. 34

4.3 Quasiparticle band structures of the freestanding monolayer and of the bilayer stacks [aligned, antialigned with interposed cations ("cation sandwich"), and antialigned with interposed N ("N sandwich")] of BN, AlN, GaN, and InN. Red arrows denote the fundamental band gap. The high-symmetry points are Γ (0,0,0), K (1/3, 1/3, 0), and M (0.5,0,0). The band gaps of 2D III-nitride monolayers and their bilayer structures span the visible and UV ranges. 35
4.4 Electron and hole wave functions squared for (a) aligned, (b) antialigned with interposed N, and (c) antialigned with interposed Ga bilayers of GaN. Although the holes remain localized on the N atoms, electrons reside outside the GaN planes due to the strong out-of-plane electric dipole moment and their location can be controlled by the stacking orientation. 37
5.1 Phonon-limited hole drift mobility in Cu_2O as a function of temperature. 43
5.2 Phonon-mode-resolved imaginary self-energies as a function of the hole energy in Cu_2O. 0 eV is referenced to the valence band edge. . 44
5.3 Visualization of the atomic displacements of phonon modes (a) 11 and (b) 18 of Cu_2O. The larger atoms are copper, shown in brown, and the smaller atoms are oxygen, shown in red. These polar optical modes dominate the scattering at room temperature. 45
6.1 Phonon dispersions of (a) rs-BeO, (b) zb-BeO, (c) wz-BeO, and (d) MgO. All structures have positive phonon frequencies after relaxation. 49
6.2 Quasiparticle band structures of (a) rs-BeO, (b) zb-BeO, (c) wz-BeO, and (d) MgO. All four have large band gaps and small electron effective masses. 50
6.3 Carrier drift mobilities of MgO, rs-BeO, zb-BeO, and wz-BeO. . . . 51
7.1 The band structure and atom-projected density of states of (a) cBN and (b) diamond, shown with their crystal structures. While the band gaps are similar, the hole effective masses are heavier in cBN. This is because the cBN valence bands consist primarily of second-nearest-neighbor N orbitals, while the diamond valence band is formed by nearest-neighbor C orbitals. 57
7.2 Phonon dispersions of (a) cBN and (b) diamond. With the exception of the LO-TO splitting at Γ in polar c-BN, both structures exhibit similar maximum phonon frequencies, sound velocities, and overall band characteristics. 59
7.3 Squared electron-phonon coupling intraband matrix elements for the conduction band of (a)-(b) cBN and (c)-(d) diamond as a function of the phonon wave vector along two perpendicular crystallographic directions. The 1/4 fractions denote a quarter of the distance along the reciprocal-space path to the designated high-symmetry point. The modes that couple most strongly to electrons are the polar optical (LO) modes in c-BN and the LA modes in diamond. 61

7.4 Squared electron-phonon coupling matrix elements for the topmost valence band of (a)-(c) cBN and (d)-(f) diamond. The 1/4 fractions denote a quarter of the distance along the reciprocal-space path to the designated high-symmetry point. The modes that couple most strongly to holes for small wave vectors q are the polar optical (LO) modes in c-BN and the TO modes in diamond. 62
7.5 Phonon-mode-resolved imaginary self-energies (i.e., carrier scattering rates) as a function of the carrier energy for (a) electrons in cBN, (b) electrons in diamond, (c) holes in cBN, and (d) holes in diamond. The scattering rates of thermal electrons (i.e., within a few k_B T from the band extremum) are comparable for the two materials, but thermal holes scatter at an 1-2 orders-of-magnitude faster rate in cBN compared to diamond. 63
7.6 Phonon-limited carrier drift mobilities in cBN and diamond as a function of temperature. The experimental diamond drift mobilities are from natural diamond samples (Nava *et al.*,[1] and Reggiani *et al.*[2]) Experimental cBN Hall mobilities are from single crystal (Wang *et al.*[3] and Taniguchi *et al.*[4]) and thin films. (Livinov *et al.*,[5] Liao *et al.*,[6] He *et al.*,[7] and Kojima *et al.*[8]) Open symbols denote thin-film samples. Although the electron mobility is similar in the two materials, the hole mobility in c-BN is much lower than in diamond. The heavier hole effective mass in c-BN and the resulting larger density of states increase the hole-scattering rates and reduce the hole mobility compared to diamond. 64
7.7 Carrier mobility at 300K as a function of donor/acceptor density density in (a) n-type, Si-doped cBN, (b) n-type, P-doped diamond, (c) p-type, Be-doped cBN, and (d) p-type, B-doped diamond. Dashed and dotted lines show the theoretical contributions from lattice scattering, neutral impurities, and ionized impurities. Experimental data points are from experimental work by Wang et al.,[3] He et al.,[7] Taniguchi et al.,[4] Pernot et al.,[9] Gabrysch et al.,[10] Werner et al.,[11] Mortet et al.,[12] Thonke,[13] Tsukioka and Okushi,[14] and Volpe et al.[15] 67
A.1 Phonon dispersion plots of (a) monolayer and (b) bilayer GaN. The low frequency modes for the monolayer (c) and bilayer (d) are also more clearly shown. Positive frequencies confirm the mechanical stability of the structures. Small negative phonon frequencies for the flexural mode near Γ are likely due to finite numerical and convergence accuracy. 74
A.2 Band gaps (a) and exciton binding energies (b) of 2D GaN as a function of Brillouin-zone sampling points (NKxNKx1). The data are extrapolated to an infinite number of grid points with trend lines given in Equations A.1 and A.2 fitted to the calculated data. 76
A.3 Quasiparticle corrections to the LDA eigenenergies as a function of the LDA energy for (a) monolayer and (b) bilayer GaN. Solid lines represent the constructed scissors operators. 76

A.4 Band structure of (a) monolayer and (b) bilayer GaN calculated with LDA and LDA+G_0W_0. Energies are referenced to the valence band maximum. GW corrections were added via scissors shift operators. Both materials show a direct band gap at Γ. 77
A.5 Electron and hole wave functions squared for (a-c) monolayer and (d-f) bilayer 2D GaN. The application of compressive biaxial strain further increases the electron-hole separation, which amplifies the Stark effect and band-gap reduction. 78
A.6 Optical absorbance spectra for (a) monolayer and (b) bilayer GaN with a 5% uniaxial tensile strain applied along the y-axis. Uniaxial tensile strain along the y-axis breaks the in-plane symmetry of the crystal, resulting in anisotropic light absorption and hence polarized light emission along the x-axis. 79

LIST OF TABLES

TABLE

3.1 Band Gaps, Binding Energies, and Optical Gaps of 2D GaN 20

3.2 Hole Effective Masses of Monolayer GaN 24

4.1 Structural properties of III-nitride monolayers and heterostructures. 36

4.2 Exciton binding energies, luminescence energy, and exciton radiative lifetimes of GaN bilayers. The exciton binding energies remain strong (~ 1 eV) and the lifetimes short (a few ns) regardless of the stacking arrangement. 39

7.1 A summary of experimental room-temperature carrier mobility values in cBN and diamond. 54

7.2 Carrier effective masses of cBN and diamond after GW corrections. Although the electron masses are similar, holes are heavier in cBN. 58

7.3 Our calculated values for the optical phonon frequencies at Γ and the acoustic sound velocities in cBN and diamond compared to experimental measurements. Asterisks denote polycrystalline samples. . . 60

ABSTRACT

Advanced computational methods are continually pushing the boundary of modern materials science. They can guide experimental inquiry by surveying a large number of materials for functional properties as well as guide the design and synthesis of new materials with targeted properties, at a much faster speed than experimental approaches. This rise in predictive insight has helped foster the semiconductor revolution, and in turn, created technologies which make a direct impact on global challenges such as the energy crisis and global warming. However, even with this success, there are a wide variety of materials left to be examined in detail.

In this work two-dimensional (2D), hydrogen-passivated III-nitrides are examined. Density functional theory and many-body perturbation theory are applied to produce accurate band structures and use the Bethe-Salpeter Equation to predict exciton binding energies. The strong polarization in III-nitride monolayers results in a significant quantum-confined Stark effect (QCSE), reducing the large band gaps caused by quantum confinement. Using the polarization as a degree of freedom in constructing bilayer heterostructures, it is shown that aligned orientations yield relatively small band gaps (1.9 eV – 3.2 eV), whereas in anti-aligned orientations there is no QCSE and the gap remains large (>4.4 eV). Exciton binding energies are on the order of 1 eV. These results show that UV emission from 2D GaN is possible and that the optical gaps of 2D III-nitrides span the visible and UV spectra.

The second portion of this work is dedicated to examining the carrier mobilities of

various semiconductors using density functional theory, many-body perturbation theory, and the electron-phonon Wannier method. The phonon-limited hole mobility of Cu_2O is determined and it is shown that at room temperature it is polar optical modes which are predominantly responsible for carrier scattering. Four ultra-wide-band-gap (UWBG) materials, rs-BeO, wz-BeO, zb-BeO, and MgO, are then examined. Their ultra-wide band gaps (>6 eV) highlight their promise in high-power electronics, and their electron carrier mobilities are high as well ($>107\ cm^2/Vs$ at room temperature). Finally, the carrier mobility of cubic BN and diamond are examined since experimental results on cBN hole mobility span two orders of magnitude. Electron-phonon coupling matrix elements are evaluated to show that acoustic mode coupling is lower in diamond than in cBN. It is also shown that the room temperature scattering rate of holes is much faster in cBN than diamond. Overall, electron mobilities are comparable while cBN hole mobility (80.4 $\mathrm{cm^2/Vs}$) is lower than that of diamond (1970 $\mathrm{cm^2/Vs}$).

These computational results emphasize the applicability of 2D and UWBG materials to optoelectronic devices and suggest that polar materials provide a wide degree of useful functional properties.

CHAPTER I

Introduction

In 2015, the United Nations laid out a blueprint for its vision of the next 15 years. In it, it gives its hopes for what countries of the world will enact to do to tackle the grand challenges of our time, from global warming to the energy crisis and social injustice. While it is important to recognize the gravity of these problems, it is also necessary to underscore the role that individual materials can play in bringing about change.

While we no longer characterize time periods by the latest material breakthrough such as in the Bronze Age, materials are still just as crucial in enabling larger-scale solutions. Goal six of the UN's Sustainable Development Goals is ensuring all people have access to clean water, and ultraviolet light-emitting diodes (LEDs) are a strong contender for enabling portable sanitation. Energy-efficient materials are a key driver in promoting goals six and thirteen, which are to grow affordable and clean energy and to take action on climate change, respectively. Even on the goals that seem mostly social at face value, such as creating sustainable cities and communities and encouraging responsible consumption and production, materials can make a big difference. Creating functional materials that are nontoxic, affordable, and derived from earth-abundant elements go a long way in creating equitable access to next-generation technologies.

Part of the success of modern science is in its collaborative nature. Now more than ever, scientists at every point of the innovation chain can share ideas and work together. Fundamental materials science is able to break out of the mold of being considered a pure science removed from solution-driven goals, and it is constantly changing the frontier of what is possible in the engineering landscape. While the materials discussed in this work are only a minuscule fraction of the functional materials leading the change to address global challenges, they still add to the patchwork of solutions.

1.1 Solid state lighting and the Group-III nitrides

For most of the time that people have used artificial lighting, we have relied on fire. With the electrification of homes however, incandescent bulbs quickly became popular. These bulbs function by passing current through a filament, heating it to the point that it emits a glow. However, these bulbs are quite inefficient (<10%), as most of the energy input is used to generate heat rather than light.[16] Even more troublesome is the fact that most commercial incandescent bulbs only have an operating lifespan of 1,000 hours, effectively corresponding to a year of functional life under typical usage patterns before needing to be replaced. Given that approximately one fifth of U.S. energy is used to power lights,[17] reductions in energy use in lighting applications have the potential to make a large impact in overall domestic energy demand.

Lighting made another significant advance in the 1990s as compact fluorescent bulbs started becoming more widespread. Their efficiencies are larger than incandescent bulbs, but they are troublesome in other aspects. The main consideration is that the bulbs contain mercury gas, which is toxic and harmful to the environment. Improper disposal of these bulbs results in the gas escaping and posing a public health risk.

Newer generation light bulbs are based on light-emitting diodes (LEDs), which avoid both the downfalls of inefficiency and toxicity. These devices function by utilizing doped semiconductors. Doping refers to the process of adding impurities into a material to change the number of free carriers. N-type semiconductors have an excess of electrons, and p-type semiconductors have a shortage of electrons. By combining two of these materials together to create a p-n junction, electrons are able to recombine with holes to emit photons. The wavelength of the emitted light depends on the particular materials used to make the junction, but this operational principle holds for all types of LEDs.

A popular configuration for generating white light utilizes ultraviolet (UV) light emission. The LED produces UV light, and a phosphor coating on the surface of the bulb down-converts that light into visible colors at a ratio that we perceive as white light. GaN and AlGaN alloys are key materials in driving this technology. High-quality GaN was first synthesized in 1986,[18] and the 2014 Nobel Prize in Physics was awarded to a team of researchers who had pioneered its successful doping.[19,20] Yet despite all its success, there is still room for improvement. The low light-extraction efficiency and lack of deep-UV-transparent p-type contacts limit the overall efficiency of deep-UV AlGaN LEDs.[21] One avenue being investigated for improving the efficiency is to use the two-dimensional (2D) materials.

1.2 Two-dimensional materials

The 2D materials revolution began in 2004, when graphene was isolated for the first time.[22] Its exotic properties include a band gap of zero, large thermal and electrical conductivity, and a strength over five times that of steel.[23] Beyond graphene, many materials, notably transition metal dichalcogenides, have been produced in a monolayer or few-layer form. Interestingly, a popular method for obtaining samples of 2D materials is to use mechanical exfoliation, which is to simply press adhesive

tape against the surface of a bulk crystal and then gently remove. However, more precise methods such as chemical vapor deposition and molecular beam epitaxy are used to produce higher quality samples. The reduced dimensionality of these 2D materials allows for quantum confinement effects which significantly increase the band gap. Additionally, the lowered electronic screening allows for enhanced excitonic effects relative to the bulk material and a significant Quantum-confined Stark Effect (QCSE). In terms of mechanical stability, because the vertical growth direction is small, these materials are often able to withstand larger degrees of stress without compromising material quality, allowing for a wider variety of substrates to be used with them.

Overall, these characteristics and more make 2D materials, especially the TMDCs, promising candidates for miniaturized circuits,[24] photocatalysis for energy conversion,[25,26] large-scale flexible and transparent electronics,[27] and more. Significant research attention is being directed at identifying which bulk materials are chemically and mechanically stable in 2D form, how to synthesize them, and what their functional properties are. While devices based on 2D architectures are still in their infancy, it is expected that quantum-dot qubits, single-photon emitters, superconducting qubits and topological quantum computing elements will usher in the era of quantum information science.[28] Part of this work is dedicated to calculating the properties of 2D III-nitrides, which revolutionized the electronics industry as bulk materials and may do so again with their 2D counterparts.

1.3 High-power electronics

Part of modernizing infrastructure and creating a better platform to electrify technologies currently based largely on fossil fuels is facilitating the deployment of high-power electronics. In power lines, high voltages minimize the amount of energy lost as waste heat, improving overall efficiency. Additionally, some energy production

facilities generate large amounts of energy, meaning that they require devices able to withstand these demands. Materials can be classified by their Baliga figure of merit (BFOM), a metric quantifying a material's suitability for high-power, low-frequency applications[29,30]:

$$BFOM = \frac{1}{4}\epsilon_0 \mu E_G^3 \tag{1.1}$$

where ϵ_0 is the static dielectric constant, μ is the carrier mobility, and E_G is the band gap. The largest contributor to this figure is the band gap, making ultra-wide-band-gap (UWBG) materials highly desirable for these applications.

They are able to withstand larger voltages before reaching the critical breakdown where the material is irreparably damaged. Materials with band gaps larger than 6 eV are gaining significant attention because of their large breakdown field values. It was previously believed that large band gap materials had inferior functional properties due to challenges associated with doping. However, with some UWBG materials now showing sufficient dopability, larger BFOMs are being seen now than ever before, highlighting the power of these materials in enabling next-generation electronics.

Another key contributor to the BFOM is the mobility. While the BFOM scales with the cube of the band gap and mobility is only a linear scaling, mobility is not an insignificant contributor. Many challenges are present in optimizing carrier mobility in a material. Temperature is a key consideration, as mobility falls rapidly with increasing temperature. Finding materials with sizeable room temperature mobility is crucial to enabling devices which can operate in standard conditions, outside of a lab or specialized facility. Another factor in the mobility is material quality. Grain boundaries and impurities hinder the mobility, making high-quality synthesis a significant driver of this field as a whole.

However, computation can still play a major role in this arena. First-principles approaches allow for the consideration of metastable and unstable phases, which are

important for understanding the relationships between structure and property, even if some of the structures require conditions such as high pressures to be mechanically stable. Computation can also examine materials in their pristine state, without any interference from substrate screening or strain, and at a faster pace. While experiment is always necessary to confirm properties and examine materials under real-world conditions, computation still gives critical insight into the theoretical upper limit for materials, guiding experimental inquiry and saving time.

1.4 Organization of thesis

This dissertation contains computational studies of electronic and optical properties of several III-nitride materials, their two-dimensional counterparts, several ultrawide-band-gap (UWBG) semiconductors, and copper (I) oxide. This work is organized into the following seven chapters.

In Chapter II, we provide details on the computational methods employed throughout this work. Attention is given to methods involving density functional theory, quasiparticle corrections, and EPW codes.

Chapter III focuses on the electronic and optical properties of two-dimensional GaN. We predict electronic band gaps, luminescence energies, and excitonic properties of monolayer and bilayer 2D GaN as a function of strain, with an overall goal of elucidating how reduction to the 2D regime affects the overall properties as compared to the bulk material.

In Chapter IV, we discuss the electronic properties of hydrogen-passivated, monolayer BN, AlN, GaN, and InN, as well as their bilayer structures. We treat the polarization of each layer as an additional degree of freedom in tuning the electronic properties.

Chapter V is a study on the carrier mobility of copper (I) oxide to access its potential to be incorporated into a high performance p-type thin film transistor.

In Chapter VI, we present the quasiparticle band structures and electron mobilities of several UWBG semiconductors.

Chapter VII details work on the carrier mobilities of cubic BN and diamond. We perform GW corrections and discuss carrier mobility for both p-type and n-type materials.

Finally, Chapter VIII gives a summary of this work, puts it in perspective with current research, and provides directions for future work.

CHAPTER II

Computational Methods

2.1 Density Functional Theory

Conceptualized in the 1960s, density functional theory has completely revolutionized the fields of physics and materials science. As of a 2010 analysis, all of the top three most-cited physics papers (and eight of the top ten) were in the field of DFT.[31] Utilizing a relatively simple conceptual framework, the method has shown remarkable success at calculating a wide variety of material properties, including bond lengths, lattice constants, energies of formation, and effective masses, making it colloquially become known as the workhorse of quantum materials science. This predictive insight has allowed researchers to guide experimental inquiries into existing materials as well as probe materials which have never been synthesized. Within the scope of this work, DFT serves as the starting point for all calculations.

Highlighting the robust capabilities of this approach, DFT-based methods have been used to investigate the thermal conductivity and carrier mobility of GeO_2,[32–34] carrier mobility of $Al_xGa_{1-x}N$,[35] strain effects on band alignments and carrier mobility of BAs,[36] and of course the electronic structure of 2D III-nitride heterostructures,[37] and carrier mobilities of cBN and diamond,[38] the latter two of which are presented later in this work.

2.1.1 Theoretical foundations

DFT is a method for determining the ground-state of a system. Ideally, this information would be obtained by solving Schrödinger's equation to obtain the wave function, but in a system of N electrons, the expression becomes

$$[\sum_{i}^{N}(-\frac{\hbar^2\nabla_i^2}{2m}) + v(\mathbf{r}_i) + \sum_{i<j} U(\mathbf{r}_i, \mathbf{r}_j)]\Psi(\mathbf{r}_1, \mathbf{r}_2, ..., \mathbf{r}_N) = E\Psi(\mathbf{r}_1, \mathbf{r}_2, ..., \mathbf{r}_N) \tag{2.1}$$

where $U(\mathbf{r}_i, \mathbf{r}_j)$ is the electron-electron potential. Once more than two electrons are under consideration, the expression becomes difficult to solve even with numerical approaches.

In 1964, Hohenberg and Kohn simplified the approach by establishing the formalism that the ground state of a quantum mechanical system is determined by the system's electron density.[39] This is achieved by using $n(\mathbf{r})$ - the electron density - as a variable. Thus, the task of calculating electronic properties was retooled into finding the electron density that minimizes the total energy of the system.

This method was further refined in 1965 when Kohn and Sham proved that it is equivalent to describe a quantum system as one of non-interacting electrons moving in a fictitious external potential.[40] This approach reduces Schrödinger's equation to one dimension and allows electrons to be considered individually. Combining the two methodologies forms the basis of DFT and provides a robust tool for investigating ground state properties.

2.2 Density Functional Perturbation Theory (DFPT)

Once the electronic ground state and atomic positions are known, interatomic force constants can be calculated by the linear response method, also known as density functional perturbation theory. Through the variational principle of DFT, the second

order change in energy depends on the first order change in the electron density. Combined with the linear response to a distortion of atomic positions, the second order perturbation in the total energy can be self-consistently minimized.[41] The strength of this method is that it allows for the calculation of phonon frequencies at arbitrary wave vectors **q** without requiring the use of a supercell to explicitly calculate long-range forces resulting from a specific atomic displacement.

2.3 Many-body perturbation theory

Despite the success of DFT at calculating a wide range of ground state properties, it faces significant shortcomings in calculating excited state phenomena. Specifically, the band gap of many materials are predicted to be on the order of 30%-50% smaller than values confirmed by experiment. This arises because, with local and semilocal approximations to the exchange-correlation potential, unphysical self-interaction of the electron with itself arises due to the included Hartree energy. Because the exchange-correlation cannot precisely negate this effect, the energy of occupied states is unphysically lowered. Thus, it is common for DFT to be followed by another method such as many-body perturbation theory.[42]

2.3.1 The GW method

The GW method is one such process. It provides an approximation to the electron self-energy given DFT-level wave functions and eigenvalues. The name arises because the self-energy operator Σ, an infinite power sum, is truncated to:

$$\Sigma = iGW \tag{2.2}$$

where G is Green's function and W is the screened Coulomb interaction.[43] The correct quasiparticle wave functions and energies are then calculated via the Dyson

equation:[44,45]

$$[-\frac{1}{2}\nabla^2 + V_{ion} + V_H + \Sigma(E^{QP}_{n\mathbf{k}})]\Psi^{QP}_{n\mathbf{k}} = E^{QP}_{n\mathbf{k}}\Psi^{QP}_{n\mathbf{k}} \tag{2.3}$$

where V_{ion} is the ionic potential, V_H is the Hartree potential, $E^{QP}_{n\mathbf{k}}$ is the quasiparticle energy, and $\Psi^{QP}_{n\mathbf{k}}$ is the quasiparticle wave function. This approach has shown tremendous success in calculating the correct band gap of a wide variety of semiconducting and insulating materials, making it a powerful tool within the field of computational physics.

2.3.2 Bethe-Salpeter equation (BSE)

The Bethe-Salpeter equation is another many-body method commonly used to calculate exciton binding energy. Specifically, electron-hole pairs are bound states Ψ_{ij} constructed from individual electron and hole states ψ_i and ψ_j, respectively, interacting through the system's Coulomb interaction:[46]

$$(E_i - E_j)\psi_{ij} + \sum_{l,m}\langle ij|K|lm\rangle = \Omega\psi_{ij} \tag{2.4}$$

where K is the Coulomb interaction kernel. Knowing exciton properties thus enables the determination of optical properties dependent on the phenomenon.[47] Subtracting the exciton binding energy from the GW-corrected band gap energy yields the accurate luminescence energy, a quantity especially useful in the field of solid state lighting.

2.4 Maximally-localized Wannier functions

While the optimal method for calculating band structures on dense grids is to sample every point in the Brillouin zone, in principle this approach is not feasible due to computational limitations. Even by only calculating points within symmetry-

reduced irreducible Brillouin zone wedges, the number of points can easily render a simple calculation impossible. This problem becomes even more cumbersome when using GW eigenenergies, as working with even a relatively small number of points in the GW method can be computationally expensive.

The Wannier method allows for interpolation to very dense sampling grids because rather than relying on a Bloch state approach, it utilizes maximally-localized Wannier functions.[48] This approach is physically sound and allows for many properties to be examined in fine detail, such as electronic band structures and optical transition matrix elements.

2.5 Iterative Boltzmann Transport Equation and Electron-Phonon-Wannier (EPW)

At equilibrium, electrons are present according to the Fermi-Dirac distribution:

$$\bar{n_i} = \frac{1}{1 + \exp\left\{\frac{E - E_F}{k_B T}\right\}} \tag{2.5}$$

where E is the single particle energy and E_F is the Fermi level. This equation is valid in the absence of external forces, but when perturbations such as electric fields are considered, another tool is needed. The Boltzmann transport equation method is a semi-classical approach, where electrons are treated as classical particles but the scattering is treated quantum mechanically, as it arises from short-range forces. The key input parameters are the band structures, phonon dispersions, and the electron phonon matrix elements. It describes the statistical behavior of systems not in equilibrium and is the key method used in this work for evaluating carrier mobilities as a function of temperature.

The EPW method is a robust way for calculating a variety of electron-phonon-related properties. Using phonon eigenmodes from density functional perturbation

theory, electron-phonon coupling matrix elements can be calculated following:

$$g_{mn,v}(\mathbf{k},\mathbf{k}') = \frac{1}{\sqrt{2\omega_{\mathbf{k}'-\mathbf{k}v}}}\langle\psi_{m\mathbf{k}'}|\partial_{\mathbf{k}'-\mathbf{k}v}V|\psi_{n\mathbf{k}}\rangle \tag{2.6}$$

where $m\mathbf{k}'$ and $n\mathbf{k}$ are Kohn-Sham states, and the equation considers a scattering between the two.[49] Using this quantity, we can then calculate electron self-energies Σ:

$$\begin{aligned}\Sigma_{n\mathbf{k}}(\omega,T) =& \sum_{mv}\int_{BZ}\frac{d\mathbf{q}}{\Omega_{BZ}}|g_{mn,v}(\mathbf{k},\mathbf{q})|^2 \\ &\times\left[\frac{n_{\mathbf{q}v}(T)+f_{m\mathbf{k}+\mathbf{q}}(T)}{\omega-(\epsilon_{m\mathbf{k}+\mathbf{q}}-\epsilon_F)+\omega_{\mathbf{q}v}+i\delta}\right. \\ &+\left.\frac{n_{\mathbf{q}v}(T)+1-f_{m\mathbf{k}+\mathbf{q}}(T)}{\omega-(\epsilon_{m\mathbf{k}+\mathbf{q}}-\epsilon_F)-\omega_{\mathbf{q}v}+i\delta}\right]\end{aligned} \tag{2.7}$$

where ϵ_F is the Fermi energy, $n_{\mathbf{q}v}(T)$ is the Bose-Einstein distribution, and $f_n\mathbf{k}(T)$ is the electronic occupation at band n and wave vector $\mathbf{k}$, and δ is a fitting parameter. The carrier self-energy gives information on the scattering rate, where frequent scattering leads to an overall reduced carrier mobility.

Electron mobilities can be calculated using the iterative Boltzmann transport equation (BTE)[50]:

$$\begin{aligned}\partial_{E_\beta}f_{n\mathbf{k}} =& e\frac{\partial f^0_{n\mathbf{k}}}{\partial\epsilon_{n\mathbf{k}}}v_{n\mathbf{k},\beta}\tau^0_{n\mathbf{k}}+\frac{2\pi\tau^0_{n\mathbf{k}}}{\hbar}\sum_{\mathbf{m}v}\int\frac{d\mathbf{q}}{\Omega_{BZ}}|g_{mnv}(\mathbf{k},\mathbf{q})|^2 \\ &\times\big[(1+n_{\mathbf{q}v}-f^0_{n\mathbf{k}})\delta\epsilon_{n\mathbf{k}}-\epsilon_{m\mathbf{k}+\mathbf{q}}-\hbar\omega_{\mathbf{q}v}) \\ &+(n_{\mathbf{q}v}+f^0_{n\mathbf{k}})\delta(\epsilon_{n\mathbf{k}}-\epsilon_{m\mathbf{k}+\mathbf{q}}+\hbar\omega_{\mathbf{q}v})\big]\partial_{E_\beta}f_{n\mathbf{k}+\mathbf{q}}\end{aligned} \tag{2.8}$$

where $\frac{1}{\tau^0_{n\mathbf{k}}}$ is the relaxation time. The equation is iterative because it is solved self-consistently for $\partial_{E_\beta}f_{n\mathbf{k}}$, and an analogous expression is used for holes. By knowing the

carrier mobilities of various materials, it is possible to have a strong characterization of its propensity for a variety of applications requiring effective transport.

CHAPTER III

Electronic and Optical Properties of Two-Dimensional GaN from First-Principles

3.1 Background and motivation

Gallium nitride (GaN) is an important commercial semiconductor for optoelectronic applications in the visible and near-ultraviolet part of the spectrum.[17,51] Many efforts directed at producing deep-ultraviolet light with III-nitrides utilize high-Al content AlGaN alloys grown along the polar c-axis crystallographic direction.[52] However, the low light-extraction efficiency and the lack of deep-UV-transparent p-type contacts limit the overall efficiency of deep-UV AlGaN LEDs.[21] On the other hand, devices employing atomically thin GaN quantum wells and tunnel injection achieve deep-UV light emission[53] in the desirable spectral range for sterilization applications.[54] These atomically thin wells also exhibit strong excitonic effects[55] even at room temperature that may improve the internal quantum efficiency.[56] The suppression of the quantum-confined Stark shift[55] improves the internal quantum efficiency as well[57] and stabilizes the emission wavelength as a function of power.[58]

In addition to atomically thin quantum wells, freestanding two-dimensional gallium nitride (2D GaN) is also expected to demonstrate desirable properties for optoelectronic applications. Unlike other 2D materials, such as graphene or MoS_2, bulk

GaN crystallizes in the nonlayered wurtzite structure[59] and is not expected to adopt a 2D form with traditional exfoliation methods. However, 2D GaN has recently been directly synthesized experimentally via graphene encapsulation.[60] Subsequent theoretical calculations have confirmed the stability and investigated the properties of 2D GaN, as well as other III-V semiconductors.[61–63] Nevertheless, the fundamental electronic and optical properties of freestanding 2D GaN remain unexplored.

3.2 Project objectives

In this work, we investigate the electronic and optical properties of monolayer and bilayer freestanding 2D GaN. We apply first-principles calculations based on density functional (DFT) and many-body perturbation theory to predict accurate electronic band gaps, luminescence energies, and excitonic properties of monolayer and bilayer 2D GaN as a function of strain. Our results suggest that 2D GaN is a promising material for nonlinear optics, energy-efficient display applications, and germicidal and water-purification processes.

3.3 Methods

Our first-principles calculations are based on DFT and many-body perturbation theory. DFT structural relaxation calculations were performed using the local density approximation (LDA) for the exchange-correlation functional[64,65] within Quantum ESPRESSO[66] using a plane-wave basis and norm-conserving pseudopotentials. The 4s, 4p, and 3d electrons of Ga were included in the valence. The relaxed in-plane lattice constant is in good agreement with experimental values for bulk GaN (3.19 Å),[67] being underestimated by only 0.77%. Hydrogen atoms of integer charge were included to passivate surface dangling bonds. In simulations, it is common to passivate surface dangling bonds of the polar surfaces of compound semiconduc-

tors with fictitious hydrogen atoms of partial charge to eliminate charge transfer.[68] However, in our simulations we are interested in examining the physical effects of hydrogen passivation, including charge transfer to 2D GaN, and hence we use hydrogen pseudopotentials of integer charge. Furthermore, our choice of pseudopotential is supported by our formation-energy calculations, which confirm that full hydrogen passivation of surface bonds is energetically favorable for the monolayer. A buckled geometry of 2D GaN was investigated, as passivation makes it more stable than the planar variant.[60] Phonon calculations with density functional perturbation theory[41] and the frozen phonon method[69] (Appendix A) were used to explore the mechanical stability of the investigated structures. (Figure A.1) DFT calculations were carried out with an 8×8×1 Monkhorst-Pack mesh. To obtain converged band gap values, an artificial dipole was included in the vacuum space between periodic slabs. The technical details are analyzed in previous work.[70] The magnitude of the dipole is chosen to cancel out the artificial electric field in the vacuum region between periodic images of the slabs [i.e., the slopes of the corrected electrostatic potential curves become zero away from the slab, Figure 3.1 c,d]. The band structures were calculated with the G_0W_0 method[44] as implemented in the BerkeleyGW package.[43] The GW calculations employed semicore norm-conserving pseudopotentials which consider Ga 3s, 3p, and 3d orbitals to be valence states.[71] A plane wave cutoff energy of 250 Ry converges semicore pseudopotential DFT eigenvalues to within 20 meV. To eliminate interaction between periodic images, a Wigner-Seitz slab truncation was applied to the Coulomb interaction.[72] Simulation cell volumes included vacuum space oriented perpendicularly to the slabs such that 99% of charge density was contained within half the cell. Also employed in the GW method were the Hybertsen-Louie generalized plasmon-pole model[44] for the dielectric response's frequency dependence and the static remainder approach[73] to speed up summation convergence over unoccupied states. Quasiparticle band structure calculations were performed using a converged

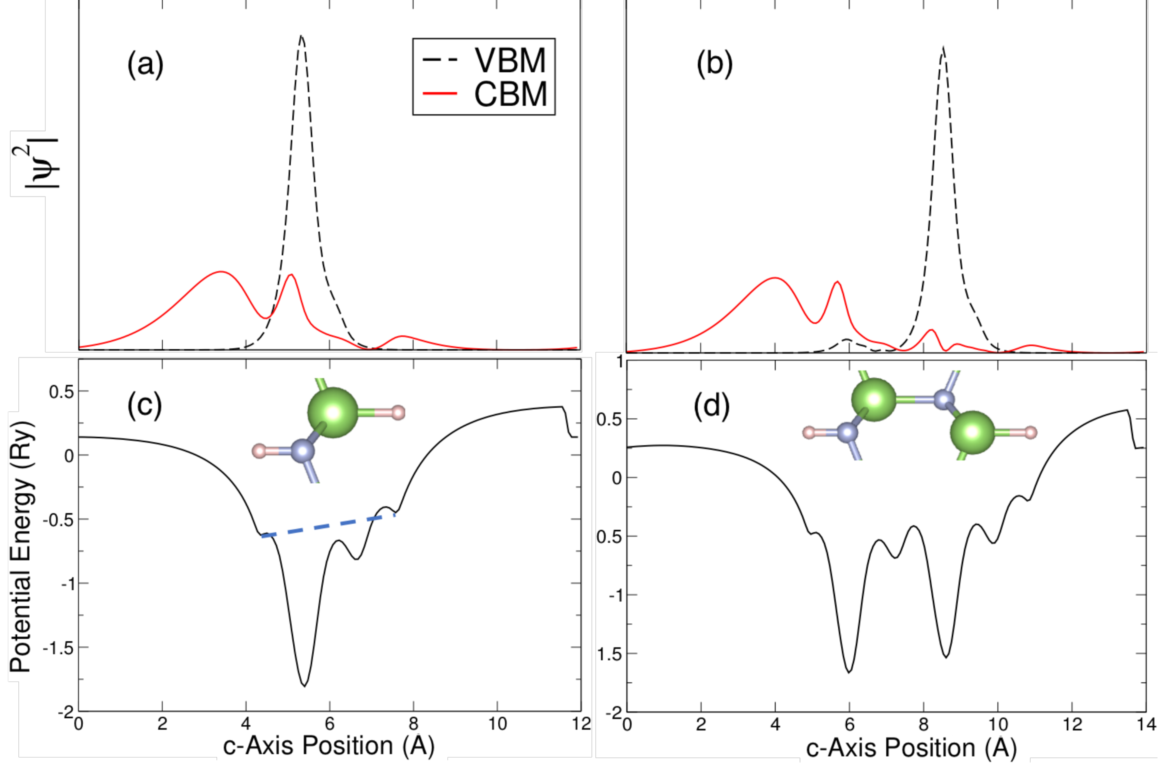

Figure 3.1: Electron and hole wave functions squared for (a) monolayer and (b) bilayer 2D GaN, and plane-averaged electrostatic potentials for (c)monolayer and (d) bilayer 2D GaN. The polarization fields within each structure spatially separate electrons and holes. The artificial dipole correction in the vacuum region is necessary to cancel out artifacts of the periodic boundary conditions. The distance and slope between peaks of like atoms, indicated by the dashed line in (c), allow for the calculation of the internal electric field magnitude.

screening cutoff energy of 34 Ry and summing over unoccupied states with energy up to 50% of the screening cutoff. Sampling grids included 8×8×1, 10×10×1, 12×12×1, and 16×16×1 Monkhorst-Pack meshes, and converged values were obtained from extrapolation (Figure A.2) in a manner consistent with previous work.[74] Quasiparticle band structures were determined by modifying the DFT-level band energies with a scissors-shift operator constructed from GW quasiparticle corrections. (Figures A.3 and A.4) Finally, exciton binding energies were calculated using the Bethe-Salpeter equation (BSE) method. The top three valence bands and the lowest conduction band were included in this calculation.

3.4 Energetics of formation and hydrogen-passivation

We performed formation-energy calculations to understand the energetics of formation and H-passivation of 2D GaN. Our results agree with Al Balushi et al. that the hydrogenated buckled structure is the most stable form of 2D GaN.[60] Our calculated enthalpy of hydrogenation per H_2 molecule is -1.102 eV for the monolayer and -1.551 eV for the bilayer relative to the unpassivated buckled structures. Moreover, the formation enthalpy of H-passivated 2D GaN with respect to bulk GaN and the H_2 molecule is -109 meV for monolayer GaN and 82 meV for bilayer GaN. H-passivated monolayer GaN is therefore a thermodynamically stable compound, while the H-passivated GaN bilayer is a metastable structure.

3.5 Electronic properties

The interfacial polarization from opposing gallium-and nitrogen-terminated surfaces gives rise to a strong inherent electric field perpendicular to the 2D layer, which works against the effect of quantum confinement and reduces the band gap. The magnitude of the electric field is calculated to be 74 MV/cm in monolayer GaN and 65 MV/cm in bilayer GaN, as determined by the slope of the plane-averaged electrostatic potential between the H atom minima (Figure 3.1 c,d). The electric-field values determined from the dipole moment of the structure along the perpendicular axis are of similar order. These electric-field values are remarkably larger than the breakdown voltage of bulk GaN (3.3 MV/cm)[75] but they do not cause band gap closure or impact ionization since the slab thicknesses are sufficiently small such that carriers cannot be accelerated to high energies. On the other hand, these polarization fields introduce a slope to the energy bands and separate electrons from holes, similar to strained nitride quantum wells.[57] The polarization fields separate the electron and hole wave functions (Figure 3.1 a,b) and lower the gap (quantum confined Stark

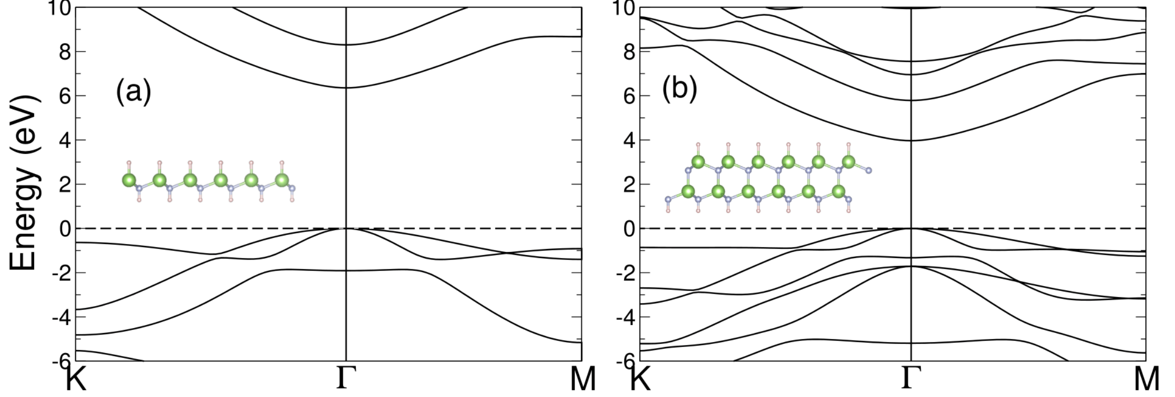

Figure 3.2: Quasiparticle band structures of (a) monolayer and (b) bilayer 2D GaN. Both materials exhibit a direct gap at Γ. The polarization fields counteract the effects of confinement in the bilayer structure.

	Monolayer		Bilayer	
	Freestanding	Embedded[55]	Freestanding	Embedded[55]
Band Gap (eV)	6.32	4.76-5.44	4.00	4.55-4.69
Exciton Binding Energy (eV)	1.31	0.10-0.21	0.75	0.10-0.17
Optical Gap (eV)	5.01	4.66-5.23	3.25	4.45-4.52

The freestanding GaN values are obtained from extrapolation (Appendix A). Embedded values are from GaN wells within AlN barriers.[55]

Table 3.1: Band Gaps, Binding Energies, and Optical Gaps of 2D GaN

effect), counteracting the band gap increase caused by quantum confinement. The lack of inversion symmetry further enables nonlinear optical properties.[42]

The quasiparticle band structures of 2D GaN are shown in Figure 3.2. Both the valence band maximum (VBM) and conduction band minimum (CBM) occur at Γ for both structures. The VBM is primarily composed of N 2p orbitals while the CBM is a hybridization of Ga 4s, Ga 4p, N 2s, and H 1s states in both structures. The DFT band gap of monolayer GaN is 2.95 eV, which is larger than the DFT gap of bulk GaN (1.79 eV) due to quantum confinement. However, bilayer GaN exhibits a DFT

band gap of 1.32 eV that is surprisingly lower than the bulk value. The reason for the gap reduction in bilayer GaN compared to bulk is the Stark effect due to the strong polarization field. However, DFT/LDA significantly underestimates semiconductor band gaps, hence GW corrections are needed to obtain accurate gap values. The GW band gap of monolayer GaN was found to be 6.32 eV, and the band gap of bilayer GaN is 4.00 eV (Table 3.1). The converged band gap values are listed in Table 3.1 and compared to atomically thin GaN wells surrounded by AlN barriers, which were presented in previous work.[55] The disparity between the freestanding and the AlN-embedded 2D GaN is due to the polarization fields. As the polarization fields in freestanding 2D GaN are not screened by the surrounding vacuum, the gap is more strongly affected by the quantum-confined Stark effect. While the electric field is stronger in the monolayer than the bilayer structure, the small thickness of the slab inhibits the spatial separation of electrons and holes, hence the Stark effect on the gap is small.

3.6 Optical and excitonic properties

Excitonic effects are also much stronger in 2D GaN compared to the bulk counterpart. The lowest-exciton binding energy in monolayer GaN is 1.31 eV, whereas in bilayer GaN the binding energy is 0.75 eV. Both values are more than 1 order of magnitude larger than bulk GaN (0.02 eV),[76] due to the increased electron-hole interaction strength caused by quantum confinement. Subtracting the exciton binding energies from the band gap yields a lowest-exciton (i.e., luminescence) energy of 5.01 eV for monolayer GaN, which is comparable to the value of AlN-embedded monolayer-GaN quantum wells. The lowest-exciton energy in bilayer GaN is 3.25 eV, which is slightly smaller than the luminescence energy of bulk GaN. Our results therefore demonstrate that the effects of confinement and Stark effect on the carriers and excitons cancel each other out in bilayer GaN. For thicker structures, we antic-

ipate that the Stark-effect contribution dominates, and the luminescence energy is lower than the bulk. However, in these thicker structures the polarization fields are more effectively screened by free carriers, and the quantum-confined Stark effect is suppressed.

We further evaluated the radiative lifetimes of excitons in monolayer and bilayer 2D GaN. We first determined the singlet-triplet exchange splitting energies to be 63 meV for monolayer GaN and 6 meV for bilayer GaN. The monolayer value is large compared to $k_B\tau$ at room temperature and below; hence excitons in the monolayer predominantly occupy long-lived triplet states with long diffusion lengths. The small exchange splitting for the bilayer implies a large thermal occupation of singlets and shorter radiative lifetimes and diffusion lengths. Following the methodology developed for evaluating radiative exciton lifetimes in two-dimensional materials,[77] the effective radiative lifetime τ_{eff} at room temperature is calculated as the thermal average of the radiative lifetimes τ_S of exciton states S according to

$$\langle\tau_S\rangle = (\frac{8\pi e^2 E_s(0)}{\hbar^2 c}\frac{\mu_S^2}{A_{uc}})^{-1}\frac{3}{4}(\frac{E_S(0)^2}{2M_S c^2})^{-1}k_B T \tag{3.1}$$

and

$$\langle\tau_{eff}\rangle^{-1} = \frac{\sum_S \langle\tau_S\rangle^{-1} e^{-\frac{E_S(0)}{k_B T}}}{\sum_S e^{-\frac{E_S(0)}{k_B T}}} \tag{3.2}$$

where μ_S is the exciton effective mass, A_{uc} is the area of the unit cell, μ_S^2 is the square modulus of the BSE exciton transition dipole divided by the number of 2D k-points, and $E_S(0)$ is the exciton energy calculated using the BSE method. We assumed the effective mass of electrons and holes to be the same as in bulk GaN (0.2 m_e and 1.4 m_e, respectively). The BSE calculation includes the top three valence bands and the lowest conduction band, while the Brillouin zone was sampled with 8×8×1, 10×10×1, 12×12×1, and 16×16×1 Monkhorst-Pack meshes. Converged values were

obtained from extrapolation to an infinitely dense grid. We determined the thermally averaged radiative lifetimes $\langle \tau_{eff} \rangle$ of singlet excitons at 300 K to be 0.6 and 4.6 ns for monolayer and bilayer GaN, respectively. These values are comparable to those of other 2D semiconductors[77] and approximately 1 order of magnitude shorter than typical values in InGaN LEDs for typical free-carrier densities ($5\times10^{18} cm^{-3}$).[56] The shorter exciton lifetimes in 2D GaN may be beneficial for improved internal quantum efficiency, as well as telecommunication (Li-Fi) applications.

3.7 Strain effects

Since in-plane strain is a viable method of tuning the electronic properties of atomically thin materials[78,79] we also explore the effect of strain on the luminescence properties of 2D GaN. We applied both compressive and tensile in-plane biaxial strain of up to 5%. Our results (band gap calculated with DFT and adjusted to account for the zero-strain GW and BSE corrections, Figure 3.3) show that increasing tensile strain first increases the band gap, and subsequently leads to a small decline. On the other hand, compressive strain monotonically reduces the gap by up to 0.3 eV for a 5% strain. To understand these trends, we examined the electron and hole wave functions as a function of strain (Figure A.5). Electrons and holes are spatially separated due to the inherent polarization field. While the hole wave function is fully confined inside the slab, the electron wave function noticeably extends beyond the edge of the slab and is only weakly bound within the potential well of the structure. Tensile in-plane strain reduces the thickness of the slab and hence the electron-hole separation, while compressive strain further shifts the electron probability to the surface of the slab, amplifying the Stark effect and the gap reduction (Appendix A). The gap decrease at large tensile strains likely results from the interplay between the quantum-confined Stark shift and the gap reduction by the deformation potential. The crystal-field splitting for ±5% biaxial strain spans a range of 1.28-2.80 eV and 0.80-1.63 eV for

	Monolayer GaN	
	m^*_{hh}	m^*_{lh}
5% Compressive Strain	3.63	1.07
Unstrained	4.59	1.00
5% Tensile Strain	4.50	1.04

Table 3.2: Hole Effective Masses of Monolayer GaN

monolayer GaN and bilayer GaN, respectively. Hole effective masses in monolayer GaN as a function of strain are listed in Table 3.2.

We also investigated the effect of uniaxial compressive and tensile in-plane strain of up to 5% on the luminescence properties. The uniaxial strain breaks the in-plane symmetry and lifts the degeneracy of the top two N 2p valence bands, resulting in optical polarization. The in-plane Poisson ratio is 0.35 for compressive strain and 0.1 for tensile strain along the directions denoted in Figure 3.4. The band gap values inFigure 3.4 are estimated using DFT. For the unstrained monolayer GaN GW corrections increase the crystal-field splitting (i.e., the energy difference between the topmost two degenerate valence bands and the third from the top at Γ) from the DFT value of 1.837 to 2.360 eV, that is, an increase of 22%. Because the topmost three valence bands of GaN are of the same N 2p orbital character, we expect that quasiparticle corrections will similarly increase the DFT degeneracy splitting due to strain. Compressive strain results in a larger heavy and light hole splitting than tensile strain, but even a tensile strain of 1% is sufficient to split the bands by more than $k_B T$ at room temperature (Figure 3.4). The resulting emitted light is linearly polarized along the direction of compressive strain. Polarized light emission is also evident from the anisotropic optical absorbance spectra of uniaxially strained 2D GaN (Figure A.6).Polarized light emission at room temperature is therefore possible with 2D GaN, which is desirable for energy-efficient display applications. The emission wavelength of the polarized luminescence can be further adjusted in the visible range

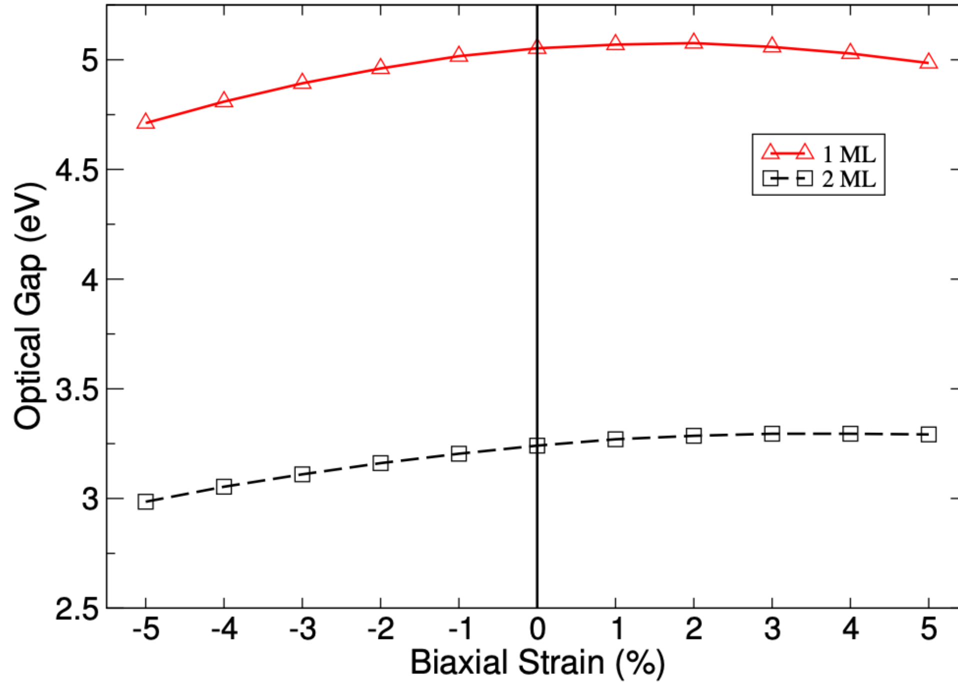

Figure 3.3: Optical gap of monolayer and bilayer 2D GaN as a function of biaxial strain. Compressive strain is a viable method for controlling the band gap of both structures. These results were determined from the DFT gap as a function of strain adjusted to account for the GW and BSE corrections at zero strain.

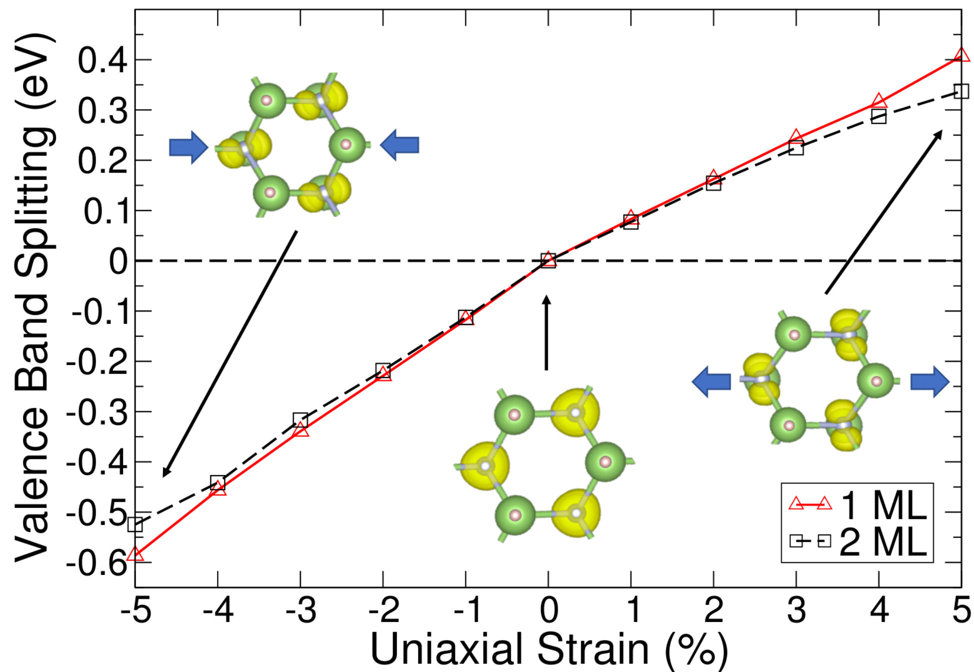

Figure 3.4: Energy splitting between the heavy and light holes of monolayer and bilayer GaN as a function of uniaxial strain. Uniaxial strain lifts the band degeneracy, resulting in polarized light emission along the axis of compressive strain.

by alloying with InN to form 2D InGaN.

3.8 Conclusions

In conclusion, we investigated the electronic and optical properties of 2D GaN as a function of thickness and strain with predictive calculations. Monolayer 2D GaN emits light in the deep-UV range, which is promising for sterilization applications. The long-lived stable triplet excitons of the monolayer may be promising for excitonic applications. Uniaxial in-plane strain results in linearly polarized light emission desirable for display applications. Our results demonstrate that 2D GaN exhibits an array of desirable functional properties and is a synergistic compound between established semiconductors and 2D materials.

CHAPTER IV

Effect of Stacking Orientation on the Electronic and Optical Properties of Polar 2D III-nitride Bilayers

4.1 Background and motivation

Group-III nitrides find broad commercial applications in visible optoelectronic devices. Recently, AlGaN alloys have been investigated for sterilization and water purification applications, owing to their emission in the ultraviolet (UV).[52] Yet, their overall efficiency is limited by difficulties in light extraction and p-type doping.[21] However, these problems may be alleviated in two-dimensional (2D) nitride materials such as atomically thin GaN quantum wells, which emit deep-UV light[80] and may have a higher internal quantum efficiency,[56] owing to their strong room-temperature excitonic effects.[81] Given the successful synthesis of 2D GaN[60,82] and its applicability in optoelectronic devices, investigations into the properties of 2D III-nitride materials have become compelling. Al Balushi et al. confirmed that the band gap of 2D GaN is much wider than its bulk counterpart,[60] opening up new avenues for the broad applicability of GaN. Further synthesis efforts have been directed at the other 2D III-nitrides. Hexagonal BN is readily available, and graphite-like hexagonal AlN nanosheets have been epitaxially grown on single crystal Ag(111),[83] but 2D InN

remains challenging to synthesize, though thin films have been grown on GaN (0001) by molecular-beam epitaxy.[84]

As experimental techniques continue to improve, there is a clear need for computation to ascertain the theoretical limits of these materials with respect to functional properties. Work on 2D GaN quantum wells embedded in AlN capping layers has shown that the band gap of GaN monolayers and bilayers are tunable over a broad range by varying the capping thickness of the AlN layers.[55] By comparing to work on freestanding monolayers and bilayers,[85] it becomes clear that the capping layers significantly lower the band gap and exciton binding energies. With these two scenarios having been explored, giving more information on properties with respect to environmental effects, there is now a question of how internal structural properties within vdW heterostructures affect the resulting properties.

The noncentrosymmetric (wurtzite) structure of the III-nitrides gives rise to a strong inherent electrical polarization along the polar c-axis crystallographic direction,[86] which, among many other phenomena, leads to the formation of 2D electron gases at GaN/AlGaN heterojunctions.[87] A unique feature of hydrogen-passivated tetrahedral 2D nitrides is the lack of reflection symmetry across the 2D plane that, in combination with the reduced screening in the 2D regime,[88] amplifies the magnitude of this intrinsic polarization field to values (74 MV/cm)[85] that exceed the critical dielectric breakdown field (3.3 MV/cm)[75] by more than an order of magnitude. The unique combination of strong electrical polarization with quantum confinement in atomically thin nitrides may give rise to distinct functional properties compared to their bulk counterparts or other nonpolar 2D materials for potential applications in optoelectronic devices. Moreover, multilayer structures of 2D nitride monolayers in which the electrical polarization of the constituent layers can be aligned in a parallel or antiparallel fashion enable further control of the functional properties.

4.2 Project objectives and overview

In this work, we investigate the electronic properties of hydrogen-passivated, monolayer BN, AlN, GaN, and InN, as well as their bilayer structures, treating the polarization of each layer as an additional degree of freedom. Our calculations reveal that III-nitride monolayer stacks with aligned polarizations have narrower band gaps than the isolated monolayers due to the strong quantum-confined Stark shift (QCSS) arising from the large inherent polarizations. On the other hand, the band gaps of stacks with opposite polarizations are comparable to the isolated monolayers, due to the offset of reduced quantum confinement by the weaker QCSS. We also find that the nature of excitons (interlayer vs. direct) and luminescence energy can be controlled by the choice of parallel or antiparallel stacking orientation, respectively, while preserving their strong exciton binding and bright character. Our results show that the stacking orientation acts as an additional degree of freedom to engineer the electronic, excitonic, and optical properties of polar 2D materials.

4.3 Methods

Our first-principles calculations utilize density functional theory (DFT) and many-body perturbation theory. Structural relaxation calculations were carried out in DFT using the local density approximation (LDA) for the exchange-correlation potential[64,65] within Quantum ESPRESSO[66] using a plane-wave basis and norm-conserving pseudopotentials. Hydrogen atoms of integer charge were included to passivate surface dangling bonds. DFT and GW calculations were carried out with an $8\times8\times1$ Monkhorst-Pack mesh for the sampling of the first Brillouin zone. To obtain converged band gap values, an artificial dipole was included in the vacuum space between periodic slabs to counteract the artificial electric field introduced by the periodic boundary conditions for polar structures, as in previous work.[70] Phonon frequencies

were found using density functional perturbation theory (DFPT).[41] Quasiparticle band structures were calculated using the one-shot G_0W_0 method[44] within BerkeleyGW.[43] Semicore pseudopotentials for Ga and In were used, which treat the Ga 3s, 3p, and 3d orbitals and the In 4s, 4p, and 4d, orbitals as valence states.[71] The DFT eigenvalues are converged to within 1 meV/atom using a plane-wave cutoff of 100 Ry for BN and AlN and 250 Ry for GaN and InN. A Wigner-Seitz slab truncation was applied to the Coulomb potential[72] to eliminate the artificial interaction between periodic images. The simulation cell included sufficient vacuum space in the direction perpendicularly to the slabs such that 99% of the charge density was contained within half the cell. Quasiparticle band-structure calculations were performed using dielectric-matrix screening cutoff energies of 35, 30, 34, and 36 Ry for BN, AlN, GaN, and InN, respectively. The Hybertsen-Louie generalized plasmon-pole model was employed for the frequency dependence of the dielectric function,[44] and the static remainder approach[73] was used to accelerate the convergence of the summation over unoccupied states. Unoccupied states with energies up to 50% of the screening cutoff were included in the summation. Quasiparticle band structures were plotted by modifying the DFT band structures with a scissors-shift operator constructed from GW quasiparticle corrections. Exciton binding energies were calculated using the Bethe-Salpeter Equation (BSE) method[46] as implemented in BerkeleyGW,[43] where the top three valence bands and lowest three conduction bands were included. The radiative exciton lifetimes were calculated with the method of Palummo et al.[77]

4.4 Thermodynamics and surface passivation

We first performed thermodynamic calculations to understand the surface passivation of surface dangling bonds in III-nitride monolayers by hydrogen atoms. $2\times2\times1$ supercells were constructed, and hydrogen atoms symmetrically attached to either 0%, 25%, 50%, 75%, or 100% of the III-nitride pairs. Following earlier work,[89–91] we

calculate the Gibbs free energy difference as a function of the fraction of hydrogen passivated sites under different temperatures and hydrogen partial pressures via eq. (4.1) – (4.3),

$$\Delta G(T,P) = G_{slab}^{passivated}(T,p,N_H) - G_{slab}^{unpassivated}(T,p,N_H) - N_H G_H(T,p) \quad (4.1)$$

$$G_{slab}^{passivated}(T,p,N_H) = E_{slab}^{(un)passivated} + ZPE_{slab}^{(un)passivated} - T(S_{vib}) \quad (4.2)$$

$$G_H(T,p) = \frac{1}{2}(E_{H_2} + ZPE_{H_2} - T(S_{trans} + S_{rot} + S_{vib})) \quad (4.3)$$

where $\Delta G(T,p)$ is the change of Gibbs free energy of hydrogen-passivated structures with respect to the unpassivated structure, $G_{slab}^{(un)passivated}$ is the Gibbs free energy of a hydrogen-(un)passivated slab, $E_{slab}^{(un)passivated}$ is the total free energy of a hydrogen-(un)passivated slab from DFT calculations, T is the temperature, p is the hydrogen partial pressure, N_H is the number of hydrogen atoms, G_H is the Gibbs free energy of one hydrogen atom, E_{H_2} is the total free energy of a hydrogen molecule from DFT calculation, ZPE is the zero point energy from DFPT calculations, and S_{trans}, S_{rot}, and S_{vib} are translational, rotational, and vibrational entropies for different structures, respectively. The vibrational entropy is evaluated using the calculated phonon frequencies and the temperature derivative of the phonon free energy.[92] As shown in Figure 4.1, at a given hydrogen pressure and temperature the III-nitride monolayers assume either a fully passivated, buckled tetrahedral structure (similar to the tetrahedral wurtzite structure) or an unpassivated, planar hexagonal structure (akin to the hexagonal structure of bulk BN). Our results show that monolayer BN assumes a planar, unpassivated structure under standard atmospheric conditions (as expected from experimental results of its chemical inertness and also reported in previous cal-

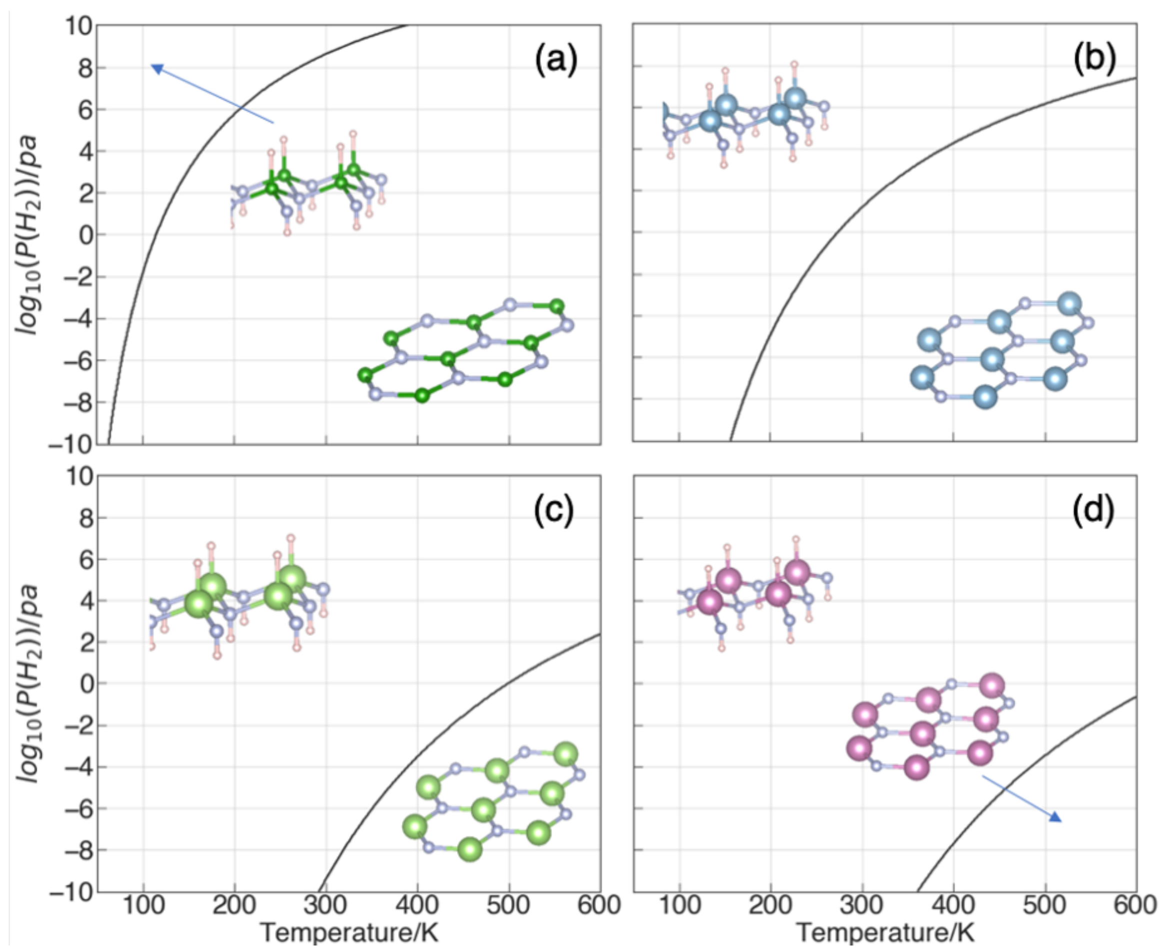

Figure 4.1: Preferred passivation state of (a) BN, (b) AlN, (c) GaN, and (d) InN monolayer as a function of hydrogen partial pressure (Pa) and temperature (K). Under standard room-temperature conditions, BN adopts a planar hexagonal, unpassivated structure, and AlN, GaN, and InN adopt buckled tetrahedral, passivated structures.

culations[93,94]) while monolayer AlN, GaN, and InN adopt the buckled, passivated structure (similar to their bulk tetrahedral wurtzite crystal structures). However, under standard hydrogen pressure but higher temperatures, such as those needed during the synthesis process, AlN is more stable as a planar, unpassivated material. Other work has also found that monolayer AlN adopts the buckled form under standard conditions,[95] which suggests that functional properties might be tunable by controlling the growth temperature. Finally, the formation of a heterostructure is unlikely to change the preferred passivation state, as the bilayer interaction energy (on the order of 0.04 eV/unit cell) is much smaller than the energy needed for dehydrogenation (on the order of 1 eV/unit cell).

4.5 Electronic properties

A visualization of the nitride heterostructures is shown in Figure 4.2, and the quasiparticle band structures of monolayer BN, AlN, GaN, and InN as well as each of their three bilayer structures are presented in Figure 4.3. Structural properties are shown in Table 4.1. All passivated BN, GaN, and InN structures exhibit a direct band gap while the gaps of AlN structures are indirect. The band gaps span a broad spectrum in the visible and UV range, ranging from 1.9 eV for aligned BN to 7.7 eV for antialigned N-interposed AlN. As a comparison, Prete et al. report unpassivated nitride monolayers yield band gap values of 1.7 eV (direct) for InN, 4.5 eV (direct) for GaN, 5.8 eV (indirect) for AlN, and 6.7 eV (indirect) for BN.[96] Furthermore, as discussed in earlier work,[97] strong polarization fields can cause band inversion and produce a topologically insulating state. The additive nature of the electric fields for aligned multilayer 2D nitride stacks suggest that, as the number of layers increases, the Stark shift can become sufficiently strong to further reduce the magnitude of the gap and even invert the order of the valence and conduction bands of 2D BN, GaN, and InN, giving rise to topological states. Additionally, the total energy of the

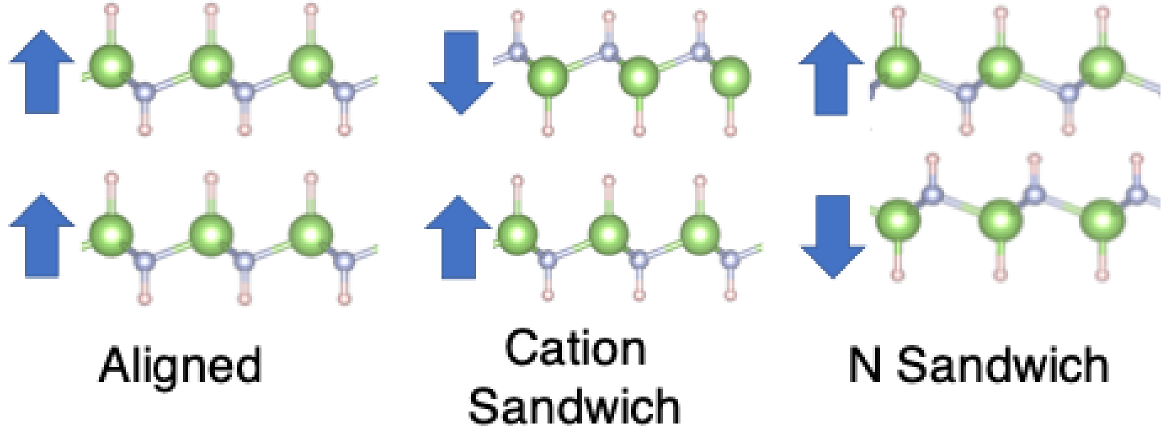

Figure 4.2: The three possible orientations of III-nitride heterostructures, where the polarization is treated as the degree of freedom. The blue arrows denote the polarization direction of each monolayer.

aligned GaN heterostructure is found to be 0.04 eV / unit cell lower than its anti-aligned counterparts, suggesting that the aligned state is the preferable configuration in these III-nitride heterostructures.

Our results also show that the counteracting effects of quantum confinement and strong electrical polarization perpendicular to the 2D planes enable the tuning of the electronic properties of the polar 2D III-nitride bilayers. Previous work found that monolayer GaN exhibits a strong polarization (74 MV/cm) as a result of charge transfer between passivating hydrogen atoms,[85] and this property is intrinsic to monolayer BN, AlN, and InN as well, owing to the fact that they all adopt the buckled tetrahedral structure when passivated with H. Yet in these monolayers, quantum-confinement effects dominate rather than QCSS - yielding wide band gaps - because electrons and holes cannot sufficiently separate in space along the out-of-plane direction. In aligned monolayers, however, the increased spatial thickness allows for carrier separation to occur. Coupled with the additive nature of the polarization, a strong QCSS is present in aligned bilayers, resulting in band gaps much narrower than those of the respective isolated monolayers. Such is the case in the aligned GaN bilayer,

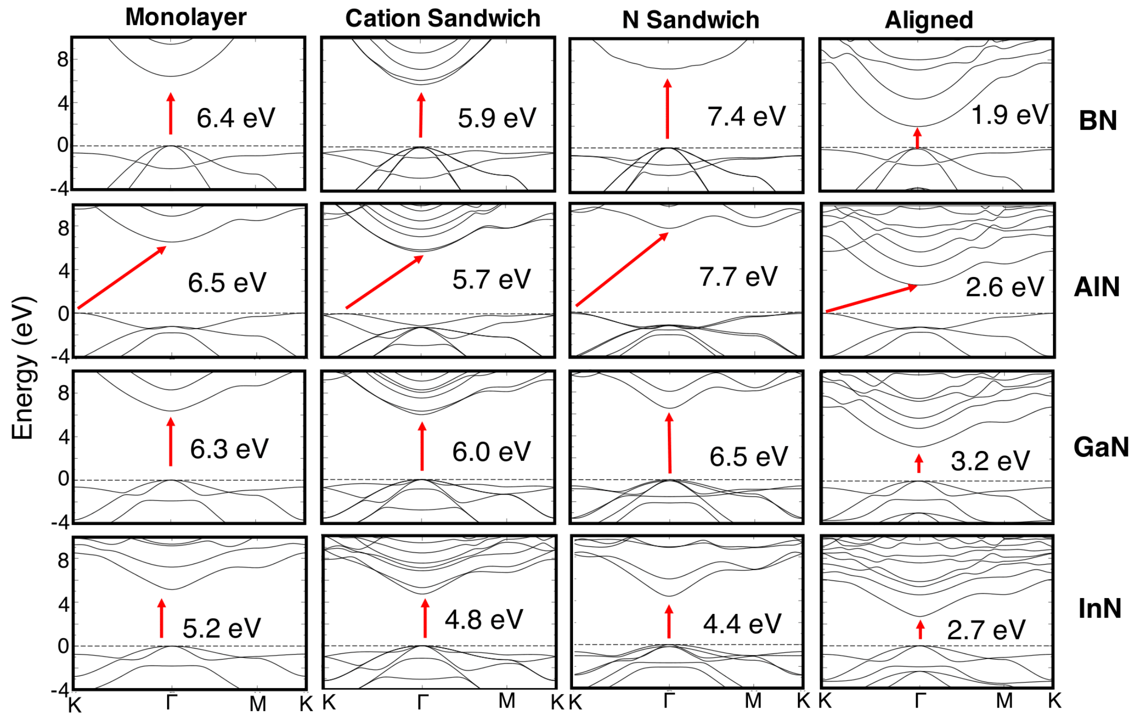

Figure 4.3: Quasiparticle band structures of the freestanding monolayer and of the bilayer stacks [aligned, antialigned with interposed cations ("cation sandwich"), and antialigned with interposed N ("N sandwich")] of BN, AlN, GaN, and InN. Red arrows denote the fundamental band gap. The high-symmetry points are Γ (0,0,0), K (1/3, 1/3, 0), and M (0.5,0,0). The band gaps of 2D III-nitride monolayers and their bilayer structures span the visible and UV ranges.

	Cation-N Bond Length (Å)	**Cation-H Bond Length (Å)**	**N-H Bond Length (Å)**	**Interlayer Distance, H-H (Å)**
Monolayer BN	1.551	1.202	1.032	N/A
BN-B Sandwich	1.551	1.204	1.035	1.758
BN-N Sandwich	1.552	1.201	1.036	1.740
BN-Aligned	1.551	1.209	1.035	1.660
Monolayer AlN	1.917	1.566	1.025	N/A
AlN-Al Sandwich	1.897	1.571	1.024	1.641
AlN-N Sandwich	1.900	1.566	1.026	0.970
AlN-Aligned	1.920	1.577	1.027	1.412
Monolayer GaN	1.966	1.547	1.020	N/A
GaN-Ga Sandwich	1.965	1.551	1.021	1.449
GaN-N Sandwich	1.965	1.547	1.023	0.852
GaN-Aligned	1.966	1.555	1.021	1.336
Monolayer InN	2.171	1.720	1.021	N/A
InN-In Sandwich	2.177	1.734	1.025	1.397
InN-N Sandwich	2.180	1.720	1.025	0.663
InN-Aligned	2.171	1.731	1.021	1.198

Table 4.1: Structural properties of III-nitride monolayers and heterostructures.

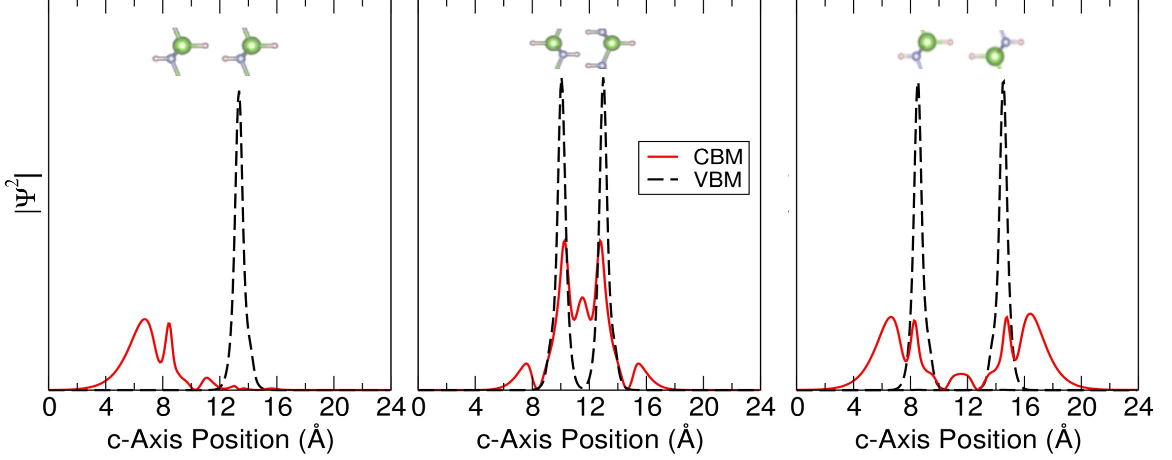

Figure 4.4: Electron and hole wave functions squared for (a) aligned, (b) antialigned with interposed N, and (c) antialigned with interposed Ga bilayers of GaN. Although the holes remain localized on the N atoms, electrons reside outside the GaN planes due to the strong out-of-plane electric dipole moment and their location can be controlled by the stacking orientation.

which has a band gap of 3.2 eV (Figure 4.3), i.e. narrower than the gap of bulk GaN (3.4 eV). In anti-aligned orientations, the band-gap magnitudes remain comparable to those of the respective monolayers. Although the larger layer thickness lowers the band gap due to a decrease in confinement, the cancellation of the polarization fields results in a band gap increase due to removal of the QCSS.

The stacking orientation of the 2D bilayers also has a strong effect on the relative location of electrons and holes. As shown in Figure 4.4, holes in 2D GaN are localized on the nitrogen atoms independent of orientation. Electrons, however, are located primarily in the vacuum region surrounding the hydrogens that passivate the nitrogen side of the individual monolayers. This property extends to 2D BN, AlN, and InN as well, and arises as a consequence of the inherent polarization of the layers. This positioning of the electrons and the fact that surface electrons are only weakly bound to the material implies that electrons in 2D nitrides are not strongly affected by atomic displacements and can conduct ballistically without being scattered by phonons or defects, suggesting applicability in fast, energy-efficient microelectronics.

4.6 Optical and excitonic properties

Moreover, the aligned polarization fields in the 2D nitride bilayers result in the formation of strongly bound interlayer excitons. Electrons and holes in aligned bilayers are localized in separate layers (Figure 4.4a), similar to $MoSe_2/WSe_2$ van der Waals interfaces.[98,99] While interlayer excitons have also been studied in embedded III-V heterostructures,[100,101] most have been limited to low-temperature applications due to the weak exciton binding. However, the reduced screening in freestanding atomically thin structures allows for strongly bound interlayer excitons which are stable at room temperature. Our calculated exciton binding energies and luminescence gaps of GaN bilayers are shown in Table 4.2. Even for the polar stacking orientation, the exciton binding energies of the bilayers remain strong (on the order of 1 eV) and comparable to the monolayer and the antialigned structures. The thermally averaged radiative lifetimes $\langle \tau_{eff} \rangle$ of singlet excitons at 300K (Table 4.2) are on the order of a few ns, i.e. comparable to the lifetimes of bright excitons in other 2D materials,[77,85] and do not vary appreciably with stacking orientation. Such short exciton lifetimes may allow for luminescence with high internal quantum efficiency, indicating the suitability of GaN bilayers for light-emission applications. Additionally, as the exciton binding energies of GaN heterostructures are comparable to that of the monolayer, the optical spectra of the GaN heterostructures are expected to be similar to the previously published optical spectrum of monolayer GaN,[85] other than the offset caused by the different band gap values.

Our results demonstrate that the luminescence energy of polar 2D nitrides can be controlled via the stacking arrangement of the bilayers, with the aligned GaN bilayer emitting in the visible and the antialigned GaN structures emitting in the ultraviolet, primarily through the control of the band gap. As the tunability results from the polar nature of the individual GaN monolayers, our results can be generalized to other stacks of polar noncentrosymmetric monolayers, suggesting a robust method

Structure	Exciton Binding Energy (eV)	Luminescence Energy (eV)	Exciton Radiative Lifetime (eV)
Ga Sandwich	1.18	4.82	7.3
N Sandwich	1.37	5.13	2.1
Aligned	1.00	2.20	2.7

Table 4.2: Exciton binding energies, luminescence energy, and exciton radiative lifetimes of GaN bilayers. The exciton binding energies remain strong (~ 1 eV) and the lifetimes short (a few ns) regardless of the stacking arrangement.

for tailoring the luminescence properties of polar 2D materials. In addition, the properties of interlayer excitons in 2D transition-metal dichalcogenides can be further tuned via an externally applied voltage, highlighting the propensity of these materials for novel optoelectronic and excitonic devices.[102,103] These observations highlight the suitability of bilayers of polar 2D materials for controlling the nature and lifetime of excitons in semiconductor heterostructures.

4.7 Conclusions

In conclusion, we applied first-principles computational methods to investigate the effect of stacking orientation on the electronic and optical properties of polar 2D III-nitride bilayers. By treating the polarization orientation as an additional degree of freedom in the bilayer design, the electronic band gap can be tuned over several eVs. Furthermore, the nature of excitons (interlayer vs. direct) can be controlled by the choice of parallel or antiparallel stacking orientation, respectively, while preserving the strong exciton binding energy (~ 1 eV) and short radiative lifetime (few ns). Our results demonstrate that the electronic and optical properties of 2D III-nitride bilayers can be widely controlled over the visible and UV ranges by the choice of stacking

orientation, highlighting their promising applications in excitonic and optoelectronic devices.

CHAPTER V

Carrier Mobility of Copper (I) Oxide

5.1 Background and motivation

Cu_2O is a well-established semiconductor. It is p-type dopable, nontoxic, and low cost, making it ideal for a wide variety of applications. In particular, its direct band gap of 2.17 eV[104] makes it of interest for solar cell applications and photocatalysis.[105,106] Additionally, there is significant research progress being made in elucidating its properties with respect to a thin-film transistor device setting.[107,108]

However, p-type oxides generally have relatively low hole mobilities, limiting their performance. Thus it is necessary to directly calculate the mobility of p-type Cu_2O while also gaining understanding into the fundamental mechanisms governing carrier transport, such as the phonon modes primarily responsible for carrier scattering at room temperature.

5.2 Project objectives and overview

In this work, we investigate the hole mobility of Cu_2O. I apply first-principles calculations based on density functional (DFT) and many-body perturbation theory to accurately predict electronic band gaps. The phonon-limited carrier mobility and phonon-mode-resolved imaginary self-energies are then calculated using the electron-

phonon Wannier method. Our results show that the Cu_2O room temperature hole mobility is 106 cm^2/Vs and that polar optical phonon scattering is the dominant scattering mechanism.

5.3 Methods

Our approach is based on density functional theory, many-body perturbation theory, density functional perturbation theory, and the maximally localized Wannier function method. Structural relaxation calculations were carried out in DFT using the local density approximation (LDA) for the exchange-correlation potential[64,65] within Quantum ESPRESSO[66] using a plane-wave basis and norm-conserving pseudopotentials for the valence electrons of Cu and O. The relaxed lattice constants agree well with experiment (4.27 Å)[109], being underestimated by only 0.66%. DFT and GW calculations were carried out with a $6 \times 6 \times 6$ Monkhorst-Pack mesh for the sampling of the first Brillouin zone (BZ). The DFT eigenvalues are converged to within 1 meV/atom using a plane-wave cutoff of 120 Ry. Phonon frequencies were found using density functional perturbation theory (DFPT)[41] on a $6 \times 6 \times 6$ BZ sampling grid. Electron-phonon coupling matrix elements were evaluated using the maximally localized Wannier function method[110] within the Electron-Phonon-Wannier (EPW) code,[49] using a carrier density of 10^{18} cm^{-3}, and interpolated to fine electron and phonon BZ sampling meshes up to $54 \times 54 \times 54$. Polar corrections to the electron-phonon matrix elements were applied.[111] The phonon-limited hole mobility was evaluated as a function of temperature with the iterative Boltzmann Transport Equation method[50] for carrier states within a 0.4 eV energy range from the valence band maximum.

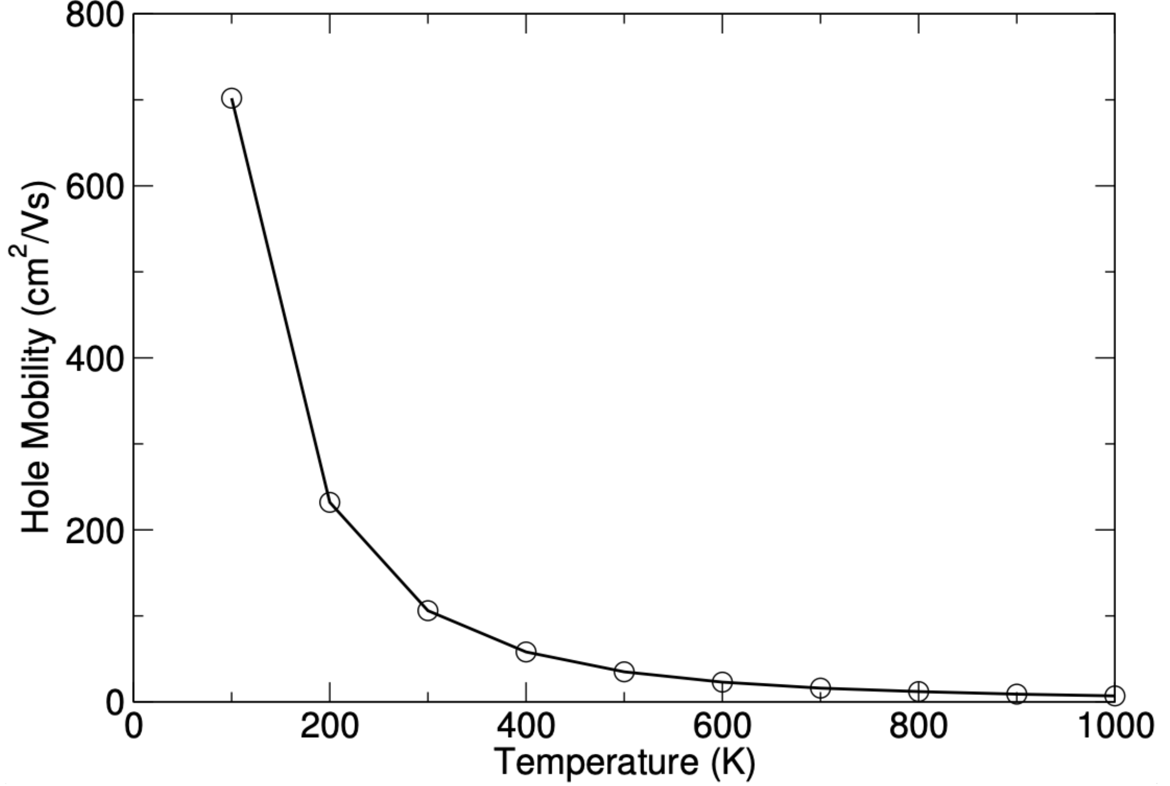

Figure 5.1: Phonon-limited hole drift mobility in Cu_2O as a function of temperature.

5.4 Carrier mobility and scattering

The calculated phonon-limited hole mobility as a function of temperature is shown in Figure 5.1. The phonon-limited mobility does not account for ionized impurities, and thus this value represents a theoretical upper limit for the mobility. However, our value for the room temperature hole mobility (106 cm^2/Vs) agrees well with some of the largest experimental values (90 cm^2/Vs[107] and 107 cm^2/Vs[112]). At high temperatures, the curve follows a $T^{-2.31}$ power law, suggesting that polar optical phonon scattering is the dominant scattering mechanism.

This result places Cu_2O in a promising place with respect to other p-type oxide semiconductors. β-Ga_2O_3 only has a room temperature hole mobility of 32 cm^2/Vs,[113] and TiO_2 has a room temperature hole mobility of 35 cm^2/Vs.[114] The higher mobility in Cu_2O suggests it can enhance the field effect mobility of thin-film transistors when

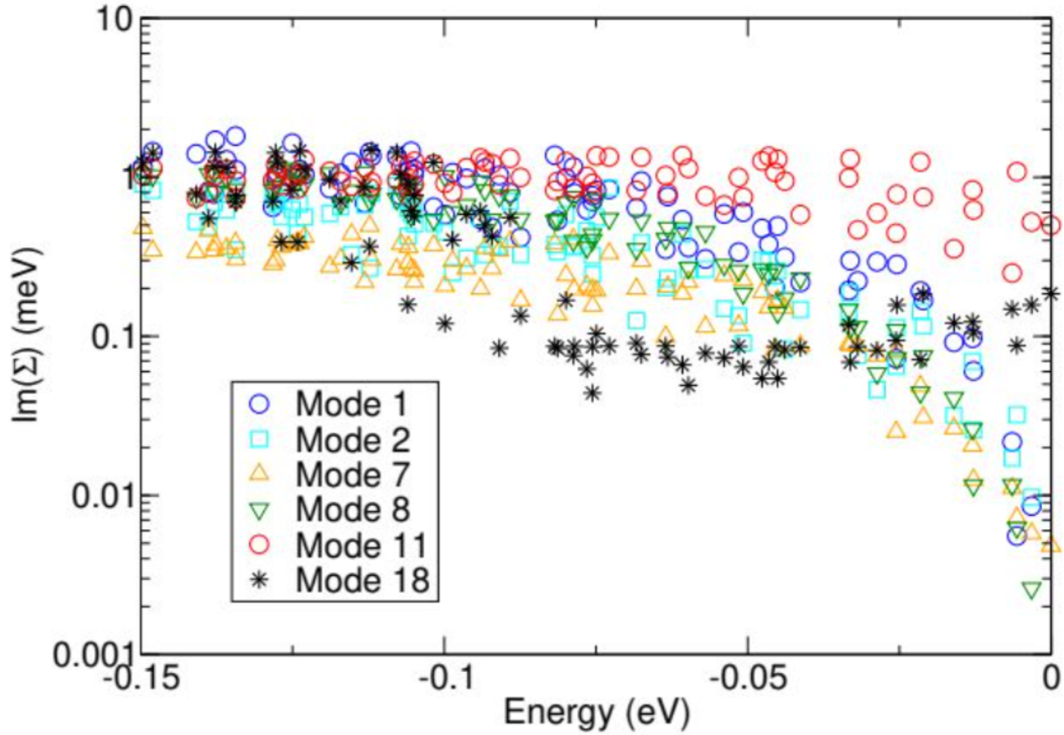

Figure 5.2: Phonon-mode-resolved imaginary self-energies as a function of the hole energy in Cu_2O. 0 eV is referenced to the valence band edge.

used as a channel material.

We can further characterize the mobility by examining the phonon-mode-resolved imaginary self-energies. The phonon modes that give non-negligible contributions to the hole scattering are shown in Figure 5.2. At higher temperatures, many modes contribute in significant amounts to the overall scattering. Near the band edge, Modes 11 and 18 give the largest contributions, where the phonons are ordered in number of increasing frequency. Thus they are the primary modes responsible for hole scattering at that temperature. Modes 11 and 18 are polar optical modes, and a visualization of the atomic displacements is shown in Figure 5.3.

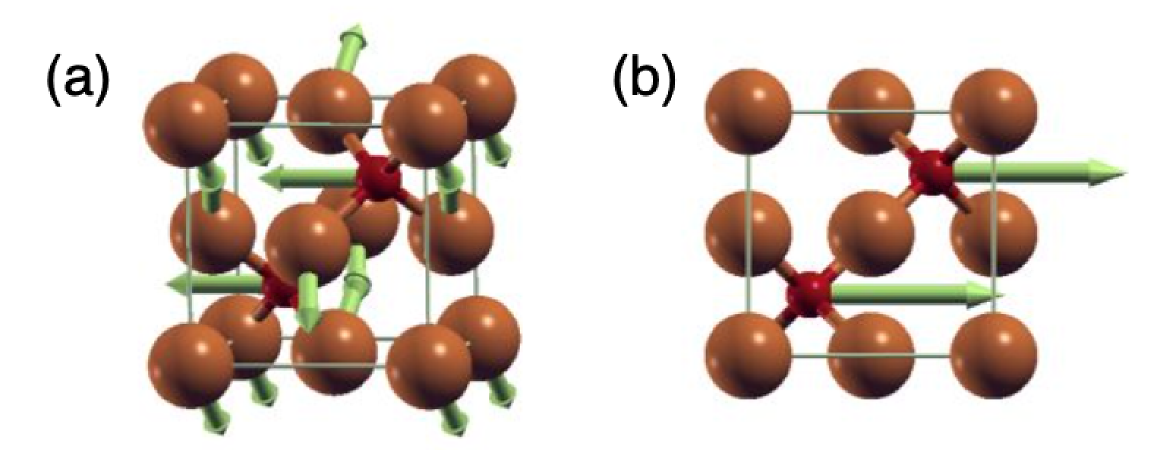

Figure 5.3: Visualization of the atomic displacements of phonon modes (a) 11 and (b) 18 of Cu_2O. The larger atoms are copper, shown in brown, and the smaller atoms are oxygen, shown in red. These polar optical modes dominate the scattering at room temperature.

5.5 Conclusions

In conclusion, we applied first-principles computational methods to investigate the phonon-limited hole mobility of Cu_2O as a function of temperature. Cu_2O has a large room temperature hole mobility compared to many other oxides, and that mobility is primarily limited by the polar optical modes. Our work shows the suitability of Cu_2O for p-type thin-film transistors and other optoelectronic applications.

CHAPTER VI

Carrier Mobility of Ultra-Wide-Band-Gap (UWBG) Semiconductors

6.1 Background and motivation

Materials are typically classified as a metal, semiconductor, or an insulator based on their band gap values. Metals have closed gaps, while insulators are often classified as having a band gap larger than 3 eV, with semiconductors bridging the divide. The ease of dopability for semiconductors in this range is part of how they have fueled the success of the electronics industry. However, materials with gaps larger than 3 eV have rapidly proved their potential. GaN has a band gap of 3.4 eV, and with its high breakdown voltage and thermal conductivity, it has significant advantages in its performance comparison against silicon-based devices, allowing it to be used in high-power optoelectronics and high-frequency devices.

Even beyond that band gap value, with values as large as 6.2 eV, materials such as AlGaN, β-Ga_2O_3, cubic BN, and diamond are rapidly proving to be strong competitors in the field of high-power electronics.[115] With the band gap criterion becoming obsolete, there is growing consensus that the dopability of a material should be the new key factor in classifying its electronic nature. Questions of particular interest in the community include the potential upper limit to the band gaps of functional semi-

conductors, the feasibility of doping ultra-wide-band-gap (UWBG) materials, and the fundamental electronic properties that these materials possess. As the prospects grow for UWBG materials to be used in devices requiring effective carrier transport, it is prudent to determine their expected properties once sufficient doping has been achieved.

The Baliga figure of merit, which provides a metric for evaluating a material's applicability for high-power electronics, scales with the cube of band gaps,[30] making this parameter critical in achieving high performance overall. Among UWBG materials, oxides tend to have larger gaps compared to nitrides and carbides. From there one can refine further by examining symmetric, atomically dense crystal structures with small cation-to-oxygen ratios, as they are expected to yield lighter hole masses due to stronger orbital overlap and reduced band folding, which is desirable for applications needing efficient p-type mobility. The resulting candidate materials are MgO, rs-BeO, wz-BeO, and zb-BeO.

6.2 Project objectives and overview

In this work, we investigate the electronic properties of zincblende BeO (zb-BeO), rocksalt BeO (rs-BeO), wurtzite BeO (wz-BeO), and rocksalt MgO (rs-MgO). We apply density functional theory and many-body perturbation theory to predict accurate band structures. We then calculate phonon-limited carrier mobilities with the EPW method. Our results suggest that these materials have large electron mobilities ($>$100 cm^2/Vs) at room temperature, giving them significant potential in the field of high-power electronics.

6.3 Methods

Our calculations on the electric properties are based on density functional theory and many-body perturbation theory. DFT structural relaxation calculations were performed using the local density approximation (LDA) for the exchange-correlation functional[64] within Quantum ESPRESSO[66] using a plane-wave basis and norm-conserving pseudopotentials. Phonon dispersions were calculated with density functional perturbation theory (DFPT).[41] Band structures were calculated with the G_0W_0 method[44] as implemented in the BerkeleyGW package,[43] using the plasmon-pole model[44] and the static remainder approach.[73] DFT and DFPT calculations were carried out with an $8 \times 8 \times 8$ Monkhorst-Pack mesh. Plane wave cutoff energies of 150 Ry and 180 Ry converge DFT and GW eigenvalues to within 4 meV for MgO and BeO polytypes, respectively. Quasiparticle band structure calculations were performed using a converged screening cutoff energy of 36 Ry for MgO and 40 Ry for the BeO polytypes. Quasiparticle band structures were plotted with Wannier90[116] by replacing the DFT eigenenergies with GW eigenenergies. Electron-phonon coupling matrix elements were evaluated using the maximally localized Wannier function method[110] within the Electron-Phonon-Wannier (EPW) code,[49] using a carrier density of 10^{18} cm^{-3}, and interpolated to fine electron and phonon BZ sampling meshes up to $120 \times 120 \times 120$. Polar corrections to the electron-phonon matrix elements were applied.[111] The phonon-limited hole mobility was evaluated as a function of temperature with the iterative Boltzmann Transport Equation method[50] for carrier states within a 0.54 eV energy range from the band extrema.

6.4 Phonons and band structures

We first calculate the phonon dispersions of MgO and the BeO polytypes to confirm mechanical stability. The dispersions are shown in Figure 6.1. MgO and wz-BeO

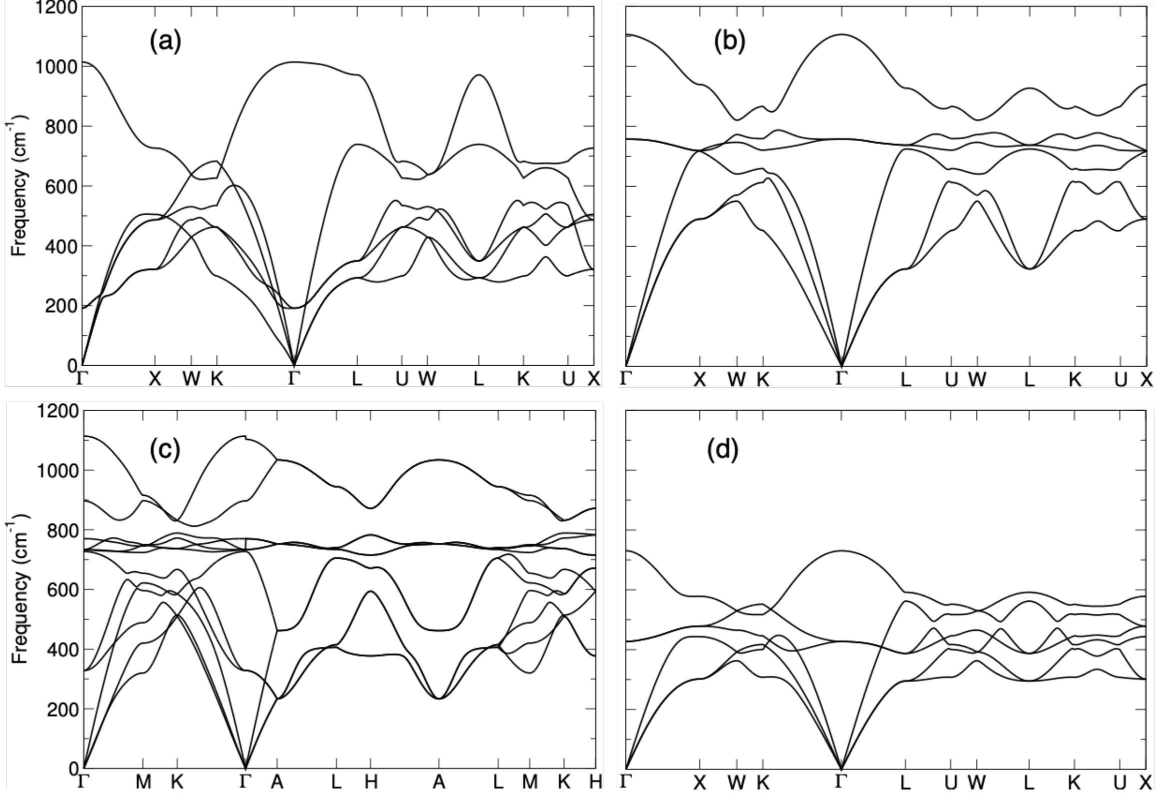

Figure 6.1: Phonon dispersions of (a) rs-BeO, (b) zb-BeO, (c) wz-BeO, and (d) MgO. All structures have positive phonon frequencies after relaxation.

are expected to have positive frequencies owing to natural occurrence at ambient pressures, and this is confirmed by DFPT calculation. zb-BeO is considered a metastable phase, but we find positive frequencies across the Brillouin zone, similar to other theoretical work.[117] rs-BeO is considered an unstable phase at atmospheric pressure,[117–119] but DFPT finds positive phonon frequencies across the zone.

We then calculate the electronic band structures of MgO and the BeO polytypes. The quasiparticle band structures are shown in Figure 6.2. rs-BeO has an indirect gap of 11.92 eV with a VBM along the Γ-K high symmetry path and a CBM at L. zb-BeO has an indirect gap of 10.52 eV with a VBM at Γ and a CBM at X. wz-BeO has a direct band gap of 11.81 eV with band extrema at Γ. MgO has a direct gap of 8.62 eV with band extrema at Γ. The band gap values for wz-BeO and MgO agree reasonably well with experiment, 7.97 eV[120] and 10.59 eV[120], respectively. The band

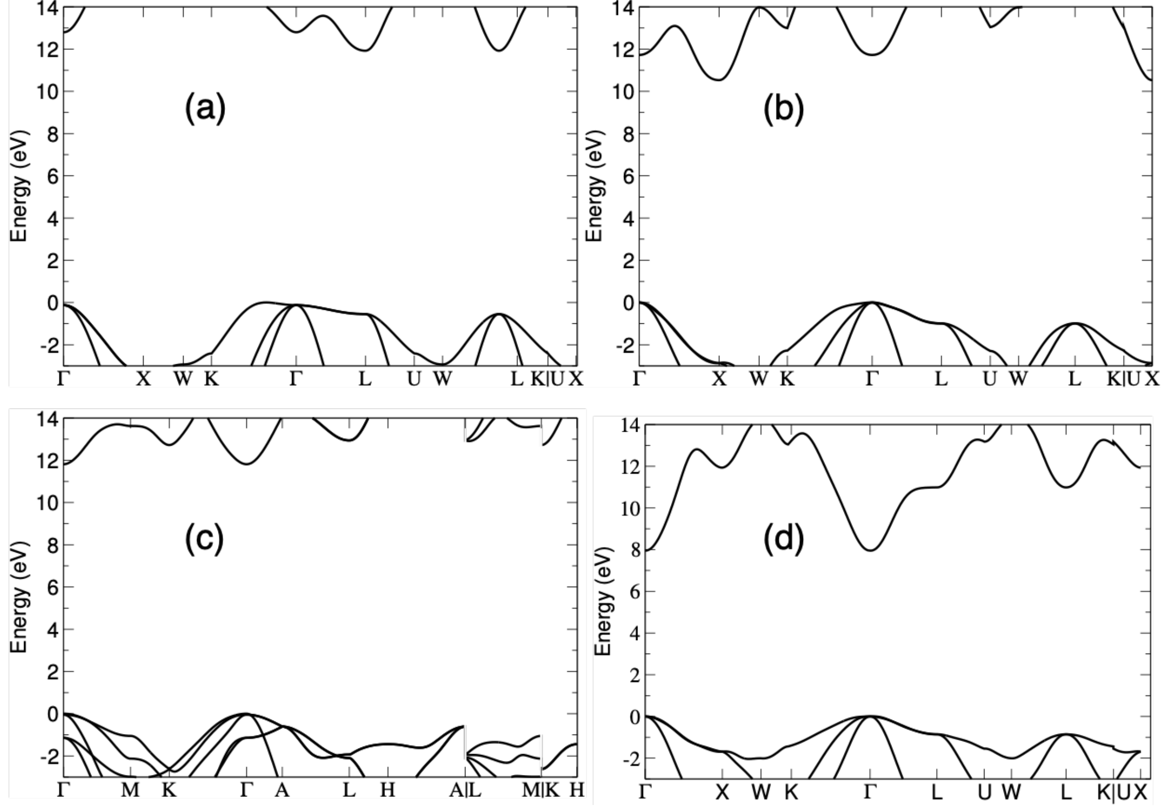

Figure 6.2: Quasiparticle band structures of (a) rs-BeO, (b) zb-BeO, (c) wz-BeO, and (d) MgO. All four have large band gaps and small electron effective masses.

structures of the metastable phases of BeO have been examined in other theoretical work. Self-consistent GW yields a gap of 9.92 eV for zb-BeO[117]. Groh et al. report a band gap of 10.96 eV for rs-BeO but find that the gap is direct at Γ.[121]

6.5 Carrier mobility

The calculated phonon-limited carrier mobility as a function of temperature is shown in Figure 6.3. This value constitutes a theoretical upper limit to the mobility as it does not account for impurity scattering. All four materials have room temperature electron mobilities greater than 100 cm^2/Vs, with rs-BeO and zb-BeO having the largest values. Hole mobility values range from 12 cm^2/Vs (rs-BeO) to 105 cm^2/Vs (wz-BeO, z-axis). These hole mobilities are sizable compared to other p-type wide-band-gap materials (32 cm^2/Vs for β-Ga_2O_3[113] and 35 cm^2/Vs for TiO_2[114]),

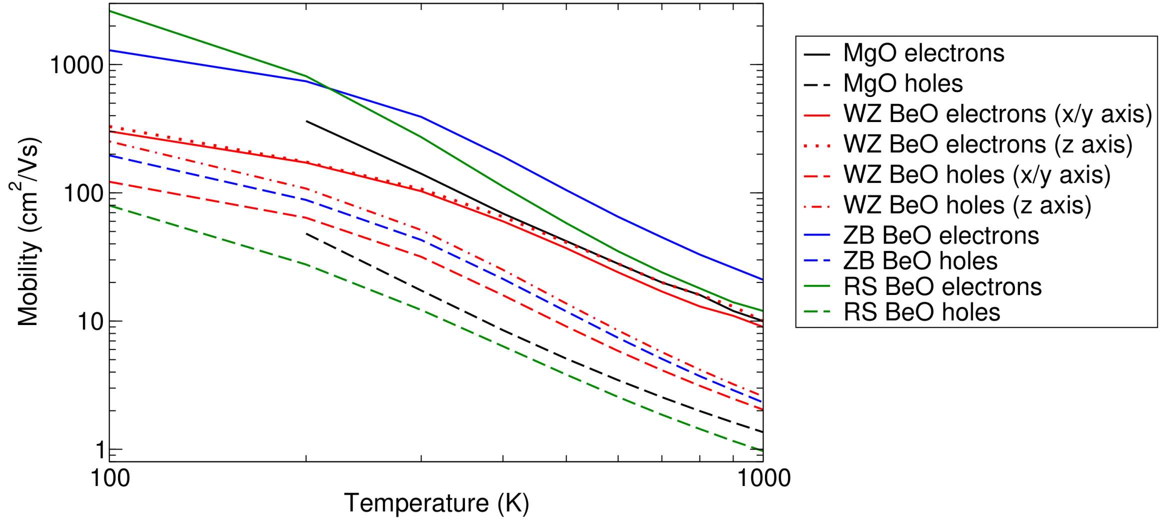

Figure 6.3: Carrier drift mobilities of MgO, rs-BeO, zb-BeO, and wz-BeO.

highlighting the superior performance of wz-BeO and zb-BeO.

6.6 Conclusions

In conclusion, we applied first-principles computational methods to investigate the phonon-limited carrier mobility of MgO and three BeO polytypes as a function of temperature. We find that these materials have large electron mobilities (>100 cm^2/Vs) at room temperature. Hole mobilities are lower but not insignificant. Our work shows the promise of UWBG materials for high-performance high-power electronics applications.

CHAPTER VII

Phonon- and Defect-limited Electron and Hole Mobility of Diamond and Cubic Boron Nitride: A Critical Comparison

7.1 Background and motivation

Diamond and cBN are both ultra-wide-band-gap (UWBG) semiconductors with promising applications in high-power high-frequency electronic devices. They have the highest known thermal conductivities of any materials, allowing for efficient heat dissipation.[122,123] Additionally, despite their ultra-wide band gaps, 5.4 eV in diamond[124] and 6.4 eV in cBN,[125] both show n-type and p-type dopability.[115] These wide band-gap values lead to high breakdown fields (>10 MV/cm in diamond,[126] 2-6 MV/cm in cBN[127]), enabling device operation at high voltages. Furthermore, improvements in sample synthesis area are creating a path to commercialization.

However, despite extensive studies on carrier transport in these materials, there are discrepancies in the reported carrier mobilities of cBN. Reports of the room-temperature electron ($\sim$ 2300 cm^2/Vs[1]) and hole ($\sim$ 2100 cm^2/Vs[2]) mobility in natural diamond lead to very large Baliga figures of merit (over 550,000 10^6 V^2 Ω^{-1} cm^{-2}),[115] confirming its appeal for efficient high-power electronics. Experiments report a large range of carrier mobility values in diamond. Hole mobilities of 138-2016

cm^2/Vs[12] and 3800 cm^2/Vs[128] have been measured in CVD-grown diamond films, while electron mobilities of 70 cm^2/Vs in polycrystalline thin films,[129] 1800 cm^2/Vs in single-crystal type IIa,[130] and 4500 cm^2/Vs for an undoped homoepitaxial CVD diamond film[128] have been measured. However, these discrepancies have largely been characterized. Grain boundaries in polycrystalline samples significantly lower the mobility as compared to single crystals,[131] and the highest reported values have not been reproduced in comparable measurements,[132] highlighting that using photo-excitation to generate free carriers is not well understood in the context of mobility.[133,134] Theoretical work studying diamond hole mobility at thermodynamic equilibrium finds a maximum value of 2000 cm^2/Vs,[135] similar to original experimental reports by Reggiani et al.[2] Recent experimental reports on phosphorus-doped diamond films which do not use photo-excitation report electron mobilities of 660 cm^2/Vs[136] and 1000 cm^2/Vs,[133] but both were carried out with low doping concentrations ($\sim 10^{16}$ cm^{-3}). The measured room-temperature electron mobility of cBN (825 cm^2/Vs)[3] is modest. However, the value of the room-temperature hole mobility of cBN is less clear, with experimental reports spanning a range of two orders of magnitude (2 cm^2/Vs[4] to 500 cm^2/Vs[5]). Until recently, the growth of high-quality samples of cBN has proven difficult. Challenges in cBN film deposition and identification of fine grains often lead to samples that are stressed or mixed phase, containing the hexagonal BN phase and elemental boron.[137] The wide range of sample qualities and preparations have led to an inconsistent recorded value, so there is a need for fundamental understanding of the mechanisms that govern carrier transport to elucidate on this disparity.

7.2 Project objectives and overview

In this work, we investigate the phonon-limited electron and mobility of cBN and diamond with atomistic first-principles calculations in order to understand the fundamental upper bounds to carrier transport in these ultra-wide-band-gap semi-

	cBN		Diamond	
	Electron Mobility (cm^2/Vs)	**Hole Mobility (cm^2/Vs)**	**Electron Mobility (cm^2/Vs)**	**Hole Mobility (cm^2/Vs)**
Theory, phonon-limited (this work)	1610	80.4	1790	1970
Natural diamond	-	-	~2300 [1]	~2700 [2]
CVD-grown diamond films	-	-	4500	138-2016 [12] 3800 [128]
Polycrystalline diamond thin films	-	-	70 [129]	-
Single-crystal type IIa diamond	-	-	1800 [130]	-
P-doped diamond films	-	-	660 [136] 1000 [133]	-
Single-crystal cBN	825 [3]	2 [4]	-	-
cBN thin film	-	500 [5]	-	-

Table 7.1: A summary of experimental room-temperature carrier mobility values in cBN and diamond.

conductors. Our calculations show that, while the electron mobilities for the two materials are similarly high, the hole mobility of cBN is lower than that of diamond by a factor of ~ 25 at room temperature. We analyze the mode-resolved electron-phonon coupling matrix elements and scattering rates to elucidate the mechanisms that hinder the hole mobility in cBN. Our results suggest that the hole mobility of cBN is much lower than some higher previously reported experimental values measured for thin-film samples on conducting substrates, and significantly impedes its performance in p-type high-power electronic devices.

7.3 Methods

Our first-principles approach is based on density functional theory, many-body perturbation theory, density functional perturbation theory, and the efficient interpolation of the electron-phonon coupling matrix elements with the maximally localized Wannier function method. Structural relaxation calculations were carried out in DFT using the local density approximation (Perdew Zunger parameterization) for the exchange-correlation potential[64,65] within Quantum ESPRESSO[66] using a plane-wave basis and norm-conserving pseudopotentials generated with the fhi98PP code[138] for the valence electrons of B, N, and C. The relaxed lattice constants are in good agreement with experiment (3.615 Å for cBN[139] and 3.567 Å for diamond[140]), being underestimated by only 1.3% for cBN and 0.18% for diamond. DFT and GW calculations were carried out with an $8 \times 8 \times 8$ Monkhorst-Pack mesh for the sampling of the first Brillouin zone (BZ). Quasiparticle band structures were calculated using the one-shot G_0W_0 method[141] within BerkeleyGW,[43] as this method has proven to produce physically-sound and sufficiently accurate band structures. The DFT eigenvalues are converged to within 1 meV/atom using a plane-wave cutoff of 100 Ry for cBN and 130 Ry for diamond. Quasiparticle band-structure calculations were performed using dielectric-matrix screening cutoff energies of 50 Ry for BN and 34 Ry

for diamond. The Hybertsen-Louie generalized plasmon-pole model was employed for the frequency dependence of the dielectric function,[44] and the static remainder approach[73] was used to accelerate the convergence of the summation over unoccupied states. Quasiparticle band structures were Quasiparticle band structures were interpolated using the maximally localized Wannier function method and the Wannier90 code.[116] Initial projections for the minimization used the valence s and p orbitals for boron, nitrogen, and carbon s and p orbitals for diamond. Phonon frequencies were found using density functional perturbation theory (DFPT)[41] on a $8 \times 8 \times 8$ BZ sampling grid. Electron-phonon coupling matrix elements were evaluated using the maximally localized Wannier function method[110] within the Electron-Phonon-Wannier (EPW) code,[49] using a carrier density of 10^{18} cm^{-3}, and interpolated to fine electron and phonon BZ sampling meshes up to $88 \times 88 \times 88$ for cBN and $80 \times 80 \times 80$ for diamond. Polar corrections to the electron-phonon matrix elements were applied for cBN.[111] The phonon-limited carrier mobility was evaluated as a function of temperature with the iterative Boltzmann Transport Equation method[50] for carrier states within a 0.3 eV energy range from the band extrema for cBN and within 0.35 eV for diamond.

7.4 Band structures and effective masses

We first determine the electronic band structures of cBN and diamond. The quasiparticle band structures are shown in Figure **??**. Both materials have indirect band gaps, with the valence band maximum (VBM) at Γ, a conduction band minimum (CBM) at X for cBN, and a CBM along the Γ-X high-symmetry path in diamond. We find a band gap of 6.80 eV for cBN and 5.66 eV for diamond, in reasonable agreement with experiment (6.4 eV for cBN,[125] 5.47 eV for diamond[124]). The differences are primarily due to the renormalization of the band gap by the electron-phonon interaction,[142] which we have not considered in this work. The top cBN valence states

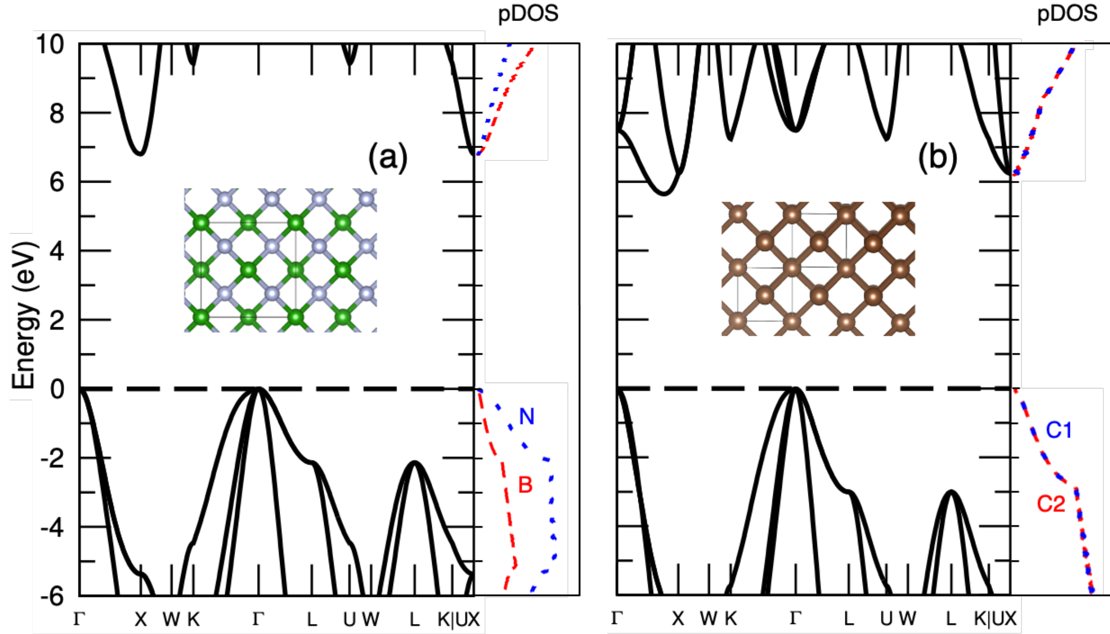

Figure 7.1: The band structure and atom-projected density of states of (a) cBN and (b) diamond, shown with their crystal structures. While the band gaps are similar, the hole effective masses are heavier in cBN. This is because the cBN valence bands consist primarily of second-nearest-neighbor N orbitals, while the diamond valence band is formed by nearest-neighbor C orbitals.

have predominantly nitrogen character while the bottommost conduction states have mostly boron character. Diamond valence and conduction states are equally composed of the sp^3 orbitals of the two carbon atoms. The band structures are qualitatively similar, but this distinction in the valence character is responsible for the different hole effective masses, shown in Table 7.3, which has a strong impact on the resulting carrier-transport properties. A larger effective mass both reduces the mobility directly, being inversely proportional to the mobility, and indirectly, as it yields a larger density of states and thus a shorter carrier scattering time.

7.5 Phonon dispersions

The phonon dispersions of cBN and diamond are presented in Figure 7.2. The calculated sound velocities and optical-mode frequencies at Γ are in good agreement

Effective Mass	cBN		Diamond	
	This work	Previous theory[143]	This work	Experiment
$m^*_{e,l}$	1.15 ($X \rightarrow \Gamma$)	1.20 ($X \rightarrow \Gamma$)	1.55 (CBM $\rightarrow \Gamma/X$)	1.4[1]
$m^*_{e,t}$	0.27 ($X \rightarrow W$)	0.26 ($X \rightarrow W$)	0.27 ($X \rightarrow W$)	0.36[1]
m^*_{hh}	3.00 ($\Gamma \rightarrow K$) 1.20 ($\Gamma \rightarrow L$) 0.54 ($\Gamma \rightarrow X$)	3.16 ($\Gamma \rightarrow K$) 1.20 ($\Gamma \rightarrow L$) 0.55 ($\Gamma \rightarrow X$)	2.52 ($\Gamma \rightarrow K$) 0.71 ($\Gamma \rightarrow L$) 0.45 ($\Gamma \rightarrow X$)	1.08[2]
m^*_{lh}	0.50 ($\Gamma \rightarrow K$) 1.20 ($\Gamma \rightarrow L$) 0.45 ($\Gamma \rightarrow X$)	0.64 ($\Gamma \rightarrow K$) 1.20 ($\Gamma \rightarrow L$) 0.54 ($\Gamma \rightarrow X$)	0.48 ($\Gamma \rightarrow K$) 0.71 ($\Gamma \rightarrow L$) 0.29 ($\Gamma \rightarrow X$)	0.36[2]
m^*_{so}	0.27 ($\Gamma \rightarrow K$) 0.23 ($\Gamma \rightarrow L$) 0.45 ($\Gamma \rightarrow X$)	0.44 ($\Gamma \rightarrow K$) 0.36 ($\Gamma \rightarrow L$) 0.54 ($\Gamma \rightarrow X$)	0.33 ($\Gamma \rightarrow K$) 0.16 ($\Gamma \rightarrow L$) 0.29 ($\Gamma \rightarrow X$)	0.15[2]

Table 7.2: Carrier effective masses of cBN and diamond after GW corrections. Although the electron masses are similar, holes are heavier in cBN.

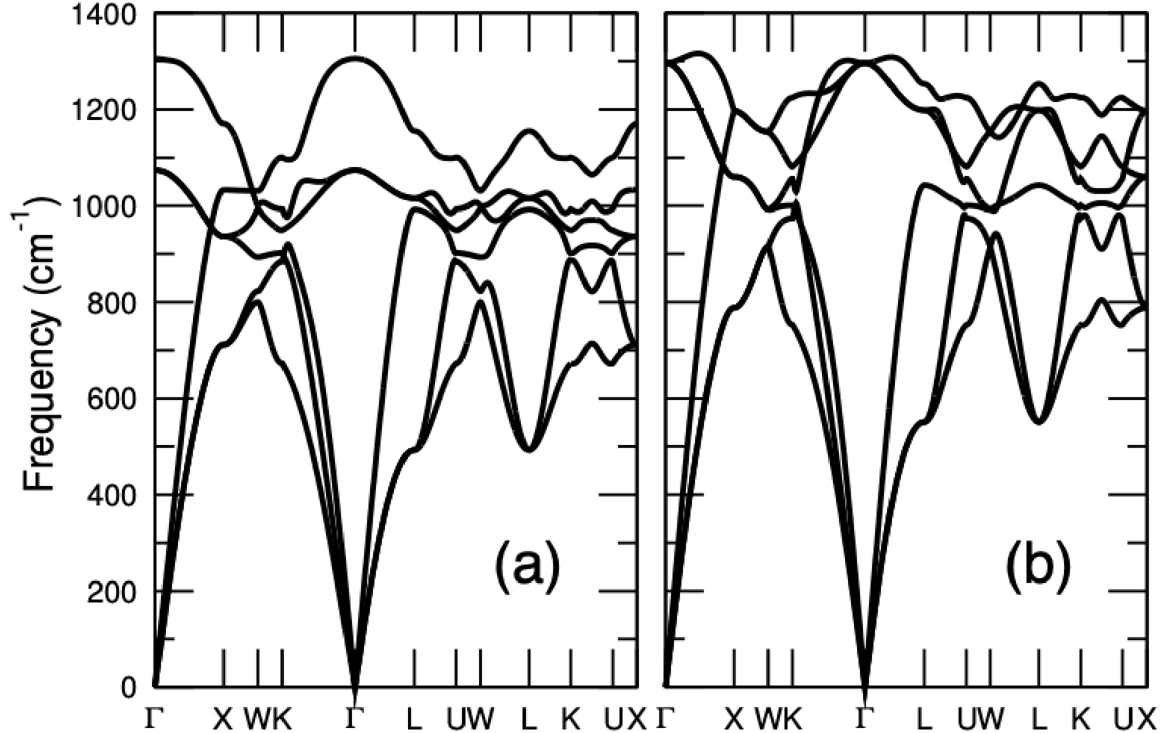

Figure 7.2: Phonon dispersions of (a) cBN and (b) diamond. With the exception of the LO-TO splitting at Γ in polar c-BN, both structures exhibit similar maximum phonon frequencies, sound velocities, and overall band characteristics.

with experiment (Table **??**). Aside from the expected LO-TO splitting present at Γ in cBN due to the polar crystal structure, the dispersions are qualitatively similar, with comparable phonon frequencies throughout the BZ.

7.6 Scattering mechanisms and carrier mobility

We next analyze the electron-phonon coupling matrix elements for the topmost valence and lowest conduction band in both materials. We evaluated the matrix elements for electrons at the CBM and for holes at the VBM and for phonon wave vectors along high-symmetry directions of the first BZ (Figs. 7.3 and 7.4). In each case, this approach includes the states occupied by carriers at room temperature. The polar optical (LO) mode couples most strongly both to electrons and to holes in cBN, while in diamond the electrons couple most strongly to the LA mode and the holes

Property	cBN		Diamond	
	Theory (this work)	Experiment	Theory (this work)	Experiment
$\omega_{TO}(cm^{-1})$	1074	1054[144]	1296	1332[145]
$\omega_{LO}(cm^{-1})$	1305	1305[144]	1296	1332[145]
$V_{L,(111)}$ (m/s)	16000	14600*,[146] 14180*[146]	17100	19039[146]
$V_{T,(111)}$ (m/s)	9420	9570*,[146] 9072*[146]	11100	12300[147]

Table 7.3: Our calculated values for the optical phonon frequencies at Γ and the acoustic sound velocities in cBN and diamond compared to experimental measurements. Asterisks denote polycrystalline samples.

couple most strongly to the TO modes. However, although carriers in cBN are more strongly coupled to the LO mode, the emission rate of these high-frequency phonons is limited due to the high carrier energy required, while the absorption rate is limited by the low optical-phonon Bose-Einstein occupation numbers. Similar arguments apply to the scattering of carriers by the optical modes in diamond. Thus, optical-phonon scattering is suppressed and the acoustic modes are expected to be the dominant carrier-scattering phonon modes in both materials, hence leading to high mobility values.

The suppression of optical-phonon electron scattering is confirmed by our calculated phonon-mode-resolved imaginary self-energies, which show that while electron scattering rates are comparable between cBN and diamond, holes scatter at a rate that is 1-2 orders of magnitude faster in cBN. The phonon-mode-resolved imaginary self-energies (i.e., carrier scattering rates) as a function of the carrier energy are presented in Figure 5. As expected from the discussion in the previous paragraph, the scattering of thermalized carriers (i.e., within a few k_B T from the band extrema) is primarily due to the acoustic modes. On the other hand, the optical phonons only become the dominant carrier-scattering modes for carrier at least 150 meV away from the band extrema, which have enough thermal energy to emit these high-energy

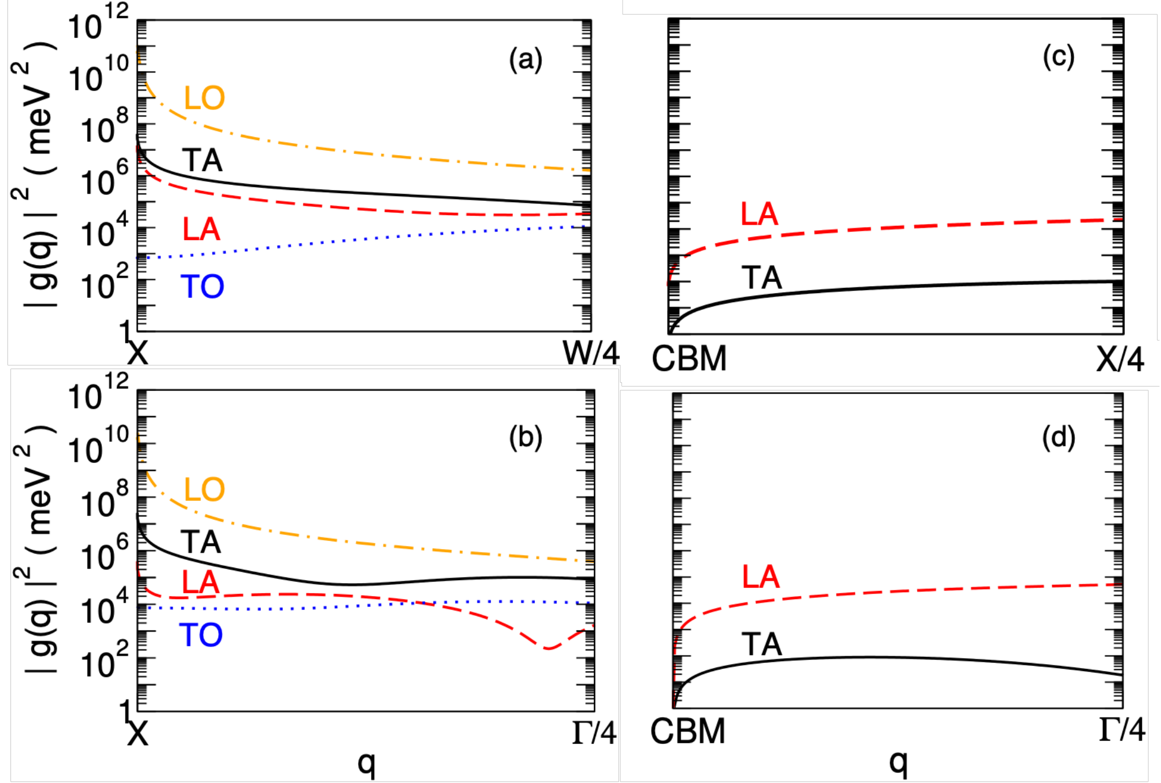

Figure 7.3: Squared electron-phonon coupling intraband matrix elements for the conduction band of (a)-(b) cBN and (c)-(d) diamond as a function of the phonon wave vector along two perpendicular crystallographic directions. The 1/4 fractions denote a quarter of the distance along the reciprocal-space path to the designated high-symmetry point. The modes that couple most strongly to electrons are the polar optical (LO) modes in c-BN and the LA modes in diamond.

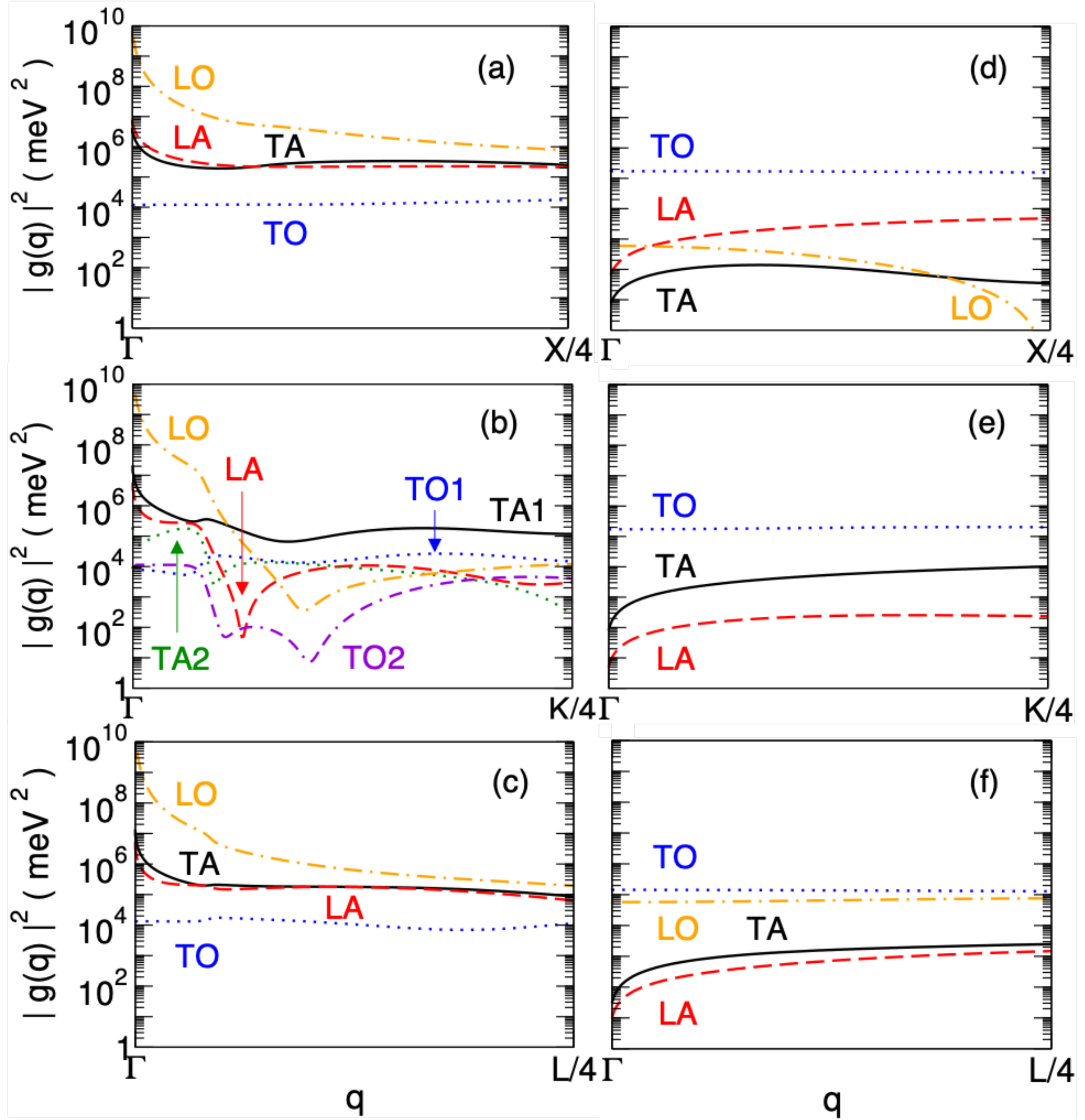

Figure 7.4: Squared electron-phonon coupling matrix elements for the topmost valence band of (a)-(c) cBN and (d)-(f) diamond. The 1/4 fractions denote a quarter of the distance along the reciprocal-space path to the designated high-symmetry point. The modes that couple most strongly to holes for small wave vectors q are the polar optical (LO) modes in c-BN and the TO modes in diamond.

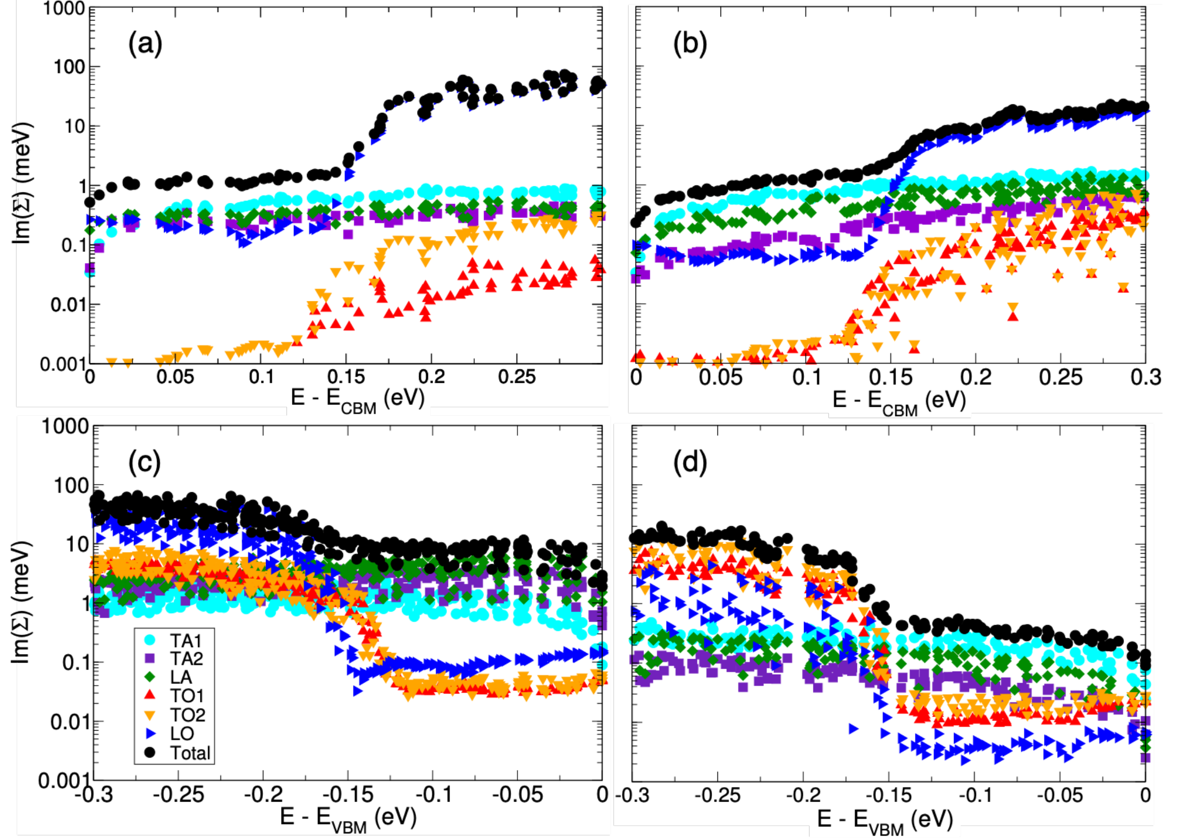

Figure 7.5: Phonon-mode-resolved imaginary self-energies (i.e., carrier scattering rates) as a function of the carrier energy for (a) electrons in cBN, (b) electrons in diamond, (c) holes in cBN, and (d) holes in diamond. The scattering rates of thermal electrons (i.e., within a few k_B T from the band extremum) are comparable for the two materials, but thermal holes scatter at an 1-2 orders-of-magnitude faster rate in cBN compared to diamond.

phonons. The similarity of the imaginary self-energies of thermal electrons for the two materials suggests that the electron mobilities are similar in the two materials. However, the higher scattering rate of thermal holes in cBN by 1-2 orders of magnitude caused by the heavy hole effective mass implies that the hole mobility in cBN should be substantially lower than in diamond.

The calculated phonon-limited carrier mobilities as a function of temperature are shown in Figure 6. Electron and hole mobility values with respect to electron- and phonon-grid densities are converged to within 10 cm^2/Vs and 3 cm^2/Vs, respectively. The electron mobility of cBN at room temperature (1610 cm^2/Vs) is comparable to

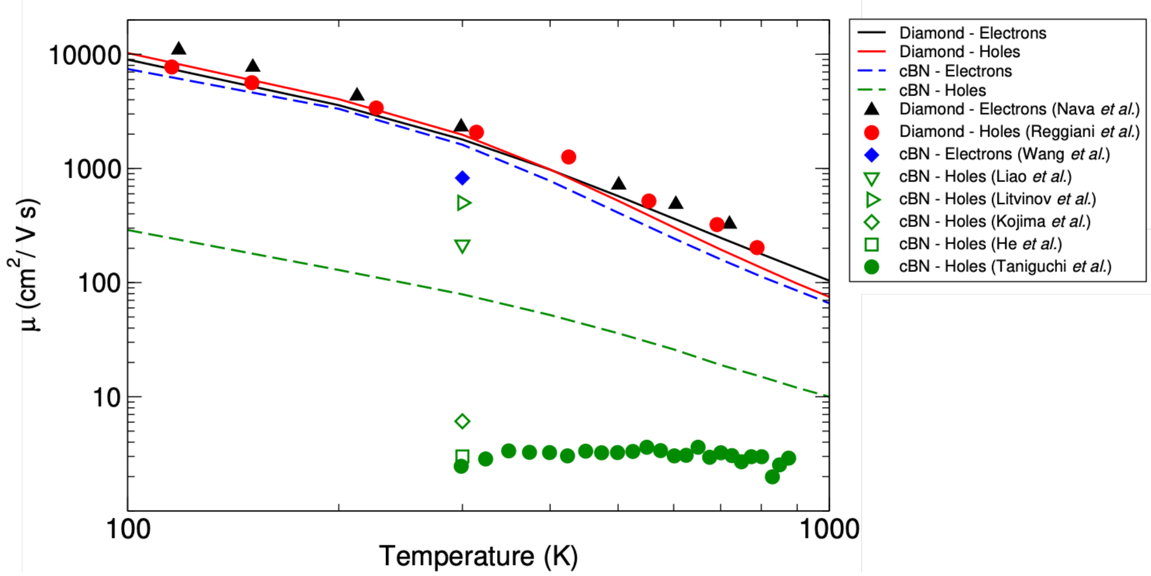

Figure 7.6: Phonon-limited carrier drift mobilities in cBN and diamond as a function of temperature. The experimental diamond drift mobilities are from natural diamond samples (Nava *et al.*,[1] and Reggiani *et al.*[2]) Experimental cBN Hall mobilities are from single crystal (Wang *et al.*[3] and Taniguchi *et al.*[4]) and thin films. (Livinov *et al.*,[5] Liao *et al.*,[6] He *et al.*,[7] and Kojima *et al.*[8]) Open symbols denote thin-film samples. Although the electron mobility is similar in the two materials, the hole mobility in c-BN is much lower than in diamond. The heavier hole effective mass in c-BN and the resulting larger density of states increase the hole-scattering rates and reduce the hole mobility compared to diamond.

that of diamond (1790 cm^2/Vs). However, our calculated hole mobility for cBN (80.4 cm^2/Vs) is significantly lower than for diamond (1970 cm^2/Vs). This difference is attributable to the aforementioned increased hole scattering rate and overall suggests that p-type cBN faces limitations to its performance in high power electronic devices.

Our mobility results are in overall good agreement with previous experimental measurements. The experimental data for the diamond carrier mobilities agree well with our calculated values. Our calculated room-temperature phonon-limited electron mobility of cBN (1610 cm^2/Vs) is higher than experiment (825 cm^2/Vs),[3] possibly due to the presence of imperfections in the experimental sample. However, our calculated value (80.4 cm^2/Vs) for the cBN hole mobility is noticeably lower than the highest reported experimental values (500 cm^2/Vs).[5] We attribute this discrepancy to the

possible conductivity of the silicon substrate used to deposit the characterized cBN thin films in References 5 and 6 and potentially to the non-optimal material quality in the measured samples that may yield samples with mixed phases. It is possible that boron may incorporate into the silicon substrate at high concentrations, making the resulting silicon sample p-type regardless of any original dopant character. This effect could explain why Litvinov et al.[5] measure the same carrier mobility for both n-type and p-type cBN thin films on silicon, especially given that their measured acceptor ionization energy (60 meV) does not match the ionization energy of Be acceptors in cBN (0.23 ± 0.03 eV).[148] Furthermore, the mobility of p-type silicon (480 cm^2/Vs)[149] is similar to the reported hole mobility values in cBN by Liao et al.[6] and by Litvinov et al.,[5] raising the question whether the measured conductivities originate from the substrate rather than the sample. More recent results, which report significantly lower hole-mobility values, were obtained from thin films deposited on quartz[8] or diamond-coated silicon substrates,[7] or single-crystal samples,[4] eliminating the possibility of the substrate contributing to the measured carrier mobility. Overall, our hole-mobility data are consistent with the lower reported values for hole mobility in cBN single crystals or thin films on insulating substrates.

7.7 Impurity scattering

Our final analysis was focused on scattering by neutral impurities and charged impurities. To account for ionized impurity scattering we use the semi-analytical Brooks-Herring model.[50,150–152] We calculate a density-of-states effective mass of 0.48 m_e for electrons in diamond, 1.11 m_e for holes in diamond, 0.69 m_e for electrons in cBN, and 1.19 m_e for holes in cBN, which are used as inputs. We used donor/acceptor energies of 0.37 eV for boron in diamond, 0.84 eV for phosphorus in diamond, 0.24 eV for silicon in cBN, and 0.19 eV for beryllium in cBN. Our results are shown in Figure 7.7. Because of the deep acceptor/donor energies, ionized impurities play little role

in limiting the overall mobility. At low donor/acceptor densities lattice scattering dominates while at higher compensations, neutral impurity scattering is the major limitation to the mobility. Our calculated total mobility agrees well with experimental data for n-type cBN and p-type diamond. The significantly lower experimental values seen in p-type cBN may be due to material quality or the fact that one of the samples is polycrystalline. Our estimated carrier mean-free paths based on the phonon-limited carrier mobilities and effective masses, ranging from 5 nm for holes in cBN to an order of 100 nm for electrons in cBN and electrons and holes in diamond, are shorter than the typical grain sizes in polycrystalline samples ($\sim$1 μm), indicating that grain-boundary scattering is not a limiting factor in reducing the carrier mobility. However, the presence of grain boundaries may introduce additional trapping centers whose concentration increases with decreasing grain size (higher grain surface-to-volume ratio). Such increasing carrier trapping at grain boundaries has been applied to explain the experimentally reported decreasing mobility with decreasing grain size in diamond.[131] Overall we find that defect scattering has a more pronounced effect in the hole mobility of diamond than in cBN, primarily because of the deeper acceptor ionization energies and thus the higher density of non-ionized acceptors that dominate scattering at high doping concentrations.

7.8 Conclusions

In conclusion, we investigated the phonon-limited carrier mobilies of cBN and diamond. The electron mobility of cBN at room temperature is comparable to that of diamond, but the hole mobility for cBN is significantly lower than for diamond. Our results explain the physics of the lower hole mobility values in cBN, corroborating the findings of recent experiments. Overall, this work highlights the challenges that p-type cBN faces in its incorporation into high-power electronic devices.

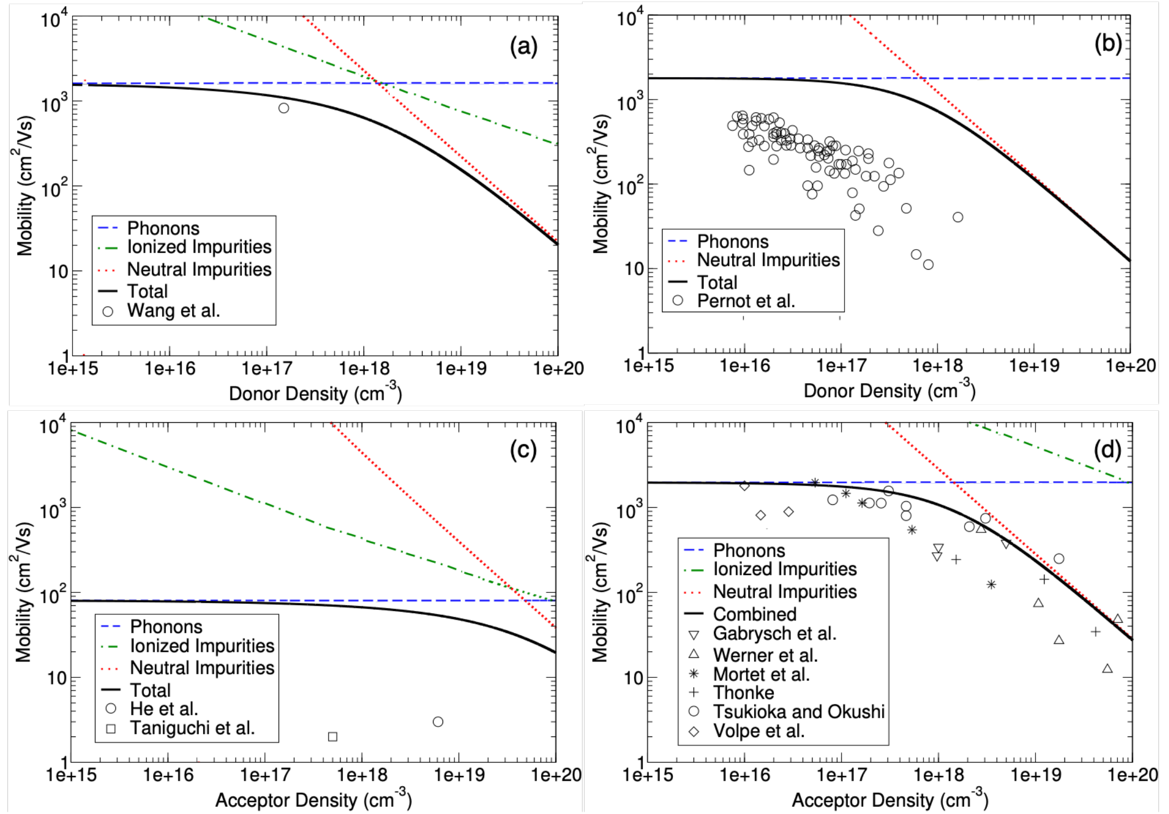

Figure 7.7: Carrier mobility at 300K as a function of donor/acceptor density density in (a) n-type, Si-doped cBN, (b) n-type, P-doped diamond, (c) p-type, Be-doped cBN, and (d) p-type, B-doped diamond. Dashed and dotted lines show the theoretical contributions from lattice scattering, neutral impurities, and ionized impurities. Experimental data points are from experimental work by Wang et al.,[3] He et al.,[7] Taniguchi et al.,[4] Pernot et al.,[9] Gabrysch et al.,[10] Werner et al.,[11] Mortet et al.,[12] Thonke,[13] Tsukioka and Okushi,[14] and Volpe et al.[15]

CHAPTER VIII

Summary and Future Work

8.1 Summary

In conclusion, we applied first-principles methods to investigate the properties of 2D GaN, III-nitride heterostructures, Cu_2O, MgO, three BeO polytypes, cBN, and diamond. We examined the electronic and optical properties of the 2D materials and characterized the carrier transport properties of the others. A detailed summary of findings follows.

Chapter III focused on the functional properties of two-dimensional GaN. We predicted electronic band gaps, luminescence energies, and excitonic properties of monolayer and bilayer 2D GaN as a function of strain. We found that monolayer 2D GaN emits light in the deep-UV range, which is promising for sterilization applications. The long-lived stable triplet excitons of the monolayer may be promising for excitonic applications, and uniaxial in-plane strain results in linearly polarized light emission desirable for display applications. Our results demonstrate that 2D GaN exhibits an array of desirable functional properties and is a synergistic compound between established semiconductors and 2D materials.

In Chapter IV, we discussed the properties of hydrogen-passivated, monolayer BN, AlN, GaN, and InN, as well as their bilayer structures. We treated the polarization as a degree of freedom in tuning the electronic properties and found that the elec-

tronic band gap can be tuned over several eVs. Furthermore, the nature of excitons (interlayer vs. direct) can be controlled by the choice of stacking orientation while preserving the strong exciton binding energy ($\sim$ 1 eV) and short radiative lifetime (few ns). Our results demonstrate that the electronic and optical properties of 2D III-nitride bilayers can be widely controlled over the visible and UV ranges by the choice of stacking orientation, highlighting their promising applications in excitonic and optoelectronic devices.

Chapter V was spent examining on the carrier mobility of copper (I) oxide. We determined that Cu_2O has a large room temperature hole mobility (106 cm^2/Vs) compared to some other p-type oxides, and that its mobility is primarily limited by the polar optical modes. Our work shows the suitability of Cu_2O for high-performance p-type thin-film transistors and other optoelectronic applications.

In Chapter VI, we presented the quasiparticle band structures and carrier mobilities of several UWBG semiconductors, with a comparison of their properties to those of leading materials. Of MgO and the BeO polytypes investigated, zb-BeO and rs-BeO have largest electron mobilities at room temperature, 391 cm^2/Vs and 272 cm^2/Vs, respectively. Hole mobilities of all materials are lower, but comparable. These results highlight the promising carrier mobility properties UWBG materials possess once they have been successfully doped, pushing against the notion that materials with large band gaps ($\sim$ 6 eV) are insulators rather than semiconductors.

Chapter VII details work on the carrier mobility of cubic BN and diamond. The electron mobility of cBN at room temperature is comparable to that of diamond, but hole mobility is significantly lower in cBN. This drop in mobility is due to larger hole scattering rates in cBN and a stronger electron-phonon coupling with acoustic modes. Overall, this work highlights the challenges that p-type cBN faces in its incorporation into high-power electronic devices.

8.2 Future work

The work detailed in this dissertation have expanded on robust research areas, yet many promising avenues of potential investigation remain. Below are several suggestions for topics that would benefit from further study.

1. Investigate nonlinear optics in 2D III-nitrides, specifically second-harmonic generation. Many materials do not exhibit this effect, so many codes are not written to capture this interaction. Writing a robust code to quantify this effect will be critical in advancing this area of work. The strong polarization in these 2D materials should allow for significant nonlinear effects though, opening up possibilities in efficient frequency doubling devices, which have implications in laser devices, LEDs, and more.

2. Study the electronic and optical properties of III-nitride monolayers and heterostructures on a variety of substrates. This work only examined freestanding structures, but substrate selection will be a major consideration for any device design, as it will have an impact on the resulting functional properties. One challenge in this investigation will almost certainly be in employing supercells to adequately capture strain effects in the case of lattice mismatch. While using supercells is routine, inaccurate strains along the 2D material and substrate interface will affect the overall results. However, once these issues are resolved, it will likely be seen that substrate choice presents a significant opportunity to further tune the resulting functional properties.

3. Calculate the dopability and carrier mobility of other UWBG semiconductors. UWBG materials that can hold dopants can have large Baliga figures of merit. Studying the mobility in these materials will further characterize their propensity for high-power electronics and allow for next-generation devices. However, one downfall in this line of inquiry is that many UWBG materials cannot be

sufficiently doped, and the EPW code used in this work does not account for this fact. It is first necessary to perform a thorough defect study to determine the overall feasibility. However, discovering more UWBG materials with high mobility values will allow for devices which can operate at higher powers without sacrificing performance.

4. Add further functionality to the computational methods, specifically the consideration of ionized impurities in the context of carrier mobility. By allowing for imperfect materials systems, the methods become more robust. Rather than representing an upper limit to the mobility, it may be possible to predict values that are even more accurate to experimental findings. As this work shows, is certainly possible to apply semi-empirical models to results after the fact, but combining these methods will allow for results being collected much more efficiently.

APPENDICES

APPENDIX A

Mechanical Stability, Details of Band Gap and Exciton Binding Energy Calculations, GW Corrections to DFT/LDA Band Structures, Wave Functions as a Function of Strain

A.1 Mechanical stability

To confirm the mechanical stability of the freestanding structures, we performed phonon calculations to identify any vibrational modes with imaginary (negative) frequencies. Two methods, density functional perturbation theory(DFPT)[41] in Quantum Espresso and the frozen phonon (FP) method in Phonopy,[69] were used and then compared. The vibrational frequencies were calculated with DFPT on an 8x8x1 grid and interpolated throughout the Brillouin zone (Figure A.1). The acoustic sum rule was applied to the vibrational frequencies at the Gpoint. The frozen phonon calculations were performed withsupercell sizes up to 3x3x1. No imaginary-frequency modes were found for any reciprocal-space points near the zone edges, which would signify a mechanical instability of the structure. We attribute the small negative phonon fre-

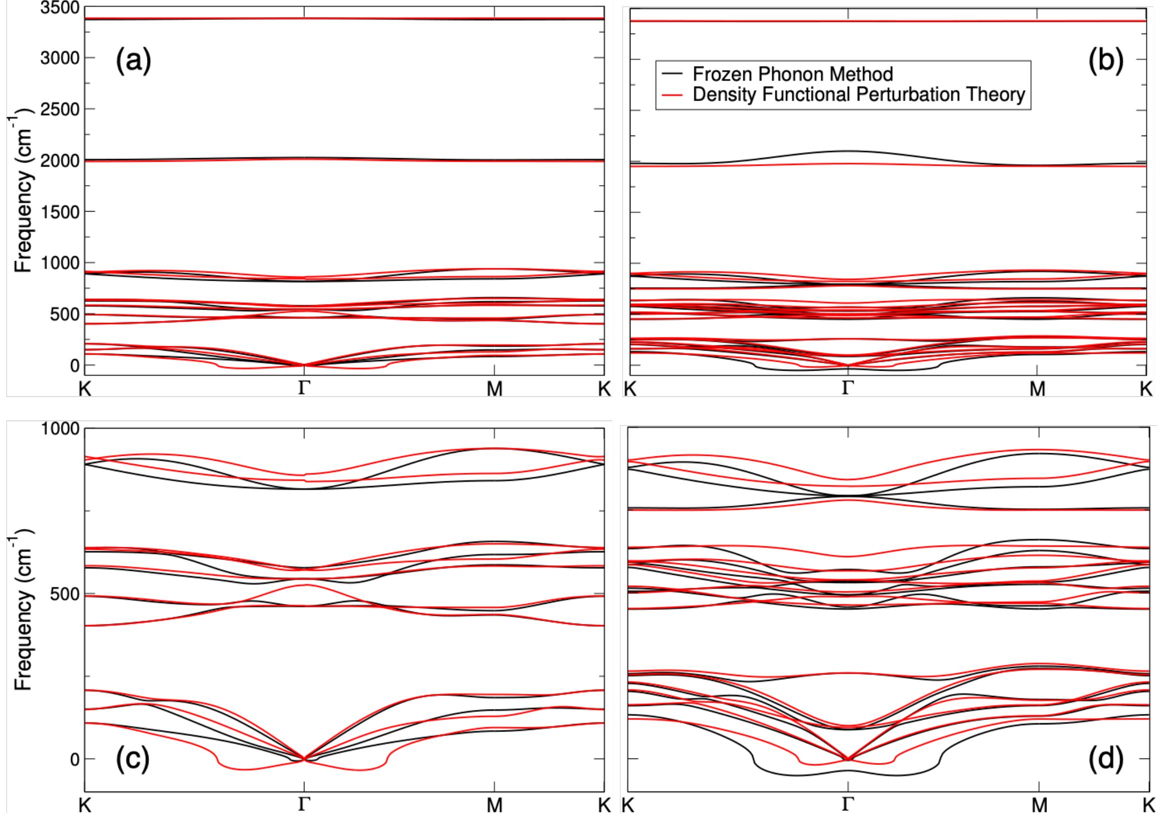

Figure A.1: Phonon dispersion plots of (a) monolayer and (b) bilayer GaN. The low frequency modes for the monolayer (c) and bilayer (d) are also more clearly shown. Positive frequencies confirm the mechanical stability of the structures. Small negative phonon frequencies for the flexural mode near Γ are likely due to finite numerical and convergence accuracy.

quencies that occur for the flexural mode with the parabolic dispersion curve near the Γ point to the finite numerical and convergence accuracy of the calculations. These negative frequencies remained even after a more strict force convergence threshold was used within the DFPT method (10^{-3} a.u. to 10^{-6} a.u). Another possibility is that wrinkling occurs in freestanding 2D GaN, which could give rise to negative flexural-mode frequencies near Γ. However, our calculations with these two different computational methods are not in agreement with each other for the low-frequency flexural mode, pointing to a numerical origin of the discrepancy. Further studies are therefore necessary to investigate the flexural mode near Γ and the physical significance of any negative frequencies.

A.2 Details of band gap and exciton binding energy calculations

GW and BSE calculations were carried out on NKxNKx1 grids in the first Brillouin zone, where NK=8, 10, 12, and 16. To obtain converged band gaps and exciton binding energies, we extrapolated the results to the limit of an infinitely dense grid. The band gap converges as $\frac{1}{NK^2}$, while the exciton binding energy converges as $\frac{1}{NK}$ (Figure A.2).[74] The band-gap values for the 12x12x1 calculation are converged to within 36 meV for monolayer GaN and 14 meV for bilayer GaN compared to the extrapolated values. Exciton binding energies converge more slowly with respect to the Brillouin zone sampling grid. The band-gap values follow a linear trend when plotted as a function of $\frac{1}{NK^2}$, while the exciton binding energy curves follow Equation A.1 for the monolayer and Equation A.2 for the bilayer when plotted as a function of NK [Figure A.2]:

$$E_{b,monolayer}(eV) = \frac{0.402317}{NK - 6.18145} + 1.31007 \tag{A.1}$$

$$E_{b,bilayer}(eV) = \frac{1.40857}{NK - 3.59358} + 0.751893 \tag{A.2}$$

The converged exciton binding energy values are 1.31 eV for monolayer GaN and 0.75 eV for bilayer GaN.

A.3 GW corrections to LDA band structures

To determine the quasiparticle band structures for monolayer and bilayer GaN, we constructed scissors-shift operators using linear fits to the GW corrections on the LDA eigenvalues as a function of the LDA band energies. The data and the fits are shown in Figure A.3. The quasiparticle energies were obtained from GW results on

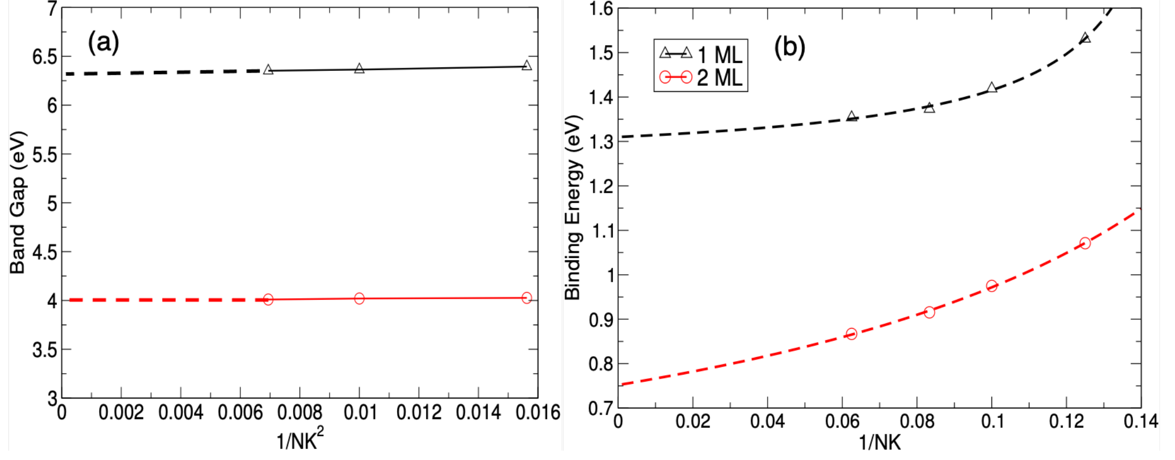

Figure A.2: Band gaps (a) and exciton binding energies (b) of 2D GaN as a function of Brillouin-zone sampling points (NKxNKx1). The data are extrapolated to an infinite number of grid points with trend lines given in Equations A.1 and A.2 fitted to the calculated data.

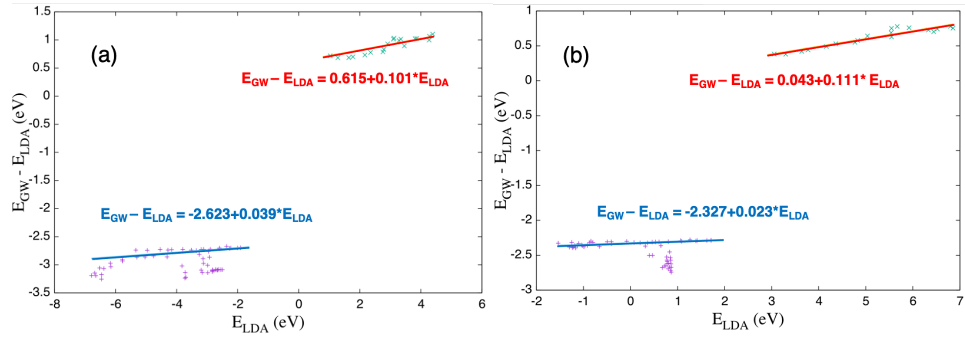

Figure A.3: Quasiparticle corrections to the LDA eigenenergies as a function of the LDA energy for (a) monolayer and (b) bilayer GaN. Solid lines represent the constructed scissors operators.

a 12x12x1 Brillouin zone sampling grid. The quasiparticle corrections to the LDA band structures simultaneously lower the valence bands and shift up the conduction bands. Figure A.4 shows the shift in band energies after scissors shift operators are included into the LDA results.

A.4 Wave functions as a function of strain

Figure A.5 shows the electron and hole wave functions of monolayer and bilayer GaN as a function of in-plane biaxial strain. The polarization fields within each struc-

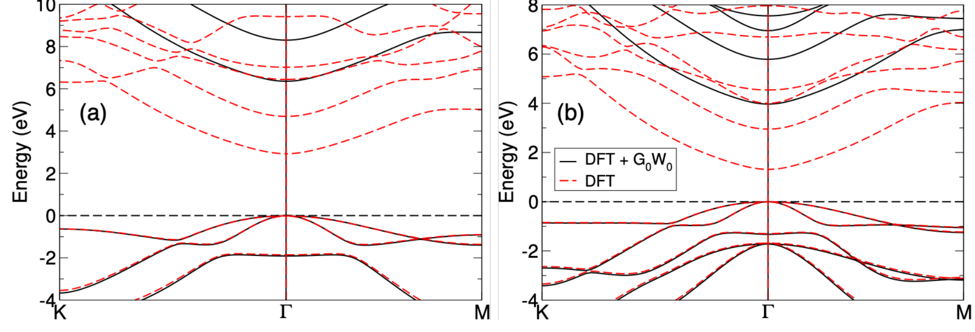

Figure A.4: Band structure of (a) monolayer and (b) bilayer GaN calculated with LDA and LDA+G_0W_0. Energies are referenced to the valence band maximum. GW corrections were added via scissors shift operators. Both materials show a direct band gap at Γ.

ture spatially separate electrons and holes, and compressive strain further accentuates the electron-hole separation.

A.5 Electric field determination from polarization

In addition to calculating the electric field strength via the slope of the electrostatic potential, the magnitude was determined by directly evaluating the dipole moment per unit area of the 2D structures. As the system is effectively non-periodic in the direction perpendicular to the layers, the expectation value of the positive and negative charges with respect to the z axis is well defined. The positive charge contributions to the dipole moment can be easily determined from the locations of the nuclei, while the plane-averaged electron charge density allows the calculation of an expectation value of z. The polarization is then evaluated via Equation A.3:

$$\vec{p_z} = \sum_{IonsI} eZ_I z_I \; - e \int_{cell} zn(z)\, dz \tag{A.3}$$

where e is electron charge, Z is the ionic charge of ion I, and n(z) is the plane-averaged electron charge density. This method yields polarization values of -0.34 e Å for monolayer GaN and -0.13 e Å for bilayer GaN, confirming the direction of the

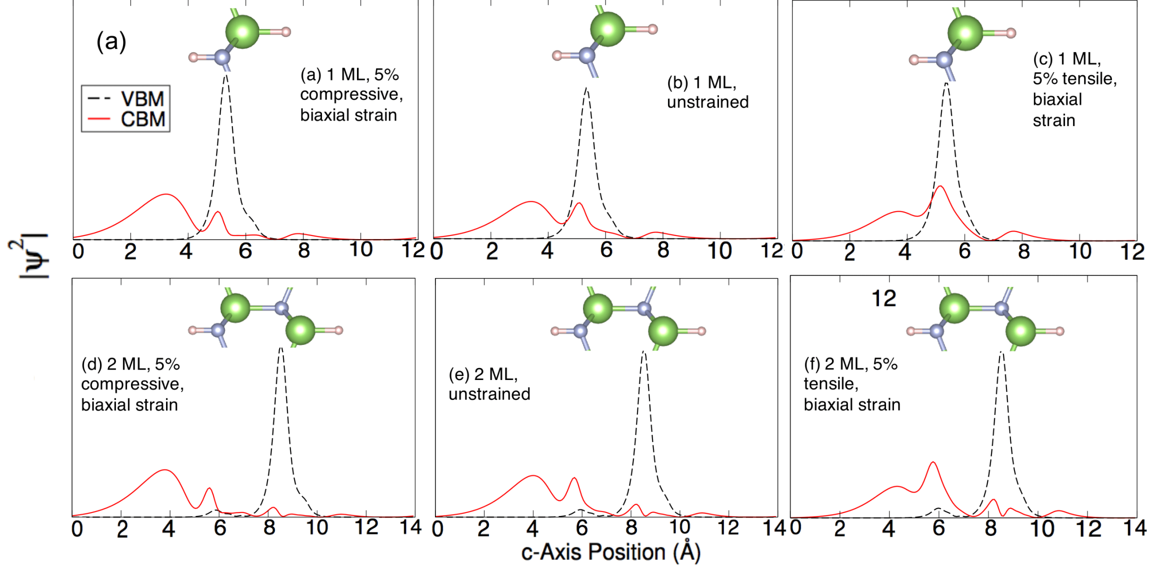

Figure A.5: Electron and hole wave functions squared for (a-c) monolayer and (d-f) bilayer 2D GaN. The application of compressive biaxial strain further increases the electron-hole separation, which amplifies the Stark effect and band-gap reduction.

electric field as found by the slope of the electrostatic potential. The magnitude of the electric field can then be evaluated directly following Equation A.4, assuming a parallel plate capacitor model,

$$E = \frac{\vec{p_z}}{dA\varepsilon_0\varepsilon} \tag{A.4}$$

where d is the distance between the net positive charge and net negative charge, A is the x-y area of the unit cell, ε_0 is vacuum permittivity, and ε is the dielectric screening constant of bulk GaN (9.5).[153] The separation distance is taken to be the z-axis distance between the terminating hydrogen atoms. With this method, the electric field strength was calculated to be 22 MV/cm for monolayer GaN and 5 MV/cm for bilayer GaN. This confirms the presence of a strong electric field, but the numerical inaccuracy with respect to the values found from the electrostatic potential can likely be attributed to several sources. On one hand, the plane distance of the parallel plate capacitor model is not well defined. On the other hand, the dielectric constant of bulk GaN may not accurately describe the screening of electric fields in

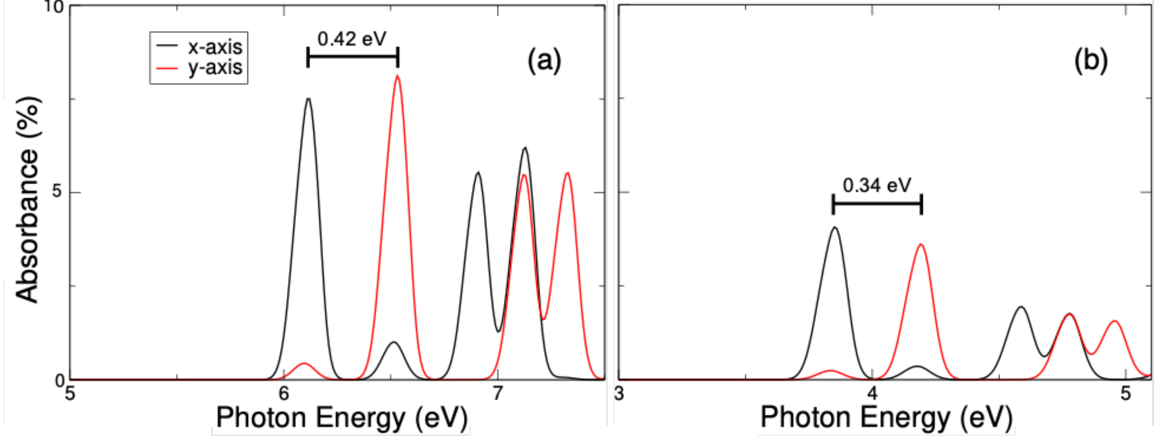

Figure A.6: Optical absorbance spectra for (a) monolayer and (b) bilayer GaN with a 5% uniaxial tensile strain applied along the y-axis. Uniaxial tensile strain along the y-axis breaks the in-plane symmetry of the crystal, resulting in anisotropic light absorption and hence polarized light emission along the x-axis.

2D GaN due to the large electric-field values and the strong confinement.

A.6 Optical absorption spectra

To validate the occurrence of polarized light emission, we calculated the optical absorption spectra of uniaxially strained GaN for the two in-plane light polarizations. The spectra were calculated using BSE using an 8x8x1 Brillouin-zone sampling grid and including the top three valence bands and the lowest conduction band. The resulting spectra are directionally anisotropic, verifying that the emitted light is linearly polarized. Our results verify that, for tensile uniaxial strain along the y-axis,the resulting polarization is along the x-axis.

BIBLIOGRAPHY

BIBLIOGRAPHY

[1] F. Nava, C. Canali, C. Jacoboni, L. Reggiani, and S. Kozlov, “Electron effective masses and lattice scattering in natural diamond,” *Solid State Communications*, vol. 33, no. 4, pp. 475–477, 1980.

[2] L. Reggiani, D. Waechter, and S. Zukotynski, “Hall-coefficient factor and inverse valence-band parameters of holes in natural diamond,” *Phys. Rev. B*, vol. 28, pp. 3550–3555, Sep 1983.

[3] C.-X. Wang, G.-W. Yang, T.-C. Zhang, H.-W. Liu, Y.-H. Han, J.-F. Luo, C.-X. Gao, and G.-T. Zou, “High-quality heterojunction between p-type diamond single-crystal film and n-type cubic boron nitride bulk single crystal,” *Applied Physics Letters*, vol. 83, no. 23, pp. 4854–4856, 2003.

[4] T. Taniguchi, S. Koizumi, K. Watanabe, I. Sakaguchi, T. Sekiguchi, and S. Yamaoka, “High pressure synthesis of uv-light emitting cubic boron nitride single crystals,” *Diamond and Related Materials*, vol. 12, no. 3, pp. 1098–1102, 2003, 13th European Conference on Diamond, Diamond-Like Materials, Carbon Nanotubes, Nitrides and Silicon Carbide.

[5] D. Litvinov, C. A. Taylor, and R. Clarke, “Semiconducting cubic boron nitride,” *Diamond and Related Materials*, vol. 7, no. 2, pp. 360–364, 1998.

[6] K. Liao, W. Wang, and C. Kong, “Study on microstructure and semiconducting properties of doped c-bn-containing films,” *Surface and Coatings Technology*, vol. 141, no. 2, pp. 216–219, 2001.

[7] B. He, W. J. Zhang, Y. S. Zou, Y. M. Chong, Q. Ye, A. L. Ji, Y. Yang, I. Bello, S. T. Lee, and G. H. Chen, “Electrical properties of be-implanted polycrystalline cubic boron nitride films,” *Applied Physics Letters*, vol. 92, no. 10, p. 102108, 2008.

[8] K. Kojima, K. Nose, M. Kambara, and T. Yoshida, “Effects of magnesium doping on growth and electric conductivity of nanocrystalline cubic boron nitride thin films,” *Journal of Physics D: Applied Physics*, vol. 42, no. 5, p. 055304, feb 2009.

[9] J. Pernot and S. Koizumi, “Electron mobility in phosphorous doped 111 homoepitaxial diamond,” *Applied Physics Letters*, vol. 93, no. 5, p. 052105, 2008.

[10] M. Gabrysch, S. Majdi, A. Hallén, M. Linnarsson, A. Schöner, D. Twitchen, and J. Isberg, "Compensation in boron-doped cvd diamond," *physica status solidi (a)*, vol. 205, no. 9, pp. 2190–2194, 2008.

[11] M. Werner, R. Locher, W. Kohly, D. Holmes, S. Klose, and H. Fecht, "The diamond irvin curve," *Diamond and Related Materials*, vol. 6, no. 2, pp. 308–313, 1997.

[12] V. Mortet, M. Daenen, T. Teraji, A. Lazea, V. Vorlicek, J. D'Haen, K. Haenen, and M. D'Olieslaeger, "Characterization of boron doped diamond epilayers grown in a nirim type reactor," *Diamond and Related Materials*, vol. 17, no. 7, pp. 1330–1334, 2008, proceedings of Diamond 2007, the 18th European Conference on Diamond, Diamond-Like Materials, Carbon Nanotubes, Nitrides and Silicon Carbide.

[13] K. Thonke, "The boron acceptor in diamond," *Semiconductor Science and Technology*, vol. 18, no. 3, pp. S20–S26, feb 2003.

[14] K. Tsukioka and H. Okushi, "Hall mobility and scattering mechanism of holes in boron-doped homoepitaxial chemical vapor deposition diamond thin films," *Japanese Journal of Applied Physics*, vol. 45, no. 11, pp. 8571–8577, nov 2006.

[15] P.-N. Volpe, J. Pernot, P. Muret, and F. Omnès, "High hole mobility in boron doped diamond for power device applications," *Applied Physics Letters*, vol. 94, no. 9, p. 092102, 2009.

[16] D. C. Agrawal, H. S. Leff, and V. J. Menon, "Efficiency and efficacy of incandescent lamps," *American Journal of Physics*, vol. 64, no. 5, pp. 649–654, 1996.

[17] S. Pimputkar, J. S. Speck, S. P. DenBaars, and S. Nakamura, "Prospects for LED lighting," *Nature Photonics*, vol. 3, no. 4, pp. 180–182, 2009.

[18] H. Amano, N. Sawaki, I. Akasaki, and Y. Toyoda, "Metalorganic vapor phase epitaxial growth of a high quality gan film using an aln buffer layer," *Applied Physics Letters*, vol. 48, no. 5, pp. 353–355, 1986.

[19] H. Amano, M. Kito, K. Hiramatsu, and I. Akasaki, "P-type conduction in mg-doped GaN treated with low-energy electron beam irradiation (LEEBI)," *Japanese Journal of Applied Physics*, vol. 28, no. Part 2, No. 12, pp. L2112–L2114, dec 1989. [Online]. Available: https://doi.org/10.1143/jjap.28.l2112

[20] S. Nakamura, M. Senoh, and T. Mukai, "Highly p-typed mg-doped GaN films grown with GaN buffer layers," *Japanese Journal of Applied Physics*, vol. 30, no. Part 2, No. 10A, pp. L1708–L1711, oct 1991. [Online]. Available: https://doi.org/10.1143/jjap.30.l1708

[21] M. Kneissl, T. Kolbe, C. Chua, V. Kueller, N. Lobo, J. Stellmach, A. Knauer, H. Rodriguez, S. Einfeldt, Z. Yang, N. M. Johnson, and M. Weyers, "Advances in group III-nitride-based deep UV light-emitting diode technology," *Semiconductor Science and Technology*, vol. 26, no. 1, p. 014036, dec 2010.

[22] K. S. Novoselov, A. K. Geim, S. V. Morozov, D. Jiang, Y. Zhang, S. V. Dubonos, I. V. Grigorieva, and A. A. Firsov, "Electric field effect in atomically thin carbon films," *Science*, vol. 306, no. 5696, pp. 666–669, 2004.

[23] C. Lee, X. Wei, J. W. Kysar, and J. Hone, "Measurement of the elastic properties and intrinsic strength of monolayer graphene," *Science*, vol. 321, no. 5887, pp. 385–388, 2008.

[24] Y. Yoon, K. Ganapathi, and S. Salahuddin, "How good can monolayer mos2 transistors be?" *Nano Letters*, vol. 11, no. 9, pp. 3768–3773, Sep 2011.

[25] W. Ho, J. C. Yu, J. Lin, J. Yu, and P. Li, "Preparation and photocatalytic behavior of mos2 and ws2 nanocluster sensitized tio2," *Langmuir*, vol. 20, no. 14, pp. 5865–5869, Jul 2004.

[26] X. Zong, H. Yan, G. Wu, G. Ma, F. Wen, L. Wang, and C. Li, "Enhancement of photocatalytic h2 evolution on cds by loading mos2 as cocatalyst under visible light irradiation," *Journal of the American Chemical Society*, vol. 130, no. 23, pp. 7176–7177, Jun 2008.

[27] N. Li, Q. Wang, C. Shen, Z. Wei, H. Yu, J. Zhao, X. Lu, G. Wang, C. He, L. Xie, J. Zhu, L. Du, R. Yang, D. Shi, and G. Zhang, "Large-scale flexible and transparent electronics based on monolayer molybdenum disulfide field-effect transistors," *Nature Electronics*, vol. 3, no. 11, pp. 711–717, Nov 2020.

[28] X. Liu and M. C. Hersam, "2d materials for quantum information science," *Nature Reviews Materials*, vol. 4, no. 10, pp. 669–684, Oct 2019.

[29] B. J. Baliga, "Semiconductors for high-voltage, vertical channel field-effect transistors," *Journal of Applied Physics*, vol. 53, no. 3, pp. 1759–1764, 1982.

[30] B. Baliga, "Power semiconductor device figure of merit for high-frequency applications," *IEEE Electron Device Letters*, vol. 10, no. 10, pp. 455–457, 1989.

[31] A. D. Becke, "Perspective: Fifty years of density-functional theory in chemical physics," *The Journal of Chemical Physics*, vol. 140, no. 18, p. 18A301, 2014.

[32] S. Chae, K. A. Mengle, R. Lu, A. Olvera, N. Sanders, J. Lee, P. F. P. Poudeu, J. T. Heron, and E. Kioupakis, "Thermal conductivity of rutile germanium dioxide," *Applied Physics Letters*, vol. 117, no. 10, p. 102106, 2020.

[33] S. Chae, K. Mengle, K. Bushick, J. Lee, N. Sanders, Z. Deng, Z. Mi, P. F. P. Poudeu, H. Paik, J. T. Heron, and E. Kioupakis, "Toward the predictive discovery of ambipolarly dopable ultra-wide-band-gap semiconductors: The case of rutile geo_2," *Applied Physics Letters*, vol. 118, no. 26, p. 260501, 2021.

[34] K. Bushick, K. A. Mengle, S. Chae, and E. Kioupakis, "Electron and hole mobility of rutile geo$_2$ from first principles: An ultrawide-bandgap semiconductor for power electronics," *Applied Physics Letters*, vol. 117, no. 18, p. 182104, 2020.

[35] N. Pant, Z. Deng, and E. Kioupakis, "High electron mobility of al$_x$ga$_{1x}$n evaluated by unfolding the dft band structure," *Applied Physics Letters*, vol. 117, no. 24, p. 242105, 2020.

[36] K. Bushick, S. Chae, Z. Deng, J. T. Heron, and E. Kioupakis, "Boron arsenide heterostructures: lattice-matched heterointerfaces and strain effects on band alignments and mobility," *npj Computational Materials*, vol. 6, no. 1, p. 3, Jan 2020.

[37] N. Sanders, M. Zhang, K. Mengle, L. Qi, and E. Kioupakis, "Effect of stacking orientation on the electronic and optical properties of polar 2d iii-nitride bilayers," *The Journal of Physical Chemistry C*, Jul 2021.

[38] N. Sanders and E. Kioupakis, "Phonon- and defect-limited electron and hole mobility of diamond and cubic boron nitride: a critical comparison," 2021.

[39] P. Hohenberg and W. Kohn, "Inhomogeneous electron gas," *Phys. Rev.*, vol. 136, pp. B864–B871, Nov 1964.

[40] W. Kohn and L. J. Sham, "Self-consistent equations including exchange and correlation effects," *Phys. Rev.*, vol. 140, pp. A1133–A1138, Nov 1965.

[41] S. Baroni, S. de Gironcoli, A. Dal Corso, and P. Giannozzi, "Phonons and related crystal properties from density-functional perturbation theory," *Rev. Mod. Phys.*, vol. 73, pp. 515–562, Jul 2001.

[42] J. M. Rondinelli and E. Kioupakis, "Predicting and designing optical properties of inorganic materials," *Annual Review of Materials Research*, vol. 45, no. 1, pp. 491–518, 2015.

[43] J. Deslippe, G. Samsonidze, D. A. Strubbe, M. Jain, M. L. Cohen, and S. G. Louie, "Berkeleygw: A massively parallel computer package for the calculation of the quasiparticle and optical properties of materials and nanostructures," *Computer Physics Communications*, vol. 183, no. 6, pp. 1269 – 1289, 2012.

[44] M. S. Hybertsen and S. G. Louie, "Electron correlation in semiconductors and insulators: Band gaps and quasiparticle energies," *Phys. Rev. B*, vol. 34, pp. 5390–5413, Oct 1986.

[45] L. Hedin and S. Lundqvist, "Effects of electron-electron and electron-phonon interactions on the one-electron states of solids," ser. Solid State Physics, F. Seitz, D. Turnbull, and H. Ehrenreich, Eds. Academic Press, 1970, vol. 23, pp. 1 – 181.

[46] M. Rohlfing and S. G. Louie, "Electron-hole excitations and optical spectra from first principles," *Phys. Rev. B*, vol. 62, pp. 4927–4944, Aug 2000.

[47] A. S. Toulouse, B. P. Isaacoff, G. Shi, M. Matuchová, E. Kioupakis, and R. Merlin, "Frenkel-like wannier-mott excitons in few-layer Pbi_2," *Phys. Rev. B*, vol. 91, p. 165308, Apr 2015.

[48] N. Marzari, A. A. Mostofi, J. R. Yates, I. Souza, and D. Vanderbilt, "Maximally localized wannier functions: Theory and applications," *Rev. Mod. Phys.*, vol. 84, pp. 1419–1475, Oct 2012.

[49] S. Poncé, E. Margine, C. Verdi, and F. Giustino, "Epw: Electron–phonon coupling, transport and superconducting properties using maximally localized wannier functions," *Computer Physics Communications*, vol. 209, pp. 116–133, 2016.

[50] S. Poncé, E. R. Margine, and F. Giustino, "Towards predictive many-body calculations of phonon-limited carrier mobilities in semiconductors," *Phys. Rev. B*, vol. 97, p. 121201, Mar 2018.

[51] E. Kioupakis, P. Rinke, A. Janotti, Q. Yan, and C. Van de Walle, *Energy Conversion: Solid-State Lighting.* John Wiley & Sons, Ltd, 2013, ch. 8, pp. 231–259.

[52] Y. Taniyasu, M. Kasu, and T. Makimoto, "An aluminium nitride light-emitting diode with a wavelength of 210 nanometres," *Nature*, vol. 441, no. 7091, pp. 325–328, May 2006.

[53] J. Verma, P. K. Kandaswamy, V. Protasenko, A. Verma, H. Grace Xing, and D. Jena, "Tunnel-injection GaN quantum dot ultraviolet light-emitting diodes," *Applied Physics Letters*, vol. 102, no. 4, p. 041103, 2013.

[54] J. Jagger, *Introduction to research in ultraviolet photobiology.* Englewood Cliffs, N.J.: Prentice-Hall, 1967.

[55] D. Bayerl, S. Islam, C. M. Jones, V. Protasenko, D. Jena, and E. Kioupakis, "Deep ultraviolet emission from ultra-thin GaN/AlN heterostructures," *Applied Physics Letters*, vol. 109, no. 24, p. 241102, 2016.

[56] T. Langer, A. Chernikov, D. Kalincev, M. Gerhard, H. Bremers, U. Rossow, M. Koch, and A. Hangleiter, "Room temperature excitonic recombination in GaInN/GaN quantum wells," *Applied Physics Letters*, vol. 103, no. 20, p. 202106, 2013.

[57] E. Kioupakis, Q. Yan, and C. G. Van de Walle, "Interplay of polarization fields and Auger recombination in the efficiency droop of nitride light-emitting diodes," *Applied Physics Letters*, vol. 101, no. 23, p. 231107, 2012.

[58] J. S. Speck and S. F. Chichibu, "Nonpolar and semipolar Group III nitride-based materials," *MRS Bulletin*, vol. 34, no. 5, p. 304–312, 2009.

[59] R. Dingle, D. D. Sell, S. E. Stokowski, and M. Ilegems, "Absorption, reflectance, and luminescence of GaN epitaxial layers," *Phys. Rev. B*, vol. 4, pp. 1211–1218, Aug 1971.

[60] Z. Y. Al Balushi, K. Wang, R. K. Ghosh, R. A. Vilá, S. M. Eichfeld, J. D. Caldwell, X. Qin, Y.-C. Lin, P. A. DeSario, G. Stone, S. Subramanian, D. F. Paul, R. M. Wallace, S. Datta, J. M. Redwing, and J. A. Robinson, "Two-dimensional gallium nitride realized via graphene encapsulation," *Nature Materials*, vol. 15, no. 11, pp. 1166–1171, Nov 2016.

[61] M. C. Lucking, W. Xie, D.-H. Choe, D. West, T.-M. Lu, and S. B. Zhang, "Traditional semiconductors in the two-dimensional limit," *Phys. Rev. Lett.*, vol. 120, p. 086101, Feb 2018.

[62] H. Zhang, F.-S. Meng, and Y.-B. Wu, "Two single-layer porous gallium nitride nanosheets: A first-principles study," *Solid State Communications*, vol. 250, pp. 18 – 22, 2017.

[63] M. S. Prete, A. Mosca Conte, P. Gori, F. Bechstedt, and O. Pulci, "Tunable electronic properties of two-dimensional nitrides for light harvesting heterostructures," *Applied Physics Letters*, vol. 110, no. 1, p. 012103, 2017.

[64] D. M. Ceperley and B. J. Alder, "Ground state of the electron gas by a stochastic method," *Phys. Rev. Lett.*, vol. 45, pp. 566–569, Aug 1980.

[65] J. P. Perdew and A. Zunger, "Self-interaction correction to density-functional approximations for many-electron systems," *Phys. Rev. B*, vol. 23, pp. 5048–5079, May 1981.

[66] P. Giannozzi, S. Baroni, N. Bonini, M. Calandra, R. Car, C. Cavazzoni, D. Ceresoli, G. L. Chiarotti, M. Cococcioni, I. Dabo, A. D. Corso, S. de Gironcoli, S. Fabris, G. Fratesi, R. Gebauer, U. Gerstmann, C. Gougoussis, A. Kokalj, M. Lazzeri, L. Martin-Samos, N. Marzari, F. Mauri, R. Mazzarello, S. Paolini, A. Pasquarello, L. Paulatto, C. Sbraccia, S. Scandolo, G. Sclauzero, A. P. Seitsonen, A. Smogunov, P. Umari, and R. M. Wentzcovitch, "QUANTUM ESPRESSO: a modular and open-source software project for quantum simulations of materials," *Journal of Physics: Condensed Matter*, vol. 21, no. 39, p. 395502, sep 2009.

[67] H. Schulz and K. Thiemann, "Crystal structure refinement of AlN and GaN," *Solid State Communications*, vol. 23, no. 11, pp. 815 – 819, 1977.

[68] X. Huang, E. Lindgren, and J. R. Chelikowsky, "Surface passivation method for semiconductor nanostructures," *Phys. Rev. B*, vol. 71, p. 165328, Apr 2005.

[69] A. Togo and I. Tanaka, "First principles phonon calculations in materials science," *Scripta Materialia*, vol. 108, pp. 1 – 5, 2015.

[70] L. Bengtsson, "Dipole correction for surface supercell calculations," *Phys. Rev. B*, vol. 59, pp. 12 301–12 304, May 1999.

[71] M. L. Tiago, S. Ismail-Beigi, and S. G. Louie, "Effect of semicore orbitals on the electronic band gaps of si, ge, and gaas within the gw approximation," *Phys. Rev. B*, vol. 69, p. 125212, Mar 2004.

[72] S. Ismail-Beigi, "Truncation of periodic image interactions for confined systems," *Phys. Rev. B*, vol. 73, p. 233103, Jun 2006.

[73] J. Deslippe, G. Samsonidze, M. Jain, M. L. Cohen, and S. G. Louie, "Coulomb-hole summations and energies for *gw* calculations with limited number of empty orbitals: A modified static remainder approach," *Phys. Rev. B*, vol. 87, p. 165124, Apr 2013.

[74] G. Shi and E. Kioupakis, "Anisotropic spin transport and strong visible-light absorbance in few-layer snse and gese," *Nano Letters*, vol. 15, no. 10, pp. 6926–6931, Oct 2015.

[75] A. Dobrinsky, G. Simin, R. Gaska, and M. Shur, "III-nitride materials and devices for power electronics," *ECS Transactions*, vol. 58, no. 4, pp. 129–143, Aug 2013.

[76] J. F. Muth, J. H. Lee, I. K. Shmagin, R. M. Kolbas, H. C. Casey, B. P. Keller, U. K. Mishra, and S. P. DenBaars, "Absorption coefficient, energy gap, exciton binding energy, and recombination lifetime of GaN obtained from transmission measurements," *Applied Physics Letters*, vol. 71, no. 18, pp. 2572–2574, 1997.

[77] M. Palummo, M. Bernardi, and J. C. Grossman, "Exciton radiative lifetimes in two-dimensional transition metal dichalcogenides," *Nano Letters*, vol. 15, no. 5, pp. 2794–2800, May 2015.

[78] Z. Huang, T.-Y. Lü, H.-Q. Wang, S.-W. Yang, and J.-C. Zheng, "Electronic and thermoelectric properties of the group-iii nitrides (BN, AlN and GaN atomic sheets under biaxial strains," *Computational Materials Science*, vol. 130, pp. 232 – 241, 2017.

[79] A. S. Rodin, A. Carvalho, and A. H. Castro Neto, "Strain-induced gap modification in black phosphorus," *Phys. Rev. Lett.*, vol. 112, p. 176801, May 2014.

[80] A. Aiello, Y. Wu, A. Pandey, P. Wang, W. Lee, D. Bayerl, N. Sanders, Z. Deng, J. Gim, K. Sun, R. Hovden, E. Kioupakis, Z. Mi, and P. Bhattacharya, "Deep ultraviolet luminescence due to extreme confinement in monolayer GaN/Al(Ga)N nanowire and planar heterostructures," *Nano Letters*, vol. 19, no. 11, pp. 7852–7858, Nov 2019.

[81] D. Bayerl and E. Kioupakis, "Room-temperature stability of excitons and transverse-electric polarized deep-ultraviolet luminescence in atomically thin GaN quantum wells," *Applied Physics Letters*, vol. 115, no. 13, p. 131101, 2019.

[82] Y. Chen, K. Liu, J. Liu, T. Lv, B. Wei, T. Zhang, M. Zeng, Z. Wang, and L. Fu, "Growth of 2d GaN single crystals on liquid metals," *Journal of the American Chemical Society*, vol. 140, no. 48, pp. 16 392–16 395, Dec 2018.

[83] P. Tsipas, S. Kassavetis, D. Tsoutsou, E. Xenogiannopoulou, E. Golias, S. A. Giamini, C. Grazianetti, D. Chiappe, A. Molle, M. Fanciulli, and A. Dimoulas, "Evidence for graphite-like hexagonal aln nanosheets epitaxially grown on single crystal ag(111)," *Applied Physics Letters*, vol. 103, no. 25, p. 251605, 2013.

[84] Y. F. Ng, Y. G. Cao, M. H. Xie, X. L. Wang, and S. Y. Tong, "Growth mode and strain evolution during inn growth on gan(0001) by molecular-beam epitaxy," *Applied Physics Letters*, vol. 81, no. 21, pp. 3960–3962, 2002.

[85] N. Sanders, D. Bayerl, G. Shi, K. A. Mengle, and E. Kioupakis, "Electronic and optical properties of two-dimensional GaN from first-principles," *Nano Letters*, vol. 17, no. 12, pp. 7345–7349, Dec 2017.

[86] F. Bernardini, V. Fiorentini, and D. Vanderbilt, "Spontaneous polarization and piezoelectric constants of III-V nitrides," *Phys. Rev. B*, vol. 56, pp. R10 024–R10 027, Oct 1997.

[87] M. A. Khan, J. N. Kuznia, J. M. Van Hove, N. Pan, and J. Carter, "Observation of a two-dimensional electron gas in low pressure metalorganic chemical vapor deposited GaN-$Al_xGa_{1-x}N$ heterojunctions," *Applied Physics Letters*, vol. 60, no. 24, pp. 3027–3029, 1992.

[88] P. Cudazzo, I. V. Tokatly, and A. Rubio, "Dielectric screening in two-dimensional insulators: Implications for excitonic and impurity states in graphane," *Phys. Rev. B*, vol. 84, p. 085406, Aug 2011.

[89] B. Meyer, "First-principles study of the polar O-terminated ZnO surface in thermodynamic equilibrium with oxygen and hydrogen," *Phys. Rev. B*, vol. 69, p. 045416, Jan 2004.

[90] J. Nørskov, T. Bligaard, A. Logadottir, J. Kitchin, J. Chen, S. Pandelov, and U. Stimming, "Trends in the exchange current for hydrogen evolution," *Journal of The Electrochemical Society*, vol. 152, no. 2, pp. J23–J26, 2005.

[91] M. Hakala, R. Kronberg, and K. Laasonen, "Hydrogen adsorption on doped MoS_2 nanostructures," *Scientific Reports*, vol. 7, no. 1, p. 15243, Nov 2017.

[92] B. Fultz, "Vibrational thermodynamics of materials," *Progress in Materials Science*, vol. 55, no. 4, pp. 247 – 352, 2010.

[93] F. W. Averill, J. R. Morris, and V. R. Cooper, "Calculated properties of fully hydrogenated single layers of BN, BC_2N, and graphene: Graphane and its BN-containing analogues," *Phys. Rev. B*, vol. 80, p. 195411, Nov 2009.

[94] M. K. L. Man, S. Deckoff-Jones, A. Winchester, G. Shi, G. Gupta, A. D. Mohite, S. Kar, E. Kioupakis, S. Talapatra, and K. M. Dani, "Protecting the properties of monolayer MoS_2 on silicon based substrates with an atomically thin buffer," *Scientific Reports*, vol. 6, no. 1, p. 20890, Feb 2016.

[95] W. X. Zhang, T. Li, S. B. Gong, C. He, and L. Duan, "Tuning the electronic and magnetic properties of graphene-like AlN nanosheets by surface functionalization and thickness," *Phys. Chem. Chem. Phys.*, vol. 17, pp. 10 919–10 924, 2015.

[96] M. S. Prete, D. Grassano, O. Pulci, I. Kupchak, V. Olevano, and F. Bechstedt, "Giant excitonic absorption and emission in two-dimensional group-iii nitrides," *Scientific Reports*, vol. 10, no. 1, p. 10719, Jul 2020.

[97] M. S. Miao, Q. Yan, C. G. Van de Walle, W. K. Lou, L. L. Li, and K. Chang, "Polarization-driven topological insulator transition in a GaN/InN/GaN quantum well," *Phys. Rev. Lett.*, vol. 109, p. 186803, Nov 2012.

[98] E. V. Calman, M. M. Fogler, L. V. Butov, S. Hu, A. Mishchenko, and A. K. Geim, "Indirect excitons in van der waals heterostructures at room temperature," *Nature Communications*, vol. 9, no. 1, p. 1895, May 2018.

[99] A. T. Hanbicki, H.-J. Chuang, M. R. Rosenberger, C. S. Hellberg, S. V. Sivaram, K. M. McCreary, I. I. Mazin, and B. T. Jonker, "Double indirect interlayer exciton in a $MoSe_2/WSe_2$ van der waals heterostructure," *ACS Nano*, vol. 12, no. 5, pp. 4719–4726, May 2018.

[100] G. Grosso, J. Graves, A. T. Hammack, A. A. High, L. V. Butov, M. Hanson, and A. C. Gossard, "Excitonic switches operating at around 100K," *Nature Photonics*, vol. 3, no. 10, pp. 577–580, Oct 2009.

[101] A. A. High, A. T. Hammack, L. V. Butov, M. Hanson, and A. C. Gossard, "Exciton optoelectronic transistor," *Opt. Lett.*, vol. 32, no. 17, pp. 2466–2468, Sep 2007.

[102] D. Unuchek, A. Ciarrocchi, A. Avsar, K. Watanabe, T. Taniguchi, and A. Kis, "Room-temperature electrical control of exciton flux in a van der waals heterostructure," *Nature*, vol. 560, no. 7718, pp. 340–344, Aug 2018.

[103] A. Ciarrocchi, D. Unuchek, A. Avsar, K. Watanabe, T. Taniguchi, and A. Kis, "Polarization switching and electrical control of interlayer excitons in two-dimensional van der waals heterostructures," *Nature Photonics*, vol. 13, no. 2, pp. 131–136, Feb 2019.

[104] B. K. Meyer, A. Polity, D. Reppin, M. Becker, P. Hering, P. J. Klar, T. Sander, C. Reindl, J. Benz, M. Eickhoff, C. Heiliger, M. Heinemann, J. Bläsing, A. Krost, S. Shokovets, C. Müller, and C. Ronning, "Binary copper oxide semiconductors: From materials towards devices," *physica status solidi (b)*, vol. 249, no. 8, pp. 1487–1509, 2012. [Online]. Available: https://onlinelibrary.wiley.com/doi/abs/10.1002/pssb.201248128

[105] M. Hara, T. Kondo, M. Komoda, S. Ikeda, J. N. Kondo, K. Domen, M. Hara, K. Shinohara, and A. Tanaka, "Cu2o as a photocatalyst for overall water splitting under visible light irradiation," *Chem. Commun.*, pp. 357–358, 1998.

[106] K. Tu, Q. Wang, A. Lu, and L. Zhang, "Portable visible-light photocatalysts constructed from cu2o nanoparticles and graphene oxide in cellulose matrix," *The Journal of Physical Chemistry C*, vol. 118, no. 13, pp. 7202–7210, Apr 2014.

[107] K. Matsuzaki, K. Nomura, H. Yanagi, T. Kamiya, M. Hirano, and H. Hosono, "Epitaxial growth of high mobility cu2o thin films and application to p-channel thin film transistor," *Applied Physics Letters*, vol. 93, no. 20, p. 202107, 2008.

[108] H. Al-Jawhari, "Review," *Materials Science in Semiconductor Processing*, vol. 40, no. Complete, pp. 241–252, 2015.

[109] A. Werner and H. D. Hochheimer, "High-pressure x-ray study of cu_2o and ag_2o," *Phys. Rev. B*, vol. 25, pp. 5929–5934, May 1982.

[110] F. Giustino, M. L. Cohen, and S. G. Louie, "Electron-phonon interaction using wannier functions," *Phys. Rev. B*, vol. 76, p. 165108, Oct 2007.

[111] C. Verdi and F. Giustino, "Fröhlich electron-phonon vertex from first principles," *Phys. Rev. Lett.*, vol. 115, p. 176401, Oct 2015.

[112] X. Zou, G. Fang, L. Yuan, M. Li, W. Guan, and X. Zhao, "Top-gate low-threshold voltage p-Cu_2O thin-film transistor grown on SiO_2/Si substrate using a high-κ hfon gate dielectric," *IEEE Electron Device Letters*, vol. 31, no. 8, pp. 827–829, 2010.

[113] S. Rafique, L. Han, A. T. Neal, S. Mou, M. J. Tadjer, R. H. French, and H. Zhao, "Heteroepitaxy of n-type β-ga2o3 thin films on sapphire substrate by low pressure chemical vapor deposition," *Applied Physics Letters*, vol. 109, no. 13, p. 132103, 2016.

[114] Y. Furubayashi, T. Hitosugi, Y. Yamamoto, K. Inaba, G. Kinoda, Y. Hirose, T. Shimada, and T. Hasegawa, "A transparent metal: Nb-doped anatase tio2," *Applied Physics Letters*, vol. 86, no. 25, p. 252101, 2005.

[115] J. Y. Tsao, S. Chowdhury, M. A. Hollis, D. Jena, N. M. Johnson, K. A. Jones, R. J. Kaplar, S. Rajan, C. G. Van de Walle, E. Bellotti, C. L. Chua, R. Collazo, M. E. Coltrin, J. A. Cooper, K. R. Evans, S. Graham, T. A. Grotjohn,

E. R. Heller, M. Higashiwaki, M. S. Islam, P. W. Juodawlkis, M. A. Khan, A. D. Koehler, J. H. Leach, U. K. Mishra, R. J. Nemanich, R. C. N. Pilawa-Podgurski, J. B. Shealy, Z. Sitar, M. J. Tadjer, A. F. Witulski, M. Wraback, and J. A. Simmons, "Ultrawide-bandgap semiconductors: Research opportunities and challenges," *Advanced Electronic Materials*, vol. 4, no. 1, p. 1600501, 2018.

[116] A. A. Mostofi, J. R. Yates, Y.-S. Lee, I. Souza, D. Vanderbilt, and N. Marzari, "wannier90: A tool for obtaining maximally-localised wannier functions," *Computer Physics Communications*, vol. 178, no. 9, pp. 685–699, 2008.

[117] K.-L. Wang and S.-P. Gao, "Phonon dispersions, band structures, and dielectric functions of beo and bes polymorphs," *Journal of Physics and Chemistry of Solids*, vol. 118, pp. 242–247, 2018.

[118] K. Chang and M. L. Cohen, "Theoretical study of beo: structural and electronic properties," *Solid State Communications*, vol. 50, no. 6, pp. 487–491, 1984.

[119] U. D. Wdowik, "Structural stability and thermal properties of BeO from the quasiharmonic approximation," *Journal of Physics: Condensed Matter*, vol. 22, no. 4, p. 045404, jan 2010.

[120] O. Madelung, *II-VI compounds*. Berlin, Heidelberg: Springer Berlin Heidelberg, 2004, pp. 173–244.

[121] D. Groh, R. Pandey, M. B. Sahariah, E. Amzallag, I. Baraille, and M. Rérat, "First-principles study of the optical properties of beo in its ambient and high-pressure phases," *Journal of Physics and Chemistry of Solids*, vol. 70, no. 5, pp. 789–795, 2009.

[122] L. Wei, P. K. Kuo, R. L. Thomas, T. R. Anthony, and W. F. Banholzer, "Thermal conductivity of isotopically modified single crystal diamond," *Phys. Rev. Lett.*, vol. 70, pp. 3764–3767, Jun 1993.

[123] K. Chen, B. Song, N. K. Ravichandran, Q. Zheng, X. Chen, H. Lee, H. Sun, S. Li, G. A. G. Udalamatta Gamage, F. Tian, Z. Ding, Q. Song, A. Rai, H. Wu, P. Koirala, A. J. Schmidt, K. Watanabe, B. Lv, Z. Ren, L. Shi, D. G. Cahill, T. Taniguchi, D. Broido, and G. Chen, "Ultrahigh thermal conductivity in isotope-enriched cubic boron nitride," *Science*, vol. 367, no. 6477, pp. 555–559, 2020.

[124] C. D. Clark, P. J. Dean, P. V. Harris, and W. C. Price, "Intrinsic edge absorption in diamond," *Proceedings of the Royal Society of London. Series A. Mathematical and Physical Sciences*, vol. 277, no. 1370, pp. 312–329, 1964.

[125] R. Chrenko, "Ultraviolet and infrared spectra of cubic boron nitride," *Solid State Communications*, vol. 14, no. 6, pp. 511–515, 1974.

[126] M. Geis, "Diamond transistor performance and fabrication," *Proceedings of the IEEE*, vol. 79, no. 5, pp. 669–676, 1991.

[127] T. Brożek, J. Szmidt, A. Jakubowski, and A. Olszyna, "Electrical behaviour and breakdown in plasma deposited cubic bn layers," *Diamond and Related Materials*, vol. 3, no. 4, pp. 720–724, 1994, proceedings of the 4th European Conference on Diamond, Diamond-like and Related Materials.

[128] J. Isberg, J. Hammersberg, E. Johansson, T. Wikström, D. J. Twitchen, A. J. Whitehead, S. E. Coe, and G. A. Scarsbrook, "High carrier mobility in single-crystal plasma-deposited diamond," *Science*, vol. 297, no. 5587, pp. 1670–1672, 2002.

[129] H. J. Looi, R. B. Jackman, and J. S. Foord, "High carrier mobility in polycrystalline thin film diamond," *Applied Physics Letters*, vol. 72, no. 3, pp. 353–355, 1998.

[130] L. S. Pan, D. R. Kania, P. Pianetta, J. W. Ager, M. I. Landstrass, and S. Han, "Temperature dependent mobility in single-crystal and chemical vapor-deposited diamond," *Journal of Applied Physics*, vol. 73, no. 6, pp. 2888–2894, 1993.

[131] C. E. Nebel, "Electronic properties of CVD diamond," *Semiconductor Science and Technology*, vol. 18, no. 3, pp. S1–S11, feb 2003.

[132] M. Nesladek, A. Bogdan, W. Deferme, N. Tranchant, and P. Bergonzo, "Charge transport in high mobility single crystal diamond," *Diamond and Related Materials*, vol. 17, no. 7, pp. 1235–1240, 2008, proceedings of Diamond 2007, the 18th European Conference on Diamond, Diamond-Like Materials, Carbon Nanotubes, Nitrides and Silicon Carbide.

[133] J. Pernot, C. Tavares, E. Gheeraert, E. Bustarret, M. Katagiri, and S. Koizumi, "Hall electron mobility in diamond," *Applied Physics Letters*, vol. 89, no. 12, p. 122111, 2006.

[134] C. Saguy, E. Baskin, and R. Kalish, "Electrical properties of undoped and ion-implanted type iia diamonds measured by photo-hall," *Diamond and Related Materials*, vol. 14, no. 3, pp. 344–349, 2005, proceedings of Diamond 2004, the 15th European Conference on Diamond, Diamond-Like Materials, Carbon Nanotubes, Nitrides and Silicon Carbide.

[135] J. Pernot, P. N. Volpe, F. Omnès, P. Muret, V. Mortet, K. Haenen, and T. Teraji, "Hall hole mobility in boron-doped homoepitaxial diamond," *Phys. Rev. B*, vol. 81, p. 205203, May 2010.

[136] M. Katagiri, J. Isoya, S. Koizumi, and H. Kanda, "Lightly phosphorus-doped homoepitaxial diamond films grown by chemical vapor deposition," *Applied Physics Letters*, vol. 85, no. 26, pp. 6365–6367, 2004.

[137] C. B. Samantaray and R. N. Singh, "Review of synthesis and properties of cubic boron nitride (c-bn) thin films," *International Materials Reviews*, vol. 50, no. 6, pp. 313–344, 2005.

[138] M. Fuchs and M. Scheffler, "Ab initio pseudopotentials for electronic structure calculations of poly-atomic systems using density-functional theory," *Computer Physics Communications*, vol. 119, no. 1, pp. 67–98, 1999.

[139] E. Knittle, R. M. Wentzcovitch, R. Jeanloz, and M. L. Cohen, "Experimental and theoretical equation of state of cubic boron nitride," *Nature*, vol. 337, no. 6205, pp. 349–352, Jan 1989.

[140] S. Shikata, T. Tanno, T. Teraji, H. Kanda, T. Yamada, and J. ichi Kushibiki, "Precise measurements of diamond lattice constant using bond method," *Japanese Journal of Applied Physics*, vol. 57, no. 11, p. 111301, oct 2018.

[141] M. S. Hybertsen and S. G. Louie, "First-principles theory of quasiparticles: Calculation of band gaps in semiconductors and insulators," *Phys. Rev. Lett.*, vol. 55, pp. 1418–1421, Sep 1985.

[142] F. Giustino, S. G. Louie, and M. L. Cohen, "Electron-phonon renormalization of the direct band gap of diamond," *Phys. Rev. Lett.*, vol. 105, p. 265501, Dec 2010.

[143] Y.-N. Xu and W. Y. Ching, "Calculation of ground-state and optical properties of boron nitrides in the hexagonal, cubic, and wurtzite structures," *Phys. Rev. B*, vol. 44, pp. 7787–7798, Oct 1991.

[144] J. A. Sanjurjo, E. López-Cruz, P. Vogl, and M. Cardona, "Dependence on volume of the phonon frequencies and the ir effective charges of several iii-v semiconductors," *Phys. Rev. B*, vol. 28, pp. 4579–4584, Oct 1983.

[145] R. S. Krishnan, "The raman spectrum of diamond," *Proceedings of the Indian Academy of Sciences - Section A*, vol. 19, no. 5, p. 216, May 1944.

[146] S.-F. Wang, Y.-F. Hsu, J.-C. Pu, J. C. Sung, and L. Hwa, "Determination of acoustic wave velocities and elastic properties for diamond and other hard materials," *Materials Chemistry and Physics*, vol. 85, no. 2, pp. 432–437, 2004.

[147] L. Reggiani, S. Bosi, C. Canali, F. Nava, and S. F. Kozlov, "Hole-drift velocity in natural diamond," *Phys. Rev. B*, vol. 23, pp. 3050–3057, Mar 1981.

[148] O. MISHIMA, J. TANAKA, S. YAMAOKA, and O. FUKUNAGA, "High-temperature cubic boron nitride p-n junction diode made at high pressure," *Science*, vol. 238, no. 4824, pp. 181–183, 1987.

[149] G. W. Ludwig and R. L. Watters, "Drift and conductivity mobility in silicon," *Phys. Rev.*, vol. 101, pp. 1699–1701, Mar 1956.

[150] H. Brooks, "Theory of the electrical properties of germanium and silicon," ser. Advances in Electronics and Electron Physics, L. Marton, Ed. Academic Press, 1955, vol. 7, pp. 85–182.

[151] C. Herring, "Transport properties of a many-valley semiconductor," *Bell System Technical Journal*, vol. 34, no. 2, pp. 237–290, 1955.

[152] S. S. Li and W. R. Thurber, "The dopant density and temperature dependence of electron mobility and resistivity in n-type silicon," *Solid-State Electronics*, vol. 20, no. 7, pp. 609–616, 1977.

[153] A. S. Barker and M. Ilegems, "Infrared lattice vibrations and free-electron dispersion in GaN," *Phys. Rev. B*, vol. 7, pp. 743–750, Jan 1973.